Université du Québec
Institut National de la Recherche Scientifique
Centre Énergie, Matériaux, Télécommunications

ELECTROCHEMICAL NITROGEN REDUCTION IN AQUEOUS MEDIA: CHALLENGES AND ULTRASOUND-ENHANCED CATALYTIC STRATEGIES

Par

Arash Toghraei

Thèse présentée pour l'obtention du grade de
Philosophiae Doctor (Ph.D.)
en sciences de l'energie et des matériaux

Jury d'évaluation

Président du jury et Examinateur interne	Ana Tavares Professeur à l'INRS-ÉMT
Examinateur externe	Elena Baranova Professeur à l'Université Concordia
Examinateur externe	Ali Seifitokaldani Professeur à l'Université McGill
Directeur de recherche	Daniel Guay Professeur à l'INRS-ÉMT
Codirecteur de recherche	Gilles Peslherbe Professeur à l'Université Concordia

© Droits réservés de « Arash Toghraei », Mars 2026

ACKNOWLEDGEMENTS

Some time ago, I passed my elementary school teacher on the street. We did not say hi, but I thought about him for the rest of the day. I wondered if he would even recognize me now, I myself had forgotten about him for years, yet he had his own effect on shaping who I am, and how I approach life every day.

Everyone I have interacted with has influenced me in some way, even in small ways that subtly shaped me. As I finish my doctoral thesis, I am deeply grateful to my parents, my wife, my friends, and all the teachers, professors, classmates, and labmates who have had a meaningful impact on how I perceive and understand the world.

I am especially thankful to Prof. Daniel Guay, my PhD supervisor, who taught me not to afraid of research challenges, offered flexibility, and gave me the space to explore the field of ammonia production. In marathon running, there are runners who set the pace for others, "pacemakers" who guide fellow runners. Daniel was a pacemaker for me, and I deeply respect that he has been, and will continue to be, a pacemaker for other runners, despite how demanding it is to keep running for such a long time.

This field, still largely unexplored and full of challenges, requires supportive hands. I was fortunate to have many. I thank my co-supervisor, Prof. Gilles Peslherbe, and his PhD student, Mehdi Shamekhi for their collaboration for doing the theoretical calculations. I also had the opportunity to visit TU Delft for few months, where I explored electrochemical tests in non-aqueous solutions and learned many techniques from Prof. Ruud Kortlever and his PhD student at that time, Boaz Izelaar, with whom I greatly enjoyed discussing our research field and was inspired by his organized approach to research.

My labmates have been invaluable, always ready to help, from the very beginning of my work, both in the laboratory and in settling down in a new country. Thanks a lot, to Mohsen, Sommayeh, Diwakar, Saeed, Birhanu, Cybelle, Minghui, and Saïd, who were there from the start. I also thank Navid, Shahab, and Shreyanka for their help and the enjoyable talks we shared in the laboratory.

During the PhD, there were moments when I felt overwhelmed by challenges. Yet Niki, my wife, lifted me up many times, and I am very, very grateful to have her by my side. I would also like to thank my parents for their lifelong support, for encouraging me to explore the world, and for giving me the freedom to discover myself. I was lucky to share moments of my life and my

education with my twin sister, feeling her support beside me, and with my little brother, who's his love for science since childhood has always inspired me.

I am grateful to FRQNT-B2X (Fonds de recherche du Québec – Nature et technologies) for supporting me financially throughout my PhD. Finally, I thank the jury members, Ana, Ali, and Elena for accepting to read this thesis and for taking part in the defense session.

RÉSUMÉ

L'ammoniac (NH_3) joue un rôle vital dans la vie moderne, étant le principal composant des engrais qui soutiennent des milliards de personnes. Cependant, sa production industrielle dépend fortement de l'H_2 produit à partir de combustibles fossiles, entraînant des émissions importantes de CO_2. La réaction électrochimique de réduction de l'azote (NRR) a émergé comme une approche prometteuse pour la production verte d'NH_3, qui peut également être utilisée comme carburant durable. Dans ce processus, le N_2 est réduit au niveau de la cathode, mais dans les solutions aqueuses, la réduction de l'eau en H_2 concurrence fortement, rendant la formation d'NH_3 difficile.

Dans ce travail, deux approches différentes ont été explorées pour améliorer la production d'NH_3. Tout d'abord, l'alliage a été étudié afin d'améliorer les propriétés de surface de la cathode pour la NRR. L'activité NRR d'un alliage argent-étain (Ag-Sn) a été examinée. Deux éléments ont été alliés, qui sont de faibles catalyseurs pour la réduction de l'eau et qui, à l'état pur, ont été rapportés comme présentant une bonne activité NRR, une combinaison avantageuse pour la NRR. Des expériences de contrôle à long terme dans 2 M KOH et 0,5 M K_2SO_4 ont révélé que l'NH_3 détecté provenait de contaminations plutôt que de la NRR. Des calculs basés sur la théorie de la fonctionnelle de la densité ont montré que, bien que Ag_3Sn présente un potentiel de démarrage de la NRR inférieur à celui de l'Ag et de l'étain purs, il nécessite néanmoins des surtensions élevées pour que la réaction se déroule. Ces résultats soulignent l'importance de réaliser correctement des tests de contrôle à long terme afin d'éviter des rapports faussement positifs sur l'activité NRR.

La deuxième approche a abordé la difficulté observée d'activer électrochimiquement le N_2. Dans cette méthode novatrice, une cellule électrochimique a été placée dans un bain à ultrasons, où la sonication active les molécules de N_2 pour leur réduction ultérieure à la cathode. Sans ultrasons, aucun NH_3 n'a été détecté avec une cathode en cuivre pendant 1 heure, tandis que la NRR sonoélectrochimique a produit 15,6 µg/h d'NH_3 en utilisant un mélange N_2+Ar à 50:50. L'ajout de polytétrafluoroéthylène (PTFE), qui génère des charges de surface triboélectriques sous conditions ultrasonores et favorise la formation de radicaux réactifs, a significativement amélioré l'activation du N_2. Cette amélioration a été confirmée par une augmentation d'environ 25 fois de la concentration en NO_2^-, ce qui a conduit à un taux de production d'NH_3 de 78,9 µg/h. Les expériences de contrôle ont confirmé que l'NH_3 provenait uniquement du N_2. L'étude met également en évidence les rôles critiques des niveaux optimisés d'O_2, de l'incorporation d'Ar et

de la charge en PTFE dans la promotion de l'activation du N_2 et l'augmentation du rendement en NH_3.

Cette thèse souligne les défis liés à la contamination et à la fiabilité des mesures de la NRR, ainsi que la difficulté de produire de l'NH_3 uniquement par des réactions électrochimiques en solution aqueuse. Elle présente ensuite une nouvelle méthode tirant parti de la sonochimie pour l'activation du N_2 et de sa possible intégration avec la réduction électrochimique pour la production verte d'NH_3 en solution aqueuse.

Mots-clés : Réaction de réduction de l'azote ; Alliage Ag-Sn ; Contamination en ammoniac ; Électrocatalyse assistée par ultrasons ; Contact-électro-catalyseur ; Production verte d'ammoniac ; Conversion du N_2 ; Électrification par contact

ABSTRACT

Ammonia (NH_3) plays a vital role in modern life, serving as the main component of fertilizers sustaining billions. However, its industrial production relies heavily on H_2 produced from fossil fuels, causing significant CO_2 emissions. Electrochemical nitrogen reduction reaction (NRR) has emerged as a promising approach for green NH_3 production which can also be used as a sustainable fuel. In this process, N_2 is reduced at the cathode, but in aqueous solutions, water reduction to H_2 competes strongly, making NH_3 formation challenging.

In this work, two different approaches were explored to enhance NH_3 production. First, alloying was studied to improve cathode surface properties for NRR. The NRR activity of a silver-tin alloy (Ag_3Sn) was studied. Two elements were alloyed, which are weak catalysts for water reduction, and in their pure form have been reported to exhibit good NRR activity, a combination that is advantageous for NRR. Long-term control experiments in 2 M KOH and 0.5 M K_2SO_4 revealed that the detected NH_3 originated from contamination rather than NRR. Density functional theory calculations further showed that although Ag_3Sn exhibits a lower NRR onset potential than pure Ag and Sn, it still requires high overpotentials to proceed. These results highlight the importance of properly running long-term control tests to avoid false-positive reports of NRR activity.

The second approach addressed the observed difficulty of activating N_2 electrochemically. In this novel method, an electrochemical cell was placed in an ultrasonic bath, where sonication activated N_2 molecules for subsequent reduction at the cathode. Without ultrasound, no NH_3 was detected using a copper cathode within 1 hour, whereas sonoelectrochemical NRR produced 15.6 μg/h NH_3 using a 50:50 N_2+Ar mixture. Addition of polytetrafluoroethylene (PTFE), which generates triboelectric surface charges under ultrasonic conditions and promotes reactive radical formation, significantly enhanced N_2 activation. This enhancement was supported by a ~26-fold increase in NO_2^- concentration. This resulted in a NH_3 production rate of 78.9 μg/h. Control experiments confirmed that the NH_3 originated solely from N_2. The study also highlights the critical roles of optimized O_2 levels, Ar incorporation, and PTFE loading in promoting N_2 activation and increasing NH_3 yield.

The thesis highlights the challenges of contamination and reliable NRR measurement, along with the difficulty of producing NH_3 solely through electrochemical reactions in aqueous solutions. It then presents a new method that takes advantage of sonochemistry for N_2 activation and the

possibility of its integration with electrochemical reduction for green NH_3 production from N_2 in aqueous solutions.

Keywords: Nitrogen reduction reaction; Ag-Sn alloy; Ammonia contamination; Ultrasound-Assisted Electrocatalysis; Contact-electro-catalyst; Green ammonia production; N_2 conversion; Contact electrification

SOMMAIRE RÉCAPITULATIF

RÉDUCTION ÉLECTROCHIMIQUE DE L'AZOTE EN MILIEU AQUEUX : DÉFIS ET STRATÉGIES CATALYTIQUES AMÉLIORÉES PAR ULTRASONS

1.1 Contexte

L'ammoniac (NH_3) est un élément clé des engrais industriels et l'on estime qu'il soutient les moyens de subsistance d'environ la moitié de la population mondiale. Cependant, la production industrielle de NH_3 par le procédé Haber-Bosch émet chaque année environ 1,4 % du total des émissions mondiales de CO_2. Une méthode durable de production d'ammoniac sans carbone (vert) permettrait non seulement d'éliminer ces émissions de CO_2, mais aussi d'utiliser le NH_3 comme vecteur d'énergie propre, celui-ci étant considéré comme le carburant de l'avenir (Figure 1.1). Une méthode prometteuse est la réaction de réduction électrochimique de l'azote (NRR), qui permet la conversion directe de N_2 en NH_3 dans une cellule électrochimique, où N_2 réagit avec des protons solvatés et des électrons, conduits à la surface de la cathode par une source d'énergie. Cependant, malgré des années de recherche, cette méthode reste à un faible niveau de maturité technologique (TRLs), généralement 1 à 3. Cela est principalement dû à la forte liaison triple du N_2 et à la faible activation de N_2 à la surface de nombreux électrocatalyseurs. Aux potentiels négatifs requis pour la NRR, la réaction concurrente d'évolution de l'hydrogène (HER) domine généralement, et la plupart des protons/électrons se combinent pour produire du H_2 plutôt que du NH_3, entraînant une faible sélectivité pour la NRR.

Au cours des dernières années, plusieurs électrocatalyseurs à base de métaux et de non-métaux ont été rapportés comme actifs pour la NRR. Cependant, les rendements en NH_3 sont restés faibles, produisant généralement du NH_3 dans la gamme de 1 partie par million (ppm). Ces faibles rendements rendent les résultats très sensibles aux erreurs de mesure et à la contamination. Récemment, des protocoles ont été proposés pour minimiser les effets de faux positifs. En suivant ces protocoles, qui mettent l'accent sur des tests de contrôle rigoureux, aucune activité de NRR n'a été observée pour de nombreux matériaux différents (Table 1.1). Dans de nombreux cas, la contamination du gaz de purge et/ou la réduction d'espèces azotées autres que N_2 ont été identifiées comme les principales sources d'erreur.

En gardant à l'esprit ces écueils liés aux faux positifs, notre objectif a été de synthétiser un alliage potentiellement actif et d'étudier son activité vis-à-vis de la NRR en réalisant différents tests de

contrôle. Nous avons sélectionné l'alliage en combinant des métaux présentant une faible adsorption de l'hydrogène, afin de minimiser la HER. Un autre critère essentiel était d'associer un métal à bande d et un métal à orbitales p, afin de bénéficier de l'hybridation des orbitales p–d. Cette stratégie a déjà été appliquée pour développer des électrocatalyseurs actifs pour la réduction de NO_3^- et NO_2^- en NH_3, l'hybridation p–d étant censée améliorer l'activité en modulant la structure électronique et en facilitant les étapes réactionnelles intermédiaires. Plus récemment, cette approche a été utilisée dans la recherche de matériaux plus actifs pour la NRR, où l'alliage du Cu (orbitales d) avec le Ga (orbitales p) a montré une activité renforcée en réduisant la barrière énergétique de la réaction pour l'hydrogénation du N_2.

Dans le premier projet de cette thèse, Ag et Sn ont été choisis sur la base de ces critères et du fait que les métaux purs ont montré une activité raisonnable pour la NRR en solution aqueuse. Ce premier projet combine des tests électrochimiques expérimentaux et une analyse computationnelle par la théorie de la fonctionnelle de la densité (DFT) afin d'étudier l'activité NRR de l'alliage Ag_3Sn supporté sur du tissu de carbone activé (ACC) dans des électrolytes basiques et neutres.

En plus de la stratégie d'alliage, une approche complètement différente consiste à surmonter le goulot d'étranglement de l'activation de N_2 en utilisant une méthode alternative, puis à réduire les espèces azotées activées en NH_3 par réduction électrochimique. Pour ce faire, des chercheurs ont utilisé un traitement plasma sur le gaz N_2 afin de produire des espèces NOx^-. Les NOx^- formés peuvent ensuite être purgés dans une cellule électrochimique, où ils sont réduits à la surface de la cathode pour former du NH_3. Cependant, ce procédé est limité par une consommation énergétique élevée, la complexité de l'infrastructure plasma et les difficultés de contrôle du processus. De plus, l'acheminement efficace des espèces azotées excitées vers les sites catalytiques est entravé par le fait que le plasma est généralement généré dans une chambre séparée.

Le traitement par ultrasons constitue une alternative plus simple pour générer des espèces NOx^- dans des systèmes aqueux. Lors de réactions sonochimiques en solution aqueuse, la cavitation et la production de radicaux réactifs peuvent convertir le gaz N_2 en NOx^-. Comparée à la production de NOx^- assistée par plasma, la méthode ultrasonore nécessite des équipements plus simples et un processus moins complexe. Elle offre également une voie potentiellement plus évolutive pour la génération de NOx^-, en particulier dans les industries utilisant déjà les ultrasons.

Dans ces industries, les NOx^- pourraient être produits comme sous-produit, améliorant ainsi la faisabilité économique globale.

Des études récentes montrent que l'introduction de catalyseurs électro-contact peut améliorer les vitesses de réaction sonochimique. Des matériaux tels que le polytétrafluoroéthylène (PTFE), le fluorure de propylène et d'éthylène (FEP) et le polyfluorure de vinylidène (PVDF) sont triboélectriques et peuvent être polarisés mécaniquement. Sous excitation ultrasonore, ces matériaux favorisent la séparation des charges interfaciales et le transfert d'électrons, renforçant ainsi la génération d'espèces radicalaires réactives. Ces radicaux peuvent ensuite interagir avec d'autres substances présentes en solution, initiant ou accélérant des réactions chimiques. La catalyse électro-contact a récemment été étudiée pour la dégradation de polluants dans l'eau, la production de H_2O_2, la récupération de métaux dans les effluents électroniques, ainsi que la synthèse de composés tels que HCHO et CH_3OH par oxydation du CH_4. Dans une étude, le PTFE a été utilisé comme catalyseur électro-contact dans un bain à ultrasons pour produire de l'ammoniac (NH_3), avec un flux continu de N_2 purgé dans la solution. Dans ce cas, le NH_3 a été généré sans appliquer de potentiel externe ni utiliser de cellule électrochimique. La génération reposait uniquement sur l'effet électro-contact du PTFE, activé par l'agitation ultrasonore. Le mécanisme proposé implique la génération de radicaux OH• et H• via l'électrification de contact. Ensuite, les radicaux OH• se combinent pour former du H_2O_2, tandis que les radicaux H• réagissent avec N_2 pour produire du NH_3. Toutefois, le rendement observé en NH_3 était limité, probablement en raison de l'oxydation concurrente de N_2 en espèces NOx^-. Des recherches antérieures ont montré que des catalyseurs électro-contact tels que le PTFE pouvaient générer de l'acide nitrique et d'autres oxydes d'azote (NOx) dans des conditions similaires. Ces travaux mettent en évidence la coexistence de microenvironnements oxydatifs et réducteurs au cours du processus. Cette double réactivité rend difficile la formation sélective de NH_3 et souligne la nécessité d'un système plus contrôlé pour orienter la réaction vers la production d'ammoniac.

Dans le deuxième projet de cette thèse, nous proposons une stratégie novatrice qui combine l'activation sonochimique et électro-contact de N_2 en vue de sa réduction électrochimique ultérieure en NH_3 sur une feuille de cuivre. Cette stratégie améliore les performances en intégrant la catalyse électro-contact à l'électrocatalyse sous traitement ultrasonore. Cette méthode hybride permet l'activation de N_2 via la catalyse électro-contact, tandis que les espèces NOx^- générées

subissent ensuite une réduction électrochimique en NH_3. Nous avons examiné de manière systématique les paramètres clés influençant la réaction.

1.2 Objectifs et structure de la thèse

La structure de cette thèse s'articule autour de deux approches complémentaires de la production d'ammoniac vert à partir de N_2, conçues pour explorer à la fois le potentiel et les limites des stratégies actuelles, et proposer de nouvelles directions pour une conversion efficace de N_2 en NH_3. La première approche porte sur la stratégie d'alliage, l'une des méthodes les plus étudiées dans ce domaine. La seconde explore un système hybride combinant la réduction électrochimique de l'azote (NRR) avec une activation de N_2 assistée par ultrasons. Ces deux approches sont reliées par un objectif commun : d'une part, démontrer si la stratégie d'alliage étudiée est efficace pour la NRR, et d'autre part, proposer et valider une nouvelle méthodologie hybride pour l'activation de N_2 et la production d'ammoniac.

La thèse est structurée comme suit :

Chapitre 1 propose une introduction générale et une revue de littérature. Il commence par souligner l'urgence de remplacer les combustibles fossiles et l'importance d'une production d'ammoniac sans carbone. La discussion se concentre ensuite sur la NRR aqueuse comme voie prometteuse pour une synthèse durable de NH_3. La revue de littérature est présentée en deux grandes sections, en lien avec les objectifs de la thèse. La première section aborde les défis liés aux faux positifs dans la recherche sur la NRR et examine la stratégie d'alliage, en expliquant le choix de l'alliage Ag–Sn pour cette étude. La seconde section, à partir de la section 1.5, met l'accent sur les stratégies de pré-activation de N_2 afin d'améliorer la production d'ammoniac. Elle inclut une revue sur la réduction des NOx en NH_3, l'activation de N_2 assistée par plasma pour la production d'ammoniac, ainsi que des méthodes moins explorées telles que les ultrasons et la contact-électro-catalyse, qui ont inspiré l'approche hybride développée dans ce travail.

Chapitre 2 décrit les méthodologies expérimentales employées dans les deux directions de recherche, en détaillant les procédés de synthèse, les dispositifs électrochimiques, les techniques de caractérisation et les conditions de réaction.

Chapitre 3 présente le premier article, intitulé « Exploring Ag_3Sn Alloy for Nitrogen Electroreduction to Ammonia », qui étudie les performances de l'Ag_3Sn pour la NRR, avec des analyses détaillées de son activité, de sa sélectivité et de la compréhension mécanistique de son

comportement. L'Ag_3Sn a été choisi en raison de son fort potentiel rapporté pour la NRR. Les objectifs de cette section étaient de synthétiser des alliages Ag–Sn, de mesurer de manière fiable l'activité NRR de l'Ag_3Sn et de comprendre les raisons fondamentales de son activité ou inactivité observée. Cette approche a permis d'évaluer de manière critique si cette stratégie d'alliage, couronnée de succès dans d'autres réactions électrochimiques telles que la NO_3RR et la CO_2RR, est également efficace pour l'électrocatalyse de la NRR.

Chapitre 4 présente le deuxième article, intitulé « Breaking the nitrogen triple bond: a sonoelectrochemical pathway to ammonia synthesis boosted by contact-electro-catalysis ». Il est centré sur le système sonoelectrochimique de NRR couplé au PTFE, et explore comment l'activation assistée par ultrasons et la contact-électro-catalyse influencent les vitesses de réaction et les rendements en ammoniac. Les objectifs ici étaient d'étudier la faisabilité de la NRR sonoelectrochimique, d'examiner si la vitesse de réaction peut être augmentée par l'ajout de contact-électro-catalyseurs comme le PTFE, et de comprendre l'influence de paramètres clés, notamment la composition du gaz de purge et la teneur en PTFE, sur les performances du système.

Enfin, le Chapitre 5 résume les principaux résultats de la thèse, discute de leurs implications et propose des pistes potentielles pour de futures recherches sur l'électrosynthèse de l'ammoniac vert.

1.3 Premier projet : activité électrochimique de Ag_3Sn pour la NRR

1.3.1 Activation du tissu de carbone et synthèse de Ag_3Sn

Le tissu de carbone a été découpé en morceaux de 2 × 1 cm^2 et les deux faces, pour une surface géométrique totale de 4 cm^2, ont été utilisées pour le dépôt de Ag_3Sn. Avant l'activation électrochimique, il a été rincé avec de l'eau déionisée (DI) et dégraissé dans l'acétone par ultrasonication pendant 10 minutes. Pour l'activation du tissu de carbone, une densité de courant constante de 60 mA cm^{-2} a été appliquée pendant 10 minutes dans une cellule à trois électrodes. Dans cette cellule, l'électrolyte était une solution de H_2SO_4 2 M, le tissu de carbone servait d'électrode de travail (anode), Ag/AgCl comme électrode de référence, et la grille de platine servait d'électrode contre (cathode). Après activation, l'échantillon a été rincé plusieurs fois à l'eau et laissé sécher à l'air.

Le tissu de carbone activé a ensuite été utilisé comme substrat pour l'électrodéposition de Ag_3Sn. Pour préparer le bain d'électrodéposition, 0,2 M $SC(NH_2)_2$, 0,025 M $SnSO_4$ et 0,01 M Ag_2SO_4 ont été dissous dans 50 ml de solution de 2 M H_2SO_4. Pour l'électrodéposition, la cellule à trois électrodes mentionnées précédemment a été utilisée, dans laquelle le tissu de carbone activé a été placé comme électrode de travail.

Dans un premier temps, Ag_3Sn a été électrodéposé sur du tissu de carbone non activé à un potentiel constant de -0,65 V vs. Ag/AgCl. Cela a conduit à une faible couverture Ag-Sn. L'alliage a donc été électrodéposé au même potentiel sur le tissu de carbone activé. Bien que la quantité de Ag-Sn déposée ait augmenté, la couverture est restée insuffisante. Nous avons donc employé l'électrodéposition pulsée.

La méthode d'électrodéposition pulsée a été utilisée avec différents rapports d'impulsions marche/arrêt de 2:1, 1:1 et 1:2. Les échantillons déposés avec un rapport de 2:1 ont montré la charge catalytique la plus élevée. Ensuite, des temps marche/arrêt de 2 s / 1 s, 1 s / 0,5 s, 0,5 s / 0,25 s, 0,25 s / 0,125 ms, 0,005 s / 0,0025 s, 0,0025 ms / 0,0012 ms ont été choisis pour l'électrodéposition. Le potentiel pendant la période "marche" de l'impulsion a été fixé à -0,65 V vs. Ag/AgCl. Après une durée totale de dépôt de 3 heures, les échantillons ont été rincés avec de l'eau DI et séchés à l'air. Le catalyseur Ag_3Sn formé sur le tissu de carbone activé (ACC) sera désigné comme Ag_3Sn/ACC dans ce manuscrit.

1.3.2 Caractérisation physicochimique et électrochimique

Pour étudier le dépôt du revêtement sur la surface du tissu de carbone activé, un microscope électronique à balayage (SEM, TESCAN VEGA3) a été utilisé pour obtenir des images microscopiques à différents grossissements, et la composition chimique des différents échantillons a été étudiée par EDS. La structure cristallographique du revêtement synthétisé a été étudiée par diffraction des rayons X (XRD, PANalytical X'Pert Pro).

Une cellule à deux compartiments a été utilisée, dans laquelle une membrane Nafion séparait l'anode (grille de platine) de la cathode (Ag_3Sn/ACC). Une électrode Hg/HgO a été utilisée comme électrode de référence. Les potentiels mesurés ont été rapportés par rapport à l'électrode réversible à hydrogène (RHE) en utilisant la formule suivante :

$E_{RHE} = E_{Hg/HgO} + (0,059\ pH) + 0,098.$

Avant les tests électrochimiques, un morceau de membrane Nafion (2 × 2 cm^2) a été activé selon la procédure suivante : d'abord bouilli pendant une heure dans de l'eau Milli-Q contenant 3 % vol/vol de H_2O_2, puis bouilli à nouveau pendant une heure dans une solution de H_2SO_4 1,2 M. Ensuite, il a été rincé à l'eau et bouilli dans de l'eau Milli-Q fraîche pendant encore une heure.

Deux électrolytes différents ont été utilisés. 30 ml d'une solution neutre (0,5 M K_2SO_4, pH = 7) et d'une solution basique (2 M KOH, pH = 13,5) ont été préparés pour évaluer l'activité NRR en milieu aqueux. Pour introduire du gaz N_2 pur dans la cellule électrochimique, le gaz N_2 a d'abord été purgé à travers 500 ml de solution de H_2SO_4 1 M pour éliminer les traces de NH_3, suivi d'un piège de 10 ml contenant 1 M $KMnO_4$ + 1 M KOH pour éliminer les espèces NO_x. Le dernier piège avant l'introduction du gaz dans la cellule électrochimique était de 10 ml de la même solution que celle utilisée comme électrolyte. De plus, après la cellule électrochimique, 5 ml de solution de H_2SO_4 0,1 M ont été placés pour piéger le NH_3 qui s'échapperait de la cellule. Avant d'appliquer un potentiel, le système a été purgé avec N_2 pendant une heure.

Les tests électrochimiques ont été réalisés en appliquant différents potentiels constants de -0,2, -0,4, -0,6, -0,8 et -1 V vs. RHE pendant 18 heures, tandis qu'un débit de N_2 de 20 ml min^{-1} traversait les pièges et était purgé dans la cellule électrochimique. Après le test, la quantité de NH_3 produite a été mesurée comme décrit ultérieurement.

Différents tests de contrôle ont été effectués pour vérifier la source du NH_3 produit. Le premier consistait à utiliser la même électrode sans appliquer de potentiel, tout en purgeant la cellule électrochimique avec du gaz N_2 ou Ar pendant 18 heures, puis à mesurer la quantité de NH_3 présente dans la cellule. Le deuxième test de contrôle consistait à appliquer un potentiel donné mais en remplaçant le N_2 par de l'Ar (Air Liquide, 99,999 %). Le troisième test de contrôle consistait à utiliser un tissu de carbone activé (ACC) comme électrode au lieu du catalyseur Ag_3Sn/ACC.

Les tests d'électrolyse ont été réalisés sur de longues périodes (18 heures), ce qui conduit à des concentrations plus élevées de NH_3 produit et facilite ainsi sa détection et sa quantification.

1.3.3 Mesure de l'ammoniac

Pour la solution de KOH 2 M, la méthode du bleu d'indophénol a été utilisée. À la suite de l'essai NRR, 10 mL de l'électrolyte ont été prélevés et 0,4 mL d'une solution contenant 1 g de phénol dans 10 mL d'éthanol ont été ajoutés. Ensuite, 1 mL d'une solution contenant 0,1 g d'hydroxyde de sodium, 2 mL d'hypochlorite de sodium et 2 g de citrate de sodium dihydraté dans 10 mL

d'eau ont également été ajoutés à la solution précédente. Puis 0,4 mL d'une solution de 0,5 % en masse de $C_5FeN_6Na_2O$ ont été ajoutés. L'ajout de ces solutions rendait l'électrolyte plus vert pour les échantillons contenant une quantité plus élevée de NH_4^+. La solution a été conservée dans un endroit sombre pendant 2 heures pour permettre la formation de la couleur. Ensuite, l'absorbance de la solution a été enregistrée à 655 nm à l'aide d'un spectrophotomètre UV-Vis (Agilent Cary 60).

Pour le piège H_2SO_4 0,1 M et la solution de K_2SO_4 0,5 M, la méthode du salicylate a été employée. Dans cette méthode, 2 mL de l'électrolyte ont été prélevés de la cellule électrochimique et mélangés à 2 mL d'une solution de NaOH 1 M contenant 5 % en masse d'acide salicylique et 5 % en masse de citrate de sodium. Par la suite, 1 mL de NaClO 0,05 M et 0,2 mL de $C_5FeN_6Na_2O$ à 1 % en masse ont été ajoutés à la solution, qui a ensuite été conservée dans un flacon pendant 2 heures dans l'obscurité. L'absorbance du spectre UV-Vis à 655 nm a ensuite été mesurée.

La courbe d'étalonnage a été obtenue en préparant des solutions de NH_4Cl de 0,5, 1, 2 et 3 ppm (dissoutes dans l'électrolyte correspondant). Leur absorbance a été mesurée à une longueur d'onde de 655 nm. En mesurant l'absorbance de ces échantillons à 655 nm, une relation linéaire entre l'absorbance et la concentration a été établie. Ainsi, la quantité inconnue de NH_3 d'une solution a pu être estimée à l'aide de la courbe d'étalonnage. En utilisant la pente des courbes d'étalonnage, la limite de détection pour chacune des courbes, avec un niveau de confiance de 95 %, a été calculée selon la formule suivante, où SD est l'écart type :

Limite de détection = 3,3 × SD / Pente.

1.3.3 Méthodes théoriques

GPAW 22.8.0, un code Python basé sur la méthode des ondes augmentées par projecteur (PAW), a été utilisé pour les calculs DFT. Les interactions électroniques ont été décrites avec la fonctionnelle d'estimation d'erreur bayésienne incluant la corrélation de van der Waals (BEEF-vdW), afin de calculer avec précision les énergies libres d'adsorption. Les cœurs ioniques ont été décrits avec des pseudopotentiels dérivés de l'approche PAW fournis avec GPAW.

Les structures massives ont été optimisées pour calculer les paramètres de maille avec une coupure en ondes planes de 700 eV et la première zone de Brillouin a été échantillonnée avec des maillages de points k de Monkhorst–Pack 8 × 8 × 8. Les paramètres de maille calculés pour Ag_3Sn sont a = 4,85, b = 6,07 et c = 5,26 Å, en bon accord avec les valeurs expérimentales rapportées : a = 4,78, b = 5,96 et c = 5,18 Å.

La maille élémentaire orthorhombique optimisée (groupe spatial Pmmn) de Ag_3Sn a été utilisée pour construire la surface (001) de la dalle avec quatre couches atomiques. Les images périodiques étaient séparées par 15 Å de vide dans la direction perpendiculaire à la surface. Pour faciliter la convergence SCF, l'occupation des états propres de Kohn–Sham a été lissée par la fonction de Fermi–Dirac avec une largeur de 0,1 eV, et toutes les énergies ont été extrapolées à kBT = 0 eV. Un échantillonnage Monkhorst–Pack 3 × 3 × 1 a été utilisé pour les surfaces, avec une coupure en ondes planes similaire à celle des calculs d'optimisation de la géométrie du massif, et une grille affinée de 9 × 9 × 1 a été utilisée pour les calculs de structure électronique et de densité d'états (DOS).

L'arrangement géométrique des deux couches supérieures ainsi que des adsorbats a été optimisé, les deux couches inférieures étant fixées à leurs positions massives. Toutes les optimisations structurelles ont été considérées comme convergées lorsque la force maximale sur tous les atomes mobiles était inférieure à 0,05 $eV \cdot Å^{-1}$.

L'énergie libre de Gibbs des intermédiaires NRR et des molécules en phase gazeuse a été calculée en ajoutant des corrections aux énergies électroniques calculées par DFT. L'énergie de point zéro (ZPE) a été calculée par analyse des fréquences vibrationnelles dans l'approximation harmonique, et les corrections d'entropie (S) ont été calculées en utilisant le module ASE Thermochemistry avec les approximations de gaz idéal et d'oscillateur harmonique, à T = 298,15 K et P = 1 atm. Les valeurs de ZPE et de S pour les molécules gazeuses N_2, H_2 et NH_3 ont été prises à partir de la base de données en ligne du NIST.

1.3.4 Résultats et discussion

Un alliage Ag_3Sn a été électrodéposé sur la surface d'un tissu de carbone, choisi comme substrat en raison de son inactivité documentée vis-à-vis de la NRR. L'hypothèse était que la porosité du substrat en tissu de carbone permettrait le dépôt de fortes charges de Ag_3Sn, offrant ainsi une grande surface active pour la NRR. La Figure 3.1 montre un morceau du substrat en tissu de carbone et un schéma du dispositif d'électrodéposition.

Le bain d'électrodéposition a été choisi sur la base des travaux de Wang et al.. Nous avons observé que le dépôt commençait à se détacher du substrat après seulement 30 secondes d'électrodéposition à un potentiel constant de -0,65 V vs. Ag/AgCl. Les images obtenues par microscopie électronique à balayage (MEB) dans la Figure 3.2 montrent clairement une couverture

médiocre du substrat en tissu de carbone par le dépôt. Ce phénomène peut être attribué à la nature hydrophobe du tissu de carbone, qui empêche un dépôt métallique uniforme à sa surface.

Pour contourner cette limitation, le tissu de carbone a été activé électrochimiquement dans une solution de H_2SO_4 2 M avant l'électrodéposition, ce qui a accru l'hydrophilie du substrat (comme le montrent la Figure 3.3 et la MEB de la Figure 3.4).

Comme le démontrent les images MEB de la Figure 3.5 et la cartographie élémentaire par spectrométrie de rayons X à dispersion d'énergie (EDS) de la Figure 3.6, la couverture du dépôt Ag-Sn a été augmentée. Cependant, une mauvaise adhésion du revêtement au substrat a encore été observée, avec un détachement de matériau lors du rinçage à l'eau. Afin d'améliorer la couverture et de renforcer l'adhésion, une méthode d'électrodéposition pulsée a été utilisée pour synthétiser Ag_3Sn sur la surface du tissu de carbone activé.

La Figure 3.7 présente les images MEB des échantillons fabriqués avec différentes durées d'impulsion.

Le rapport marche/arrêt des impulsions a été optimisé afin de maximiser la charge en catalyseur. La Figure 3.8 présente les résultats de la MEB et de la cartographie EDS de l'échantillon synthétisé dans des conditions d'impulsion optimisées de 0,005 s en marche et 0,0025 s à l'arrêt. Comme le montrent les Figure 3.8 (a–c), le revêtement Ag-Sn présente une couverture uniforme de la surface du tissu de carbone activé, avec des particules de taille micrométrique réparties de manière homogène sur le substrat. Les cartes de distribution élémentaire représentées dans les Figure 3.8 (d–g) confirment la dispersion homogène de l'argent et de l'étain sur la surface du substrat.

L'analyse EDS a révélé une composition de 18,5 at% Ag, 5,4 at% Sn et 76,1 at% C. La Figure 3.9 présente le diagramme de diffraction des rayons X (DRX) de l'échantillon synthétisé, montrant des pics de diffraction correspondant à Ag_3Sn (ICDD 01-071-0530). Des pics supplémentaires à 25,4° et 43,5° sont attribués au substrat de carbone.

L'activité NRR des échantillons Ag_3Sn/ACC a été évaluée dans une solution de KOH 2 M (pH = 13,5). Pour purifier le gaz de purge, différents pièges chimiques ont été placés le long de son trajet (voir Figure 3.10).

Les courbes d'étalonnage utilisées pour la mesure de NH_3 dans divers électrolytes et dans le piège H_2SO_4 0,1 M sont présentées dans la Figure 3.11. Les limites de détection estimées pour l'électrolyte KOH 2 M et le piège H_2SO_4 0,1 M étaient respectivement de 0,7 et 0,3 ppm.

Les courbes chronoampérométriques représentatives sont présentées dans la Figure 3.12 pour l'échantillon Ag_3Sn/ACC dans le KOH 2 M sous un potentiel de -0,6 V vs. RHE. Les électrolytes ont été purgés soit à l'Ar, soit au N_2. La densité de courant a montré une réponse presque identique, indépendante de la nature du gaz injecté dans l'électrolyte. La concentration de NH_3 s'est révélée inférieure à la limite de détection dans l'électrolyte KOH comme dans le piège H_2SO_4.

L'activité NRR de l'échantillon Ag_3Sn/ACC a également été évaluée dans un électrolyte neutre de K_2SO_4 0,5 M (pH = 7,0). Les courbes chronoampérométriques à un potentiel de -0,6 V vs. RHE sont présentées dans la Figure 3.12, dans l'électrolyte K_2SO_4 0,5 M purgé soit à l'Ar, soit au N_2. Dans cet électrolyte, comme dans le KOH 2 M, la densité de courant a montré une réponse presque identique indépendamment du gaz purgé. Toutefois, les réponses de courant étaient plus faibles dans le K_2SO_4 0,5 M que dans le KOH 2 M. Ce phénomène peut probablement être attribué au taux plus élevé de HER observé dans le KOH 2 M, ce qui est dû à l'alcalinité accrue du milieu et à la concentration plus élevée de cations.

La Figure 3.13 présente la quantité totale de NH_3 mesurée dans l'électrolyte K_2SO_4 0,5 M purgé à l'N_2 et à l'Ar après 18 heures de test sous différents potentiels appliqués. Les concentrations correspondantes de NH_3 sont listées dans le Table 3.1.

Dans chaque cas, des échantillons fraîchement synthétisés ont été utilisés. Dans cette étude, la quantité de NH_3 a été rapportée en masse (µg) plutôt qu'en unités de concentration (par ex. µg/mL), et la quantité totale de NH_3 a été calculée en additionnant les quantités mesurées dans l'électrolyte (30 mL) et dans le piège (5 mL). Fait intéressant, à l'exception des conditions de potentiel en circuit ouvert (OCP), du NH_3 a été détecté à tous les potentiels appliqués. Initialement, la production de NH_3 augmente lorsque le potentiel de l'électrode devient plus négatif jusqu'à -0,6 V vs. RHE, puis diminue à des potentiels plus négatifs (Figure 3.13 a). La quantité maximale de NH_3 a été de 19,5 µg à -0,6 V vs. RHE. Ces résultats suggèrent que l'activité NRR de l'échantillon Ag_3Sn/ACC dans l'électrolyte neutre de K_2SO_4 0,5 M est maximale à -0,6 V vs. RHE. La tendance observée dans ce graphique est cohérente avec plusieurs études ayant rapporté une activité NRR pour des catalyseurs en solution aqueuse.

Cependant, il est crucial de vérifier que la source de NH_3 provient bien de la réduction de N_2 à la surface du catalyseur. Pour ce faire, quatre tests de contrôle ont été effectués dans une solution de K_2SO_4 0,5 M en utilisant des échantillons fraîchement synthétisés pour chacun.

Dans le premier test de contrôle, l'échantillon Ag_3Sn/ACC a été immergé dans la solution de K_2SO_4 et purgé à l'N_2 pendant 18 heures sans appliquer de potentiel (conditions de circuit ouvert). Dans le deuxième test, la même procédure a été suivie en utilisant l'Ar au lieu du N_2. Dans les deux cas, la quantité de NH_3 dans l'électrolyte et dans le piège était inférieure à la limite de détection. Cela confirme que les gaz de purge (N_2 et Ar) étaient exempts de NH_3 et qu'aucune contamination mesurable en NH_3 ne provenait de l'équipement du laboratoire (par ex., gants en nitrile, conduites de gaz ou verrerie).

Pour le troisième test de contrôle**,** une électrode ACC a été utilisée en remplacement d'une électrode Ag_3Sn/ACC, et un potentiel de -0,6 V vs. RHE a été appliqué. Dans ce cas (Figure 3.13c), 4,5 µg et 3,5 µg de NH_3 ont été produits respectivement sous purge de gaz N_2 et Ar, soit une diminution significative par rapport aux 19,5 µg obtenus avec Ag_3Sn/ACC au même potentiel et sous purge de N_2. Ces résultats suggèrent, à ce stade, que le Ag_3Sn est responsable de la production de NH_3.

Lors du quatrième et dernier test de contrôle, le système a été purgé avec de l'Ar au lieu de N_2. Dans ce cas, le potentiel appliqué a été varié, en utilisant des électrodes Ag_3Sn/ACC fraîchement préparées à chaque potentiel. Comme le montre la Figure 3.13, la présence de NH_3 a été observée à tous les potentiels testés sous Ar, avec des valeurs comparables à celles détectées sous N_2. Au potentiel où la production de NH_3 était maximale (19,5 µg à $-0,6$ V vs. RHE), la quantité mesurée sous Ar a été de 22,0 µg, dépassant ainsi celle produite lorsque le gaz N_2 était injecté dans le système (Figure 3c). Les résultats obtenus suggèrent la présence d'espèces azotées à la surface de la cathode, capables d'être converties en NH_3 sous l'application d'un potentiel. Par conséquent, la production de NH_3 se fait par la réduction d'espèces azotées préexistantes à la surface de la cathode, et non par la réduction directe du gaz N_2. Dans l'ensemble, les résultats dans les solutions de KOH 2 M et de K_2SO_4 0,5 M ont montré que l'alliage Ag_3Sn est inactif pour l'électroréduction du N_2 en NH_3 (NRR) dans ces solutions aqueuses.

Un défi majeur dans le domaine de l'électrocatalyse aqueuse de la NRR concerne la prévalence de faux positifs. Alors que certains chercheurs affirment que la NRR en solutions aqueuses est réalisable et peut même atteindre une efficacité faradique et des taux de rendement élevés sur certains catalyseurs, d'autres affirment que ces mêmes matériaux sont totalement inactifs pour la NRR. La divergence observée entre les résultats obtenus par les différents groupes est très

probablement attribuable aux faux positifs, ce qui souligne la nécessité de respecter des protocoles expérimentaux rigoureux pour confirmer l'activité d'un catalyseur en NRR.

Dans la présente étude, il a été déterminé que lorsqu'un test de 18 heures était réalisé deux fois sur un même échantillon, la production de NH_3, qui atteignait 19,5 µg à -0,6 V vs. RHE dans K_2SO_4 0,5 M lors du premier test, tombait en dessous de la limite de détection lors du second test, et ce indépendamment du gaz de purge utilisé. Cette observation indique que la production de NH_3 n'est pas associée à la réduction du N_2, mais bien à la réduction d'espèces azotées contenues dans l'électrode. La quantité finie de ces espèces azotées réductibles explique pourquoi la production de NH_3 ne peut pas être maintenue sur une longue durée.

Au vu de ces observations, il est proposé de mettre en œuvre un test de contrôle économique pour identifier les faux positifs en NRR. Ce test consisterait à réaliser au moins deux essais successifs en utilisant la même électrode et les mêmes conditions expérimentales, suivis d'une analyse comparative des résultats obtenus. En effet, une diminution de la production de NH_3 observée au fil des tests successifs pourrait être le signe d'une variation temporelle de l'activité de l'électrode. Cependant, cette baisse pourrait également être le signe d'un faux positif, lié à la concentration limitée d'espèces azotées présentes dans l'électrode et pouvant être réduites en NH_3. Dans un domaine comme la NRR, où les faux positifs sont nombreux, cette possibilité ne doit pas être négligée.

En outre, il est recommandé d'utiliser des électrodes fraîchement synthétisées pour chaque test réalisé à différents potentiels en présence d'Ar et de N_2, afin de mieux contrôler les erreurs liées à la réduction de contaminants azotés en NH_3. Cela est particulièrement conseillé si la même électrode est d'abord utilisée pour un test sous N_2 puis sous Ar. Les résultats de la présente étude, en accord avec ceux d'autres chercheurs, suggèrent qu'un nombre considérable de faux positifs peut être identifié par une approche méthodologique consistant d'abord à réaliser le test sous Ar, une procédure relativement peu coûteuse, suivie des tests plus onéreux au $^{15}NH_3$, à condition qu'aucune détection de NH_3 ne soit observée lors du test de contrôle sous Ar.

La partie suivante est consacrée aux études théoriques visant à comprendre les raisons de l'inactivité de l'Ag_3Sn vis-à-vis de la NRR. La NRR commence par l'adsorption de N_2 sur la surface de l'Ag_3Sn (001) en tant qu'étape non électrochimique. La structure de l'Ag_3Sn (001) est présentée dans la Figure 3.14.

Afin de trouver la configuration énergétique minimale, nous avons examiné 11 sites d'adsorption différents tels qu'illustrés dans la Figure 3.14 c. L'énergie libre d'adsorption calculée pour N_2 (*) sur la surface de l'Ag_3Sn est de 0,21 eV, en pente ascendante dans le diagramme d'énergie libre (Figure 3.15). De plus, la longueur de liaison N≡N est restée inchangée à 1,10 Å, comparée à celle calculée pour la molécule de N_2 isolée, ce qui indique l'absence d'interaction entre la surface et N_2. Par ailleurs, la densité d'états projetée (PDOS) confirme qu'il n'existe aucune interaction entre la surface d'Ag_3Sn et N_2, puisqu'aucune modification significative des états p de N_2 n'est observée (Figure 3.16).

L'analyse de charge de Bader montre également qu'il n'y a aucun transfert de charge entre $*N_2$ et Ag_3Sn. L'interaction faible entre N_2 et Ag est attendue en raison de ses états d situés à basse énergie (Figure 3.16). Cependant, certaines études ont rapporté une interaction forte entre les états p des éléments du bloc p, comme Sn, et N_2. C'est pourquoi nous avons calculé l'adsorption de N_2 sur la surface du β-Sn (100), en considérant neuf sites d'adsorption différents (Figure 3.14 f). L'énergie libre d'adsorption calculée a toutefois été de 0,25 eV, ce qui traduit un processus endergonique et une interaction faible entre N_2 et Sn. Cette constatation contraste avec les rapports précédents suggérant une adsorption plus favorable de N_2 sur les catalyseurs à base de Sn.

L'étape suivante de la NRR est l'hydrogénation de $*N_2$ en *NNH, qui est en pente ascendante de 2,08 eV en énergie libre sur la surface de l'Ag_3Sn. La deuxième étape électrochimique est l'hydrogénation de *NNH en $*NNH_2$ ou *NHNH, ce qui permet de distinguer entre les voies distale et alternée, respectivement. La formation de *NHNH est moins ascendante en énergie libre que celle de $*NNH_2$, et il est donc attendu que la NRR progresse via la voie alternée sur la surface de l'Ag_3Sn. Comme le montre la Figure 4a, toutes les étapes de transfert proton-électron deviennent exergoniques après la deuxième étape d'hydrogénation, pour les voies distale et alternée. Enfin, la désorption du NH_3 de la surface est exergonique, ce qui était attendu en raison de la faible interaction entre la surface et N_2.

Nous avons évalué $U_{limiting}$ en considérant la variation d'énergie libre la plus importante parmi les étapes électrochimiques, ce qui fait de la transition $*N_2 \rightarrow$ *NNH l'étape limitante en potentiel (PLS) de la NRR globale. La forte variation d'énergie libre associée à la PLS est due à la mauvaise activation de N_2 à la surface de l'électrocatalyseur. La configuration énergétique minimale de tous les intermédiaires de la NRR sur la surface de l'Ag_3Sn est montrée dans la Figure 3.17.

Nous avons également caractérisé le profil d'énergie libre pour les voies distale et alternée sur la surface du β-Sn (100) (Figure 3.15). Comme mentionné précédemment, l'adsorption de N_2 est endergonique sur β-Sn (100), de manière similaire à celle observée sur la surface de l'Ag_3Sn, ce qui conduit à une forte variation d'énergie libre pour la première étape électrochimique. L'étape $*N_2 \rightarrow *N_2H$ est en pente ascendante de 2,31 eV, et constitue l'étape limitante en potentiel (PLS) sur β-Sn (100). De manière analogue à l'Ag_3Sn, la formation de *NHNH est moins ascendante en énergie libre que celle de $*NNH_2$, ce qui rend la voie alternée plus favorable sur β-Sn (100). Toutes les autres étapes électrochimiques ainsi que la désorption du NH_3 sont descendantes en énergie libre. Nous comparons $U_{limiting}$ pour Ag_3Sn (001), β-Sn (100) et Ag (111) dans la Figure 3.15. Malgré une valeur légèrement inférieure de Ulimiting de −2,08 V pour Ag_3Sn par rapport à −2,31 V pour β-Sn (100) et −2,74 V pour Ag (111), nous prévoyons que l'alliage Ag_3Sn est inactif pour la NRR car il nécessite encore des surtensions élevées ($\eta_{théorique}$ = −2,14 V), à des valeurs où la HER domine.

Pour améliorer l'activité catalytique et la sélectivité d'un électrocatalyseur, il convient de moduler les propriétés électroniques du site actif. Comme discuté précédemment, l'alliage constitue une stratégie simple mais efficace pour modifier la structure électronique des sites actifs. Cependant, dans notre cas, l'alliage n'a pas permis d'améliorer significativement l'activité, ce qui peut être mieux compris en examinant la structure électronique du site actif, c'est-à-dire la PDOS de l'Ag_3Sn et du β-Sn (100). La Figure 3.18 compare la PDOS des états p de Sn dans l'alliage Ag_3Sn et sur la surface Sn (100). Comme le montre la figure, il n'y a pas de changement substantiel dans la PDOS du Sn, sauf un léger décalage vers le haut des états p du Sn dans l'alliage, par rapport au Sn (100) pur, ce qui est cohérent avec l'analyse de charge de Bader, qui révèle un transfert net de 0,20 e^- du Sn vers les atomes d'Ag voisins. Bien que Sn soit légèrement plus électronégatif que Ag (1,96 vs. 1,93 sur l'échelle de Pauling), la coordination de surface du Sn avec six atomes d'Ag provoque un transfert de charge du Sn vers Ag. Ces résultats indiquent que l'alliage du Sn avec Ag ne module pas efficacement la structure électronique du Sn ou de l'Ag pour améliorer l'activité catalytique de l'Ag_3Sn. L'efficacité de l'alliage dépend de manière critique du choix des métaux, puisque la modulation de la structure électronique découle principalement du transfert de charge interatomique. Il convient de noter que l'alliage des métaux de transition d avec des métaux du bloc p ne conduit pas nécessairement à des changements substantiels des propriétés électroniques du site actif.

1.4 Deuxième projet : NRR assistée par ultrasons

1.4.1 Préparation du système

La cellule électrochimique a été placée dans un bain à ultrasons conventionnel à l'aide d'un support personnalisé. La cellule électrochimique a été continuellement purgée avec différents types de gaz à un débit de 20 mL min^{-1}. Le gaz de purge a été purifié en le faisant passer à travers une série de pièges à gaz. Le premier piège contenait 500 mL de H_2SO_4 1 M pour éliminer les traces de NH_3. Il était suivi d'un piège de 30 mL contenant 1 M $KMnO_4$ et 1 M KOH pour capturer les espèces NO_x. Le piège final, placé juste avant l'entrée du gaz dans la cellule électrochimique, contenait 20 mL de solution de Na_2SO_4 0,5 M. Chaque gaz a été purgé dans la cellule électrochimique pendant 30 minutes avant le début de l'expérience.

L'électrolyte consistait en 30 mL de Na_2SO_4 0,5 M, avec des quantités variables de PTFE testées. La cathode était un morceau de feuille de cuivre de 1 × 1 cm^2 utilisé sur les deux faces, et l'anode était une grille de platine de 2 × 2 cm^2. Avant chaque expérience, la cathode en cuivre a été polie mécaniquement puis nettoyée par traitement ultrasonique dans de l'acétone pendant 10 minutes afin d'assurer une surface propre. Une cellule électrochimique à compartiment unique, constituée d'un bécher de 100 mL rempli de 30 mL d'électrolyte, a été placée dans un bain à ultrasons.

Au cours de chaque expérience, la densité de courant à la cathode en cuivre a été maintenue à −10 mA/cm^2. Les expériences ont été réalisées dans des conditions variées afin d'évaluer l'effet de différentes concentrations de PTFE (0, 10, 20, 60, 100 et 200 mg). Les effets de la présence ou de l'absence de traitement ultrasonique ainsi que la composition du gaz de purge ont été étudiés. Les environnements gazeux comprenaient des mélanges 50:50 de N_2 + Ar et d'air + Ar, ainsi que N_2 pur, Ar pur et air pur. Toutes les expériences ont été menées pendant une heure. Pour évaluer la stabilité dans le temps, la production d'ammoniac a été mesurée après 30 minutes, 1 heure et 2 heures lors des tests de durabilité.

1.4.2 Mesure de l'ammoniac

La méthode du salicylate mentionnée précédemment a été utilisée pour mesurer la quantité de NH_3 après chaque test. Une courbe d'étalonnage a été générée à l'aide de standards de NH_4Cl à des concentrations de 0,5, 1, 2, 3 et 7 µg/mL, chacun préparé dans une solution de Na_2SO_4 0,5 M.

Le NO_2^- a été quantifié à l'aide d'un kit de test des nitrites. Tout d'abord, 35 mg de réactif ont été ajoutés à 3 mL d'électrolyte après l'expérience. Ensuite, le mélange a été incubé dans l'obscurité pendant 10 minutes pour permettre le développement de la couleur. Une courbe d'étalonnage a été établie en préparant des solutions de KNO_2 à des concentrations de 0,05, 0,5 et 1 µg/mL dans Na_2SO_4 0,5 M et en mesurant leur absorbance UV-Vis à 540 nm. Pour détecter le NO_2^- dans les électrolytes contenant différentes quantités de PTFE, l'échantillon a été dilué sept fois avec Na_2SO_4 0,5 M avant chaque mesure.

1.4.3 Résultats et discussion

La Figure 4.1 montre les courbes d'étalonnage utilisées pour mesurer les quantités de NO_2^- et NH_4^+. Tout d'abord, la propreté du système a été vérifiée en purgant séparément les gaz N_2, Ar et l'air dans la solution pendant 1 heure chacun, sans appliquer de potentiel. Les concentrations de NO_2^- et NH_4^+ étaient toutes deux inférieures à la limite de détection, ce qui indique que les gaz de purge et la cellule électrochimique étaient exempts de contamination.

Ensuite, l'effet de la sonication et de diverses additions de PTFE sur la production de NO_2^- dans un électrolyte 0,5 M Na_2SO_4 a été étudié. La sonication a été réalisée pendant une heure sous un mélange gazeux 50:50 d'azote (N_2) et d'argon (Ar) avec différentes quantités de PTFE ajoutées à l'électrolyte. Un mélange d'argon (Ar) et d'azote (N_2) a été utilisé car il a été proposé que l'Ar puisse intensifier l'activation de N_2 en raison de sa capacité thermique plus élevée. Cela augmente la température des bulles pendant la cavitation, favorisant la formation de radicaux et la production de NO_x^-. Avec le PTFE, cette augmentation de température peut également aider à surmonter les barrières d'énergie de surface pour le transfert d'électrons. Dans ces expériences, aucun potentiel électrochimique n'a été appliqué.

La concentration de NO_2^- était de 0,14 µg/mL sous sonication en l'absence de PTFE. Des études antérieures ont examiné la formation de NO_2^- sous traitement ultrasonique sans PTFE lors de purges avec N_2 ou l'air. Les mécanismes exacts sont encore à l'étude, mais ce phénomène est généralement attribué aux températures et pressions locales extrêmes générées lors de la cavitation acoustique. Cependant, l'activation directe de N_2 dans les systèmes sonochimiques sans intervention des radicaux dérivés de l'oxygène a été remise en question en raison de la haute énergie d'activation et de la grande stabilité thermodynamique de N_2. Des études antérieures ont démontré que la présence d'oxygène moléculaire est essentielle pour l'activation de N_2 et la formation de NO_x^-. Les températures et pressions locales extrêmes générées lors de

la cavitation acoustique en présence de molécules d'O_2 provoquent la rupture homolytique des molécules H_2O et O_2. Les espèces réactives de l'oxygène (ROS) résultantes, telles que les radicaux OH• et O_2•, peuvent réagir avec l'azote moléculaire pour former des espèces NO_2^-. Dans notre système, nous avons émis l'hypothèse que, lors de la purge avec des gaz inertes (N_2 ou Ar), l'O_2 nécessaire à la génération de ROS provient de l'atmosphère environnante à l'interface liquide-air. Pour vérifier cette hypothèse, nous avons scellé le bécher de sonication pour éliminer le contact avec l'air. La formation de NO_2^- a diminué de manière significative dans les systèmes scellés purgés avec N_2 ou Ar, atteignant presque les niveaux de base (0,03 µg/mL après une heure).

Ces résultats confirment que l'O_2 atmosphérique est un précurseur clé de la formation de NO_2^- dans les systèmes sonochimiques. Sauf indication contraire, tous les tests ont été réalisés à l'air libre.

L'ajout de 10 mg de PTFE a augmenté la production de NO_2^- d'environ 26 fois, atteignant 3,6 µg/mL (voir Figure 4.2). Cette augmentation significative peut être due à l'augmentation de la génération de ROS lors de l'électrification par contact de l'eau avec le PTFE. Ces radicaux peuvent oxyder N_2, entraînant la formation d'espèces NO_x^-. Cependant, l'augmentation supplémentaire de la quantité de PTFE a entraîné une diminution de la production de NO_2^-. La quantité de NO_2^- a diminué de moitié lorsque la quantité de PTFE est passée de 10 mg à 20 mg, et elle a progressivement décliné jusqu'à 0,9 µg/mL avec 100 mg de PTFE. Fait intéressant, à une charge de PTFE de 200 mg, le NO_2^- n'était plus détectable. Une relation inverse similaire à de fortes charges de PTFE a été rapportée dans d'autres applications, telles que la génération de H_2O_2 assistée par PTFE. En l'absence de tensioactif, il a été proposé que des quantités excessives de PTFE puissent entraîner une accumulation d'électrons à l'interface eau-PTFE. Cela pourrait influencer la dynamique de charge interfaciale, entravant la formation supplémentaire de radicaux, essentielle pour la progression des réactions chimiques. L'ajout de tensioactifs pour améliorer la dispersion du PTFE pourrait prévenir cette accumulation de charge. Cependant, cette étude n'a pas utilisé de tensioactif afin de ne pas interférer avec la réaction. Par conséquent, la poudre de PTFE est restée à la surface du liquide au lieu de se disperser dans la solution. L'accumulation excessive de particules de PTFE à la surface du liquide obstrue très probablement la diffusion de l'O_2 atmosphérique dans la solution, contribuant ainsi à la diminution de la concentration de NO_2^- aux plus fortes teneurs en PTFE. Sur la base de ces résultats, la condition optimale pour maximiser l'activation de N_2 en vue de la production ultérieure de NH_3 a été

identifiée comme l'ajout de 10 mg de PTFE à 30 mL de Na_2SO_4 0,5 M. Cette quantité a été utilisée dans toutes les expériences suivantes.

Toutes les expériences ont été réalisées dans une solution de Na_2SO_4 0,5 M. Cependant, la formation potentielle de NO_2^- a également été étudiée dans une solution plus concentrée de Na_2SO_4 1 M. Fait intéressant, la concentration de NO_2^- est tombée en dessous de la limite de détection dans la solution concentrée. Une tendance similaire a été rapportée pour la production de H_2O_2 via la contact-électro-catalyse sur le polytétrafluoroéthylène (PTFE) à fortes concentrations ioniques. Cet effet a été attribué à l'influence négative des anions excessifs dans la solution qui captent les radicaux OH•, ainsi qu'à l'adsorption ionique à la surface du PTFE, ce qui entrave le transfert d'électrons et supprime ainsi la génération de radicaux. De plus, il a été démontré que des concentrations élevées de Na_2SO_4 réduisent la solubilité de l'Ar dans la solution, entraînant une diminution du nombre de radicaux réactifs.

Ensuite, la réduction électrochimique a été réalisée dans un bécher ouvert de 100 mL contenant 30 mL d'une solution de Na_2SO_4 0,5 M, placé dans un bain à ultrasons. Une densité de courant constante de -10 mA/cm² a été appliquée à la cathode en feuille de cuivre, et un flux continu d'un mélange gazeux N_2:Ar 50:50 a été maintenu tout au long de l'expérience. Le cuivre a été choisi comme cathode car c'est un catalyseur bien connu pour la réduction de NO_3^- en NH_3. Bien que l'activité puisse être améliorée par des modifications telles que l'alliage, ce n'était pas l'objectif de la présente étude. Il convient de noter que le catalyseur choisi doit également posséder une grande stabilité mécanique et chimique afin de résister aux conditions sévères du traitement par ultrasons.

Une série de tests a été réalisée sous différentes conditions expérimentales tout en maintenant la densité de courant constante à -10 mA/cm².

La quantité d'ammoniac produite sur la feuille de cuivre restait inférieure à la limite de détection à -10 mA/cm² lorsque le traitement ultrasonique était absent et que l'atmosphère était un mélange Ar:N_2 50:50. De même, passer à l'azote pur comme gaz de purge a donné des niveaux indétectables de NH_3. Ces résultats étaient prévisibles, étant donné les défis bien connus associés à la réduction électrochimique de l'azote en milieu aqueux. La forte compétition de la réaction d'évolution de l'hydrogène (HER) et la faible activité du cuivre pour la NRR rendent la formation de NH_3 peu probable.

Un taux de production de NH_3 de 0,52 µg/mL/h a été observé lors de la réduction électrochimique sans PTFE lorsque le traitement ultrasonique était appliqué. Pour confirmer la source de l'ammoniac, un test témoin a été réalisé en purgeant la cellule avec de l'argon (Ar) tout en maintenant une densité de courant de −10 mA/cm² sous conditions ultrasoniques. Dans ce cas, les niveaux de NH_3 restaient inférieurs à la limite de détection. Ces tests confirment que l'ammoniac observé a été généré par l'activation des molécules de N_2 via des voies sonochimiques et leur réduction sur la surface de Cu. Cette activation de l'azote, mise en évidence par la formation de NO_2^-, a été discutée précédemment.

À −10 mA/cm², l'application du traitement ultrasonique avec 10 mg de PTFE comme contact-électro-catalyseur a multiplié par 5,5 le taux de production de NH_3, atteignant 2,63 µg/mL/h (Figure 4.3). Cette augmentation substantielle correspond à la forte hausse de la formation de NO_2^- précédemment observée dans les mêmes conditions. Cela confirme que le PTFE joue un rôle clé dans l'activation de N_2, fournissant un plus grand nombre d'intermédiaires réductibles pouvant être convertis en NH_3 à la surface de la cathode. L'analyse post-réaction a montré que la concentration de NO_2^- est tombée à 0,02 µg/mL (Figure 4.5), indiquant que presque tout le NO_2^- a été consommé lors du processus électrochimique.

L'effet du gaz de purge a été étudié plus en détail en comparant le mélange N_2+Ar avec l'azote pur, l'air et un mélange air+Ar (Figure 4.11). En comparaison avec le mélange N_2+Ar (2,63 µg/mL/h), la purge avec N_2 pur a produit beaucoup moins de NH_3 (0,80 µg/mL/h). Cela peut être lié à l'augmentation de la formation de NO_x^- sous cavitation induite par l'Ar et sa réduction ultérieure à la cathode. Comparé au N_2, la purge avec l'air a diminué la production de NH_3 (0,48 µg/mL/h), probablement en raison de la pression partielle plus faible de N_2. L'introduction d'Ar dans l'air a augmenté le rendement (1,15 µg/mL/h), confirmant davantage l'effet positif de l'Ar.

Une expérience témoin a été réalisée en utilisant de l'argon pur (Ar) comme gaz de purge en présence de polytétrafluoroéthylène (PTFE) avec une densité de courant appliquée de −10 mA/cm². Le taux de production d'ammoniac résultant était de 0,12 µg/mL/h, bien inférieur au taux obtenu avec un mélange gazeux N_2:Ar 50:50 (2,63 µg/mL/h). Cette réduction significative confirme que la formation d'ammoniac dans des conditions standards résulte des effets combinés de la contact-électro-catalyse et de la réduction électrochimique. De plus, lorsque l'expérience a été répétée dans une cellule électrochimique scellée pour empêcher la diffusion de N_2 atmosphérique (alors que l'O_2 pouvait encore être fourni par l'oxydation de l'eau à l'anode), la

concentration de NH_3 est tombée en dessous de la limite de détection. Cela indique que le N_2 de l'air ambiant contribue également légèrement (0,12 µg/mL/h) à la réaction dans des conditions de cellule ouverte.

Il convient de noter que l'efficacité globale de cette conversion électrochimique pourrait être améliorée en optimisant les paramètres électrochimiques, les caractéristiques de l'électrode ou en modifiant la composition de l'électrolyte pour favoriser la réduction de NOx^- en NH_3. Cependant, ces optimisations dépassaient le cadre de cette étude de preuve de concept.

Ensuite, nous avons étudié si le NH_3 pouvait être produit uniquement par contact-électro-catalyse sans appliquer de potentiel externe à l'électrode de Cu. Pour tester cette hypothèse, nous avons introduit un mélange 50:50 de N_2 et Ar dans une solution de Na_2SO_4 0,5 M contenant 10 mg de PTFE. Nous avons ensuite soumis ce mélange à un traitement ultrasonique pendant une heure sans appliquer de courant à l'électrode de Cu. Aucun NH_3 détectable n'a été observé, indiquant que la contact-électro-catalyse seule ne produit pas de NH_3 dans ces conditions.

Ensuite, nous avons examiné si la contact-électro-catalyse pouvait oxyder le NH_3. Comme le montre la Figure 4.7 ,la sonication d'une solution de NH_3 à 1 µg/mL dans Na_2SO_4 0,5 M pendant 60 minutes sans appliquer de potentiel a entraîné une légère diminution de la concentration de NH_3 à 0,87 µg/mL. Cette diminution n'a été observée qu'en présence de PTFE ; aucune variation n'a été constatée sans celui-ci. Ces résultats suggèrent que la contact-électro-catalyse peut entraîner l'oxydation partielle de NH_3, probablement due à la génération de radicaux réactifs. Cependant, l'ampleur de l'oxydation est minimale et pourrait éventuellement être réduite par l'optimisation de paramètres tels que la composition de l'électrolyte, la conception de la cellule et la teneur en oxygène. Ces ajustements dépassaient le cadre de cette étude.

Sur la base de ces observations, nous proposons le mécanisme suivant pour la production de NH_3 lorsque la contact-électro-catalyse est combinée aux réactions électrochimiques (Figure 4.10). Il illustre l'activation de N_2, suivie de sa réduction à la surface de la cathode, conduisant à la formation de NH_3.

1.5 Conclusion

Le développement du procédé Haber–Bosch a marqué le début de la production industrielle d'ammoniac, permettant l'utilisation à grande échelle d'engrais qui a transformé l'agriculture mondiale. En conséquence, notre planète, estimée auparavant capable de soutenir environ 4 milliards de personnes, en soutient désormais plus de 8 milliards. Cependant, ce procédé dépendant des combustibles fossiles émet chaque année de grandes quantités de CO_2, motivant la recherche de voies alternatives pour la synthèse de l'ammoniac.

La production électrochimique d'ammoniac à partir de N_2 a émergé comme un concept prometteur, surtout lorsqu'elle est couplée à des sources d'énergie renouvelable. En principe, elle permet une génération directe de NH_3 dans une cellule électrochimique. Cependant, dans les électrolytes aqueux, la réaction compétitive d'évolution de l'hydrogène (HER) domine, entraînant de faibles rendements en NH_3. L'alliage s'est révélé être une stratégie efficace pour améliorer les réactions électrocatalytiques ; NO_xRR, HER, OER, CO_2RR ainsi que NRR.

Motivés par des rapports d'activité NRR raisonnable pour Ag et Sn, leur faible activité HER et la perspective d'une hybridation des orbitales p–d, nous avons synthétisé l'alliage Ag_3Sn par électrodéposition pulsée sur tissu de carbone activé. Cependant, contrairement aux attentes, aucune activité NRR réelle n'a été observée dans les solutions aqueuses. Dans une solution de 2 M KOH, une électrolyse de 18 heures à différents potentiels n'a produit aucun NH_3 détectable. Dans 0,5 M K_2SO_4, en raison d'une meilleure limite de détection pour NH_3, celui-ci a été détecté, notamment à des potentiels plus négatifs que −0,6 V vs. RHE, mais des quantités identiques ont également été observées lors des tests de contrôle avec Ar et des électrodes fraîchement préparées. Cela indiquait que le NH_3 détecté provenait d'espèces azotées dans le système électrochimique et non de la réduction électrochimique de N_2. Les calculs DFT ont confirmé cette conclusion : bien que Ag_3Sn présente un potentiel limite plus faible pour la NRR comparé au Ag ou Sn pur, les surtensions requises restent prohibitives. Globalement, l'activité NRR anticipée de Ag_3Sn n'a donc pas été confirmée.

Reconnaissant la difficulté fondamentale d'activer N_2 uniquement par réduction électrochimique en milieu aqueux, nous avons cherché à introduire une voie d'activation supplémentaire. Nous avons conçu une approche hybride combinant ultrasons et électrocatalyse et avons renforcé l'activation de N_2 en ajoutant du PTFE comme contact-électro-catalyseur. Cette méthode génère

des espèces azotées réactives avant la réduction électrochimique. Pour évaluer le degré d'activation, nous avons mesuré la formation de NO_2^- sous purge continue N_2 + Ar (50:50) sans potentiel appliqué. La sonication seule produisait 4,2 µg h^{-1} de NO_2^-, tandis que la présence de PTFE augmentait la production à 108 µg h^{-1}, démontrant son rôle significatif dans l'activation de N_2.

L'activation améliorée a conduit à une synthèse accrue de NH_3. À −10 mA cm^{-2} sur une cathode de cuivre, l'utilisation des ultrasons avec PTFE a permis d'obtenir 77,1 µg h^{-1} de NH_3, contre seulement 14,1 µg h^{-1} avec les ultrasons seuls. Sans ultrasons, le NH_3 restait indétectable, soulignant l'importance de l'activation de N_2. La composition du gaz était également critique : des quantités optimisées d'O_2 et d'Ar ont amélioré l'activation de N_2 et augmenté les rendements en NH_3, tandis que la purge à l'air ambiant ne donnait qu'une performance modeste. Les expériences de contrôle ont confirmé que le NH_3 provenait de la réduction électrochimique de N_2 activé, et non d'une conversion directe de N_2 en NH_3 par contact-électro-catalyse.

Dans l'ensemble, ce travail met en évidence deux points clés. Premièrement, Ag_3Sn, malgré les attentes basées sur des rapports antérieurs, n'a pas montré d'activité NRR mesurable dans les conditions aqueuses testées, et des protocoles de contrôle rigoureux sont essentiels pour éviter les faux positifs. Deuxièmement, le couplage des ultrasons avec la contact-électro-catalyse offre une stratégie viable pour surmonter le goulot d'étranglement de l'activation de N_2, permettant une augmentation significative de la production électrochimique de NH_3. Au-delà de la synthèse de l'ammoniac, cette approche hybride contrôlable pourrait être appliquée à d'autres transformations moléculaires difficiles.

1.6 Perspectives futures

Une revue de la littérature met en évidence à quel point le domaine de la réduction directe de l'azote (NRR) reste encore incertain. Bien que de nombreuses études rapportent des résultats prometteurs, soutenus par des mécanismes tels que le dopage, l'alliage ou l'ingénierie de l'électrolyte, des préoccupations sérieuses subsistent. Les tests de contrôle, comme le balayage à l'argon ou le marquage isotopique au $^{15}N_2$, ne sont pas toujours réalisés avec la rigueur nécessaire, et les calculs théoriques négligent souvent les réactions concurrentes telles que l'évolution de l'hydrogène (HER) ou la difficulté fondamentale de l'adsorption et de l'activation de N_2. En conséquence, les faux positifs sont fréquents, et plusieurs catalyseurs autrefois rapportés comme actifs se sont ensuite révélés dépourvus d'activité détectable pour la NRR. Cela a conduit

à une situation où, malgré le grand nombre de publications, la reproductibilité et la fiabilité des résultats demeurent des questions ouvertes.

À l'avenir, les progrès dans ce domaine dépendront moins de l'introduction rapide de nouveaux catalyseurs sans tests de contrôle rigoureux que du renforcement des bases mêmes de la recherche. La publication de résultats négatifs devrait être davantage valorisée, car elle permettrait d'éviter la répétition d'approches inefficaces.

De plus, les études futures pourraient bénéficier de l'exploration de directions allant au-delà de la conception catalytique conventionnelle**.** Bien que l'ingénierie des catalyseurs ait été centrale dans des domaines tels que la dissociation de l'eau ou la réduction du CO_2, elle pourrait ne pas suffire à elle seule pour la NRR. Des stratégies hybrides, comme l'approche sonoélectrochimique explorée dans cette thèse, pourraient constituer une solution possible pour activer la molécule d'azote (N_2) inerte. Bien que ce travail ait démontré la faisabilité d'une telle approche, la compréhension du mécanisme sous-jacent ainsi que les performances catalytiques pourraient être encore améliorées dans de futures études.

En termes d'amélioration des performances, plusieurs paramètres peuvent être optimisés. Les caractéristiques ultrasonores, en particulier la fréquence et la puissance, ont une forte influence sur la génération de radicaux et le taux de réaction. L'utilisation d'un système ultrasonore à sonde, plutôt qu'un bain, pourrait également être avantageuse, car il permet de produire une concentration plus élevée de radicaux réactifs. De plus, la composition de l'électrolyte et les propriétés de surface de la cathode favorisant l'activité NOxRR méritent une étude approfondie. Par ailleurs, les travaux futurs pourraient se concentrer sur l'ajustement de la configuration de la cellule, le test de nouveaux matériaux de cathode, l'exploration de différents gaz de purge, ainsi que l'introduction de tensioactifs pour augmenter la teneur en PTFE dans la solution. L'examen d'autres types de contact-électro-catalyse pourrait également s'avérer prometteur.

D'un point de vue mécanistique, l'amélioration des techniques d'analyse in situ permettant de détecter une gamme plus large de radicaux — incluant les espèces azotées ainsi que les radicaux OH, H et O — aiderait à clarifier le rôle spécifique de la cavitation dans la contact-électro-catalyse et son impact sur la formation de radicaux. En outre, bien que la réaction HER sonoélectrochimique ait été étudiée dans une certaine mesure, la contribution de la contact-électro-catalyse n'a pas encore été examinée. Il est également important de déterminer comment

certains cations ou anions présents dans l'électrolyte peuvent soit inhiber, soit favoriser la réactivité globale.

Les recherches dans ce domaine sonoélectrochimique présentent aussi leurs propres défis. L'environnement réactionnel sévère peut entraîner la dégradation de la cathode ou de l'anode si elles ne sont pas suffisamment stables. De plus, l'enregistrement des réponses électrochimiques sous ultrasons reste techniquement complexe, car les ondes acoustiques peuvent provoquer des fuites ou des interférences au niveau de l'électrode de référence, qui peut elle-même agir comme un site involontaire de contact-électro-catalyse. Surmonter ces limitations sera essentiel pour faire progresser à la fois la compréhension et l'application pratique des systèmes sonoélectrochimiques hybrides pour l'activation de l'azote.

En résumé, faire progresser la NRR en milieu aqueux nécessitera deux évolutions parallèles : d'une part vers une meilleure reproductibilité et fiabilité des mesures, et d'autre part vers une intégration plus créative de nouveaux procédés.

TABLE OF CONTENTS

ACKNOWLEDGEMENTS ..... **III**
RÉSUMÉ ..... **V**
ABSTRACT ..... **VII**
SOMMAIRE RÉCAPITULATIF ..... **IX**
RÉDUCTION ÉLECTROCHIMIQUE DE L'AZOTE EN MILIEU AQUEUX : DÉFIS ET STRATÉGIES CATALYTIQUES AMÉLIORÉES PAR ULTRASONS IX
1.1 CONTEXTE IX
1.2 OBJECTIFS ET STRUCTURE DE LA THÈSE XII
1.3 PREMIER PROJET : ACTIVITE ELECTROCHIMIQUE DE Ag_3Sn POUR LA NRR XIII
1.3.1 Activation du tissu de carbone et synthèse de Ag_3Sn xiii
1.3.2 Caractérisation physicochimique et électrochimique xiv
1.3.3 Mesure de l'ammoniac xv
1.3.3 Méthodes théoriques xvi
1.3.4 Résultats et discussion xvii
1.4 DEUXIÈME PROJET : NRR ASSISTÉE PAR ULTRASONS XXIV
1.4.1 Préparation du système xxiv
1.4.2 Mesure de l'ammoniac xxiv
1.4.3 Résultats et discussion xxv
1.5 CONCLUSION XXX
1.6 PERSPECTIVES FUTURES XXXI
TABLE OF CONTENTS ..... **XXXV**
LIST OF FIGURES ..... **XXXIX**
LIST OF TABLES ..... **XLI**
LIST OF SYMBOLS AND CHEMICAL FORMULA ..... **XLII**
1 INTRODUCTION **1**
1.1 FOSSIL FUELS AND ENERGY CONSUMPTION 1
1.2 AMMONIA APPLICATIONS AND CURRENT PRODUCTION METHOD 2
1.3 CARBON-FREE AMMONIA PRODUCTION METHODS 3
1.4 ELECTROCHEMICAL NRR IN AQUEOUS SOLUTIONS 6
1.4.1 Mechanism 6
1.4.2 Competing hydrogen evolution reaction 7
1.4.3 False positives in NRR and control tests 9
1.4.4 Selection of Ag-Sn for NRR study 13

1.5 INDIRECT NRR 15
1.5.1 NH_3 production by NO_x reduction 15
1.5.2 NO_XRR Electrocatalysts 17
1.5.3 Ultrasound-assisted N_2 breaking 18
1.5.4 Contact-electro-catalysis 20
1.6 THESIS OBJECTIVES AND STRUCTURE 23

2 EXPERIMENTAL 27
2.1 EXPLORING Ag_3Sn FOR ELECTROCHEMICAL NRR 28
2.1.1 Carbon cloth activation 28
2.1.2 Ag_3Sn electrodeposition 28
2.1.3 Physicochemical characterization 29
2.1.4 Electrochemical measurements 30
2.1.5 Ammonia measurement 31
2.1.6 Theoretical calculations 31
2.2 ULTRASOUND-ASSISTED NRR 32
2.2.1 Sonoelectrochemcial system 32
2.2.2 NH_3 and NO_2^- measurement 32

3 AG_3SN ALLOY FOR NITROGEN ELECTROREDUCTION 35
3.1 ABSTRACT 35
3.2 INTRODUCTION 36
3.3 RESULTS AND DISCUSSION 37
3.3.1 Ag_3Sn electrodeposition 37
3.3.2 NRR electrocatalytic performance 43
3.3.3 Computational results 49
3.4 CONCLUSION 57
3.5 EXPERIMENTAL SECTION 58
3.5.1 Materials 58
3.5.2 Carbon cloth activation 58
3.5.3 Ag_3Sn electrodeposition 58
3.5.4 Physicochemical characterization 59
3.5.5 Electrochemical measurements 59
3.5.6 Ammonia measurement 60
3.5.7 Density functional theory 61
3.5.8 NRR Mechanisms 62

4 SONOELECTROCHEMICAL PATHWAY TO AMMONIA SYNTHESIS 65

4.1 NOTE S1. PRODUCTION OF NH_3 UNDER DIFFERENT PURGING GASES 78
4.2 EXPERIMENTAL SECTION 79
4.2.1 Materials and reagents 79
4.2.2 System preparation 79
4.2.3 NH_3, NO_2^-, and NO_3^- measurement and FE% calculation 80
5 CONCLUSION 83
5.1.1 Future perspective 84
6 BIBLIOGRAPHY 87

LIST OF FIGURES

FIGURE 1.1 PROPOSED ROADMAP OF THE AMMONIA ECONOMY. 6

FIGURE 1.2. THE POSSIBLE REACTION MECHANISM OF NRR. 7

FIGURE 1.3 VOLCANO PLOTS COMPARING THE LIMITING POTENTIALS OF HER AND NRR. 8

FIGURE 1.4 ELECTROCHEMICAL ROUTES TO NH_3/NH_4^+ 15

FIGURE 1.5 PUBLICATION TRENDS FOR NRR AND NO_xRR TO NH_3 17

FIGURE 1.6 THE DIFFERENCE BETWEEN THE LIMITING POTENTIALS FOR NO_3RR AND HER, ... 18

FIGURE 1.7 CONCENTRATIONS OF NO_2^-, NO_3^-, AND H_2O_2 GENERATED SONOCHEMICALLY. 20

FIGURE 1.8 A PROPOSED MECHANISM OF CONTACT-ELECTRO-CATALYSIS DURING ULTRASONICATION. 21

FIGURE 1.9 EXPERIMENTAL SETUP SCHEMATIC FOR HNO_3 SYNTHESIS. 23

FIGURE 2.1 METHODOLOGICAL FLOWCHART SUMMARIZING THE EXPERIMENTS PERFORMED. 27

FIGURE 3.1 SCHEMATIC OF THE ELECTRODEPOSITION BATH. 38

FIGURE 3.2 SCANNING ELECTRON MICROSCOPE (SEM) IMAGES AT DIFFERENT MAGNIFICATION 38

FIGURE 3.3 IMAGES OF WATER DROPLET DEPOSITED ON CARBON CLOTH: 39

FIGURE 3.4 SEM IMAGES OF THE ELECTROCHEMICALLY ACTIVATED CARBON CLOTH. 39

FIGURE 3.5 SEM IMAGES OF AG-SN: 40

FIGURE 3.6 ENERGY-DISPERSIVE X-RAY SPECTROSCOPY ELEMENTAL MAPPING OF AG-SN. 40

FIGURE 3.7 SEM IMAGES OF AG-SN PULSE ELECTRODEPOSITED ON ACTIVATED CARBON CLOTH. 41

FIGURE 3.8 (A-C) SEM IMAGES OF THE AG-SN COATING ON ACTIVATED CARBON CLOTH; 42

FIGURE 3.9 XRD PATTERN OF THE SYNTHESIZED Ag_3Sn ON ACTIVATED CARBON CLOTH SUBSTRATE. 43

FIGURE 3.10 SCHEMATIC (TOP) AND PHOTOGRAPH OF THE SYSTEM (BOTTOM) 44

FIGURE 3.11 CALIBRATION CURVES USED TO DETECT NH_3 45

FIGURE 3.12 CHRONOAMPEROMETRIC CURVES OF THE Ag_3Sn/ACC SAMPLES. 45

FIGURE 3.13 AMOUNT OF NH_3 AFTER THE 18-HOUR TEST. 46

FIGURE 3.14 (A, B) TOP AND SIDE VIEWS OF Ag_3Sn (100) STRUCTURE, RESPECTIVELY. 50
FIGURE 3.15 FREE ENERGY PROFILES OF THE DISTAL AND ALTERNATING PATHWAYS OF THE NRR. 51
FIGURE 3.16 THE PDOS OF Ag_3Sn, SHOWING D-STATES 52
FIGURE 3.17 MINIMUM ENERGY CONFIGURATION OF NRR INTERMEDIATES 53
FIGURE 3.18 PDOS OF INTO P-STATES FOR SN IN Ag_3Sn AND $\boldsymbol{\beta}$ −SN (100) 54
FIGURE 3.19 ADSORPTION FREE ENERGIES OF KEY INTERMEDIATES FOR COMPETING REACTIONS 56
FIGURE 3.20. FREE-ENERGY PROFILES 57
FIGURE 3.21 NRR ASSOCIATIVE MECHANISMS. 63
FIGURE 4.1. (A) UV-VIS SPECTRA OF VARIOUS 0.5 M Na_2SO_4 SOLUTIONS 68
FIGURE 4.2. (A) UV-VIS SPECTRA AND (B) THE CORRESPONDING BAR GRAPH 69
FIGURE 4.3. NH_3 YIELD RATE UNDER DIFFERENT CONDITIONS. 71
FIGURE 4.4. UV-VIS SPECTRA CORRESPONDING TO THE PRODUCED NH_3 UNDER DIFFERENT CONDITIONS. 71
FIGURE 4.5. UV–VIS SPECTRA CORRESPONDING TO 0.02 µG/ML OF NO_2^- DETECTED 72
FIGURE 4.6. (A) THE UV-VIS SPECTRA AND (B) THE CORRESPONDING NH_3 CONCENTRATION–TIME 73
FIGURE 4.7. UV-VIS SPECTRA SHOWING THE EFFECT OF CONTACT-ELECTRO-CATALYST 73
FIGURE 4.8. UV-VIS SPECTRA OF THE ELECTROLYTE REACTED WITH ZN POWDER 74
FIGURE 4.9 UV–VIS SPECTRA CORRESPONDING TO THE PRODUCED NH_3 75
FIGURE 4.10 SCHEMATIC OF THE SYSTEM AND PROPOSED MECHANISM FOR NH_3 PRODUCTION. 75
FIGURE 4.11. (A) UV-VIS SPECTRA AND (B) CORRESPONDING BAR GRAPH, ... 76
FIGURE 4.12 UV-VIS SPECTRA AND SHOWING THE AMOUNT OF NH_3 PRODUCED 77

LIST OF TABLES

TABLE 1.1 SELECTED PAPERS THAT REPORTED FALSE POSITIVES FOR NRR IN AQUEOUS SOLUTIONS.....11

TABLE 3.1 CONCENTRATION OF NH_3. 47

LIST OF SYMBOLS AND CHEMICAL FORMULA

ACC	Activated carbon cloth
Ag	Silver
Ag/AgCl	Silver/Silver chloride (reference electrode)
Ag_2SO_4	Silver sulfate
Ag_3Sn	Silver–Tin alloy
Ar	Argon
BEEF-vdW	Bayesian Error Estimation Functional with van der Waals correction
$C_5FeN_6Na_2O \cdot 2H_2O$	Sodium nitroferricyanide dihydrate
C_6H_6O	Phenol
$C_6H_9Na_3O_9 \cdot 2H_2O$	Sodium citrate dihydrate
$C_7H_6O_3$	Salicylic acid
CH_3COCH_3	Acetone
CO_2	Carbon dioxide
CO_2RR	Carbon dioxide reduction reaction
Cu	Copper
ΔG	Gibbs free energy change
DFT	Density Functional Theory
DI water	Deionized water
DOS	Density of States
E_0	Standard reaction potential
E_{DFT}	Electronic energy calculated by DFT
EDX	Energy-dispersive X-ray spectroscopy
FE	Faradaic efficiency
GPAW	Grid-based Projector Augmented Wave code
H_2	Hydrogen
H_2SO_4	Sulfuric acid
HER	Hydrogen evolution reaction
Hg/HgO	Mercury/Mercury oxide (reference electrode)
KNO_2	Potassium nitrite
$KMnO_4$	Potassium permanganate

KOH	Potassium hydroxide
K_2SO_4	Potassium sulfate
N_2	Nitrogen
NH_3	Ammonia
NH_4^+	Ammonium ion
NH_4Cl	Ammonium chloride
NO_2^-	Nitrite ion
NO_xRR	Nitrogen oxides reduction reaction
NRR	Nitrogen reduction reaction
NaClO	Sodium hypochlorite
Na_2SO_4	Sodium sulfate
NaOH	Sodium hydroxide
O_2	Oxygen
OER	Oxygen evolution reaction
PAW	Projector Augmented Wave method
PTFE	Polytetrafluoroethylene
RHE	Reversible Hydrogen Electrode
SEM	Scanning Electron Microscope
Sn	Tin
$SnSO_4$	Tin (II) sulfate
$U_{equilibrium}$	Equilibrium potential
$U_{limiting}$	Limiting potential
UV–Vis	Ultraviolet–visible spectroscopy
ZPE	Zero-point energy

1 INTRODUCTION

1.1 Fossil fuels and energy consumption

The terms "global warming", "fossil fuel problems", "greenhouse gases", and the "necessity of green energy replacement" have been repeated so many times that many people have almost become numb to them. Yet, the reality behind these terms is anything but abstract. Records of CO_2 emissions are still being broken year after year [1], and the scale of the crisis remains largely underestimated. Apart from increasing wildfires, droughts, and water crises, air pollution from fossil fuels alone causes an estimated 7 and 10 million premature deaths every year [2,3].

Replacing fossil fuels with green energy is essential, but energy consumption patterns (whether for daily life, transportation, or production of goods) are equally important. Considering energy use per capita, countries with high gross domestic product per capita (GDP/Capita), consume much more energy than low GDP/capita ones, while the extra energy consumed does not necessarily improve quality of life after some point [4,5]. This shows that energy use depends not only on basic needs but also on accessibility. In other words, when more energy is available, more is consumed. That is why fossil fuels replacement alone cannot solve the problem and unless consumption habits change, additional energy, fossil or renewable, will only fuel higher demand.

Renewable energies are not impact-free. The expansion of green energy systems requires material extraction, new infrastructure, and industrial production, all of which carry their own carbon and ecological footprints [6,7]. Moreover, switching to green energy will reduce CO_2 emissions from transportation and power, but it does not erase the impact of overconsumption. Even if factories run on renewables, producing more cars, clothes, and gadgets still means more waste, resource extraction, and pollution.

Overall, while the focus of this study is reducing reliance on fossil fuels, decarbonization cannot rely on technology alone. It must be accompanied by cultural change: educating people, reducing overconsumption, and using the potential of emerging social media to guide people toward sustainable lifestyles instead of actively promoting consumption [8]. Without this shift, we risk repeating the same cycle, greater supply leading to greater consumption, while ignoring the deeper root of the problem.

1.2 Ammonia applications and current production method

Ammonia (NH_3) is a colorless gas with a pungent odor, which is widely used in different chemicals production, from plastics to pharmaceuticals. However, its main application is in industrial fertilizers, estimated to provide food for 4 billion people worldwide [9]. Presently, most of the global NH_3 is produced by Haber-Bosch (H-B) process. This process was commercialized in 1913, making it the commercial standard for ammonia production.

In H-B process, N_2 reacts with H_2 at high pressures and temperatures. The majority of H_2 in this process is produced through steam methane reforming. H-B plants typically operate at 350–520 °C and 150–300 bar, using iron or ruthenium-based catalysts to facilitate the sluggish N_2 dissociation [10]. Maintaining such extreme conditions requires large fossil fuel inputs, both as feedstock for H_2 production and as the main energy source, making the process directly dependent on natural gas. Consequently, ammonia synthesis consumes about 1–2% of the world's total energy supply [11] and is releasing about 1.4% of the total world CO_2 emission each year [12]. The CO_2 emission is going to increase as the global demand for NH_3, to be used as a fertilizer, is estimated to increase 2.3% each year [13].

The reliance on natural gas has broader challenges beyond its environmental impacts. Natural gas price fluctuations can impact fertilizer prices directly, which subsequently affects food prices globally and thus also impacts the stability of agriculture. [14]. Furthermore, the concentration of H-B plants in certain geographic regions creates supply chain vulnerabilities [15], where disruptions can quickly affect fertilizer distribution and threaten food security worldwide. Ultimately, the Haber-Bosch process made the modern agricultural revolution possible but is not a sustainable process because of energy demands, carbon dioxide footprint, and input on fossil fuels. These drawbacks have led to research into alternatives, carbon-free ammonia production methods that can operate in milder climates and decouple the generation of NH_3 from fossil fuels.

Developing a clean method to produce carbon-free NH_3 will not only address these challenges but also open the doors to a new opportunity: to widely use ammonia as a carbon-free source of energy which is predicted to become the fuel of the future [16]. In comparison with the other carbon-free energy carrier (H_2), NH_3 has many advantages. Considering the boiling point of H_2 (-252.8 °C) and NH_3 (-33.3 °C) the liquefaction of NH_3 can be done much easier. Moreover, Piping and shipping liquefied NH_3 (as a fertilizer compound) is already widely used worldwide, so the costs of NH_3 transportation is much lesser than H_2 [17]. Interestingly, ammonia in liquid form

contains 50% more hydrogen by volume than liquefied hydrogen fuel, leading to 35% higher energy density [18]. Although these benefits theoretically position ammonia as a very promising energy carrier, for its applications some general limitations should also be noticed.

Practical challenges such as low flame speed, high ignition temperature, and NO_x formation after NH_3 combustion have been addressed in different ways in industrial processes [19]. To overcome the low flame speeds and high ignition temperatures, co-firing methods have been employed in which ammonia is co-fired with more reactive fuels, such as natural gas or hydrogen, which stabilize combustion and allow for ignition at lower temperatures.[20]. When NH_3 burns, it can produce either harmless N_2 or reactive nitrogen oxides (NO_X), depending on temperature and combustion conditions. There are engineering solutions available to help reduce these emissions, for example optimized burner designs, staged combustion, or catalytic systems such as selective catalytic reduction, that will convert NO_x into N_2 and H_2O and ensure efficient NH_3 combustion [21].

Furthermore, catalytic decomposition of ammonia into hydrogen and nitrogen (ammonia cracking) at the point of use makes it possible to feed the hydrogen produced into fuel cells or gas turbines [22]. Moreover, high-temperature fuel cells capable of directly utilizing ammonia are under development, achieving high electrical efficiencies without the energy losses linked to ammonia cracking [23]. Together, these approaches demonstrate that ammonia is not only a theoretical hydrogen carrier, but it can also be integrated into existing infrastructure, and support long-distance renewable energy transport and substantially reduce CO_2 emissions.

However, ammonia cannot be considered a truly carbon-free energy carrier if its production relies on processes that emit CO_2, such as conventional Haber–Bosch synthesis using fossil-derived hydrogen. For ammonia to be utilized as a sustainable fuel and chemical feedstock, production processes must be developed that minimize or otherwise eliminate carbon emissions from production. In this section, we describe the current pathways to either carbon-neutral or low-carbon ammonia, focusing on their pathways and practical implications.

1.3 Carbon-free ammonia production methods

Carbon-free NH_3 production can be generally categorized in three different pathways [16]:

Pathway 1, carbon sequestration: This method involves developing systems to capture and store the CO_2 emitted for H_2 production used in the H-B process. Clearly, this can increase the costs of

producing NH_3, but it can be considered a transitional stage to make a market for ammonia as a green fuel. Part of the costs in this method can be compensated when the social costs of CO_2 are considered [24]. Usually, amine-based absorption systems are used to absorb this CO_2 prior to the hydrogen entering the Haber-Bosch synthesis loop [25]. After being captured, the CO_2 is compressed and either converted, used for enhanced oil recovery or stored underground. This strategy has been used in a number of industrial projects. For example, "CF Industries" is developing a low-carbon ammonia facility in US that integrates carbon capture and storage technologies [26].

Pathway 2, clean production of H_2 to feed the Haber-Bosch system: In this approach, H_2 is produced in a clean method, and then it reacts with N_2 in the H-B process to produce carbon-free NH_3. Supplying the H-B process with hydrogen generated through polymer electrolyte membrane (PEM) electrolysis is currently at a technology readiness level (TRL) of 6–7 [13].

The process of polymer electrolyte membrane (PEM) electrolysis uses electricity to split water and produce hydrogen. Water is supplied to the anode in this system, where it undergoes oxidation to yield protons, electrons, and oxygen. While the electrons move via an external circuit, the protons move through a solid polymer electrolyte membrane to reach the cathode. Hydrogen gas is created at the cathode when protons are reduced by electrons [27].

Using a wind turbine, H_2 is produced by PEM electrolysis and converted to NH_3 by the H-B process on a small-scale (30 kg/day) in Siemens [16]. Substantial projects and investments are in progress worldwide, with China leading this change. Beginning operations in July 2025, the "Jilin Electric Power Da'an" project uses 800 MW of wind and solar power to produce 32,000 tonnes of green hydrogen and 180,000 tonnes of clean ammonia annually [28]. With an initial yearly capacity of 320,000 tonnes of green ammonia, "Envision Energy", a Chinese company has opened a sizable green hydrogen and ammonia facility in Mongolia. By 2028, the company intends to increase this capacity to 1.5 million tonnes annually [29].

This process, however, faces its own challenges: The costs of renewable, electrolytic hydrogen (USD 3-8/kg H_2) are much higher than the H_2 sourced from fossil fuels (USD 0.5-1.7/kg H_2) [30]. Another challenge is that the H-B process operates continuously, and interruptions in the feed gas can damage the equipment. Since H_2 from water splitting is powered by intermittent renewable sources such as solar and wind, supplying the H-B process with this fluctuating H_2 flow presents operational difficulties and ultimately increases production costs [31].

Pathway 3, electrochemical ammonia production directly from nitrogen: This method is still in TRL 1-3 [13], but has attracted research attention in recent years due to its high potential. Electrochemical NH_3 production systems can be powered by all kinds of renewable sources. It would not be damaged by the intermittency of power source and is able to produce ammonia in low scales, without the need for huge infrastructures of H-B process. In contrast to the H-B process, where only a few ppm of impurity in the feeding N_2 gas would damage the catalyst in use, impurities in N_2 may lower the efficiency but would not damage the equipment of electrochemically produced NH_3 in aqueous solutions [32].

As can be seen in Figure 1.1, In the NH_3 economy roadmap that was proposed by MacFarlane et al. [16], it has been predicted that the electrochemically produced NH_3 will enter the market around 2030 and then grow rapidly to a level that in 2040s, the NH_3 produced by electrochemical N_2 reduction considerably replace fossil fuels. In 2050, it is predicted that about 1.2 billion metric tons of ammonia will be produced annually, which is about eight times the ammonia produced in 2021 [33].

Despite the considerable promise of electrochemical nitrogen reduction (NRR) as a sustainable pathway for ammonia synthesis, its technological maturity remains limited to TRL 1–3, primarily due to the intrinsic complexity of the reaction. A comprehensive understanding of these limitations requires first a description of the NRR process. The subsequent subchapters therefore present the principles of electrochemical NH_3 production under ambient conditions in aqueous media and explore the key challenges impeding its advancement.

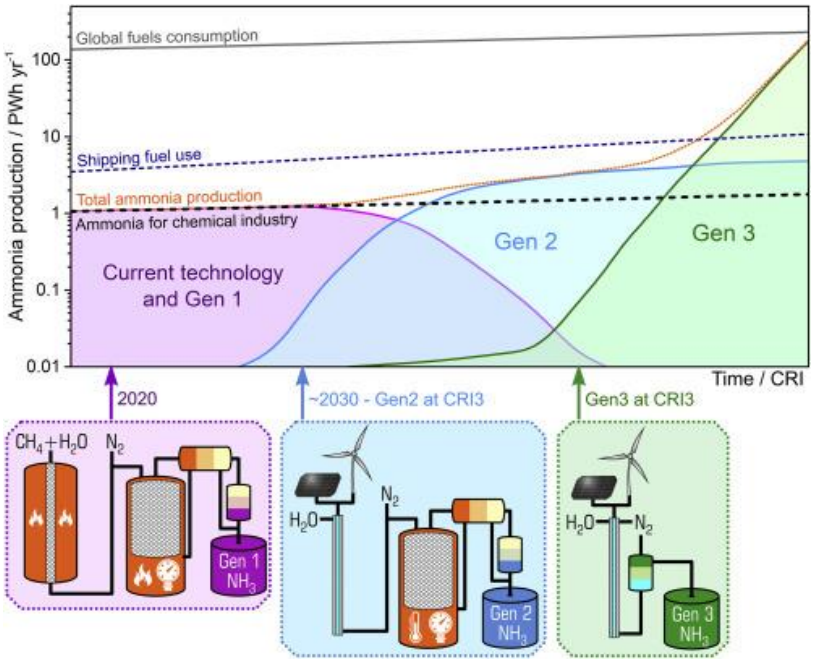


Figure 1.1 Proposed roadmap of the ammonia economy.

Schematic illustrating the projected contributions from existing methods and emerging ammonia production technologies: pathway 1 (purple), pathway 2 (light blue), and pathway 3 (green), reprinted with permission from reference [16]. Copyright (2021), Elsevier.

1.4 Electrochemical NRR in aqueous solutions

1.4.1 Mechanism

During NRR, nitrogen (N_2) is introduced into the electrolyte of an electrochemical cell, which can then be reduced at the cathode (negative electrode) to produce ammonia (NH_3) through the following reactions [34]:

$N_2 + 6H^+ + 6e^- \rightarrow 2NH_3$ (in acidic electrolyte) Equation 1.1

$N_2 + 6H_2O + 6e^- \rightarrow 2NH_3 + 6OH^-$ (in basic and natural electrolyte) Equation 1.2

Although the overall reaction seems straightforward, the conversion of N_2 to NH_3 involves multiple energy-intensive intermediate steps. Many reaction mechanisms have been proposed, but the detailed pathways of NRR are still complex and not fully understood [35]. It should be noted that for direct electrochemical NRR, these mechanistic pathways are still primarily theoretical. Because of the extremely low reaction rates, in-situ NH_3 detection limits, and contamination problems, direct experimental verification is still lacking. These difficulties, which will be covered in more detail later, have so far kept the suggested mechanisms from being definitively confirmed.

Nevertheless, NRR is generally classified into dissociative and associative pathways (Figure 1.2) [36,37]. In the dissociative pathway, the N≡N triple bond is cleaved first, generating two independent nitrogen atoms that adsorb onto the catalyst surface and are subsequently hydrogenated. This pathway requires a very large energy input and is typically associated with the H-B process under harsh conditions. Due to the high energy barrier, it is rarely accessible under ambient electrochemical conditions.

The associative pathway is more plausible for electrocatalytic NRR, as hydrogenation occurs before the N≡N bond is fully broken. Nitrogen adsorbs in an end-on configuration, meaning only one nitrogen atom interacts with the active site. Within this pathway, two main routes are recognized:

Associative distal pathway: The nitrogen atom farthest from the adsorption site is hydrogenated first to form NH_3. After the first NH_3 is released, the second nitrogen atom undergoes hydrogenation. Associative alternating pathway: Hydrogen atoms are added alternately to both nitrogen atoms, producing two NH_3 molecules through diazene ($*N_2H_2$) and hydrazine ($*N_2H_4$) intermediates [38].

Overall, associative distal and alternating pathways are proposed to be the primary routes for NRR under ambient electrocatalytic conditions, with the dissociative pathway being largely inaccessible.

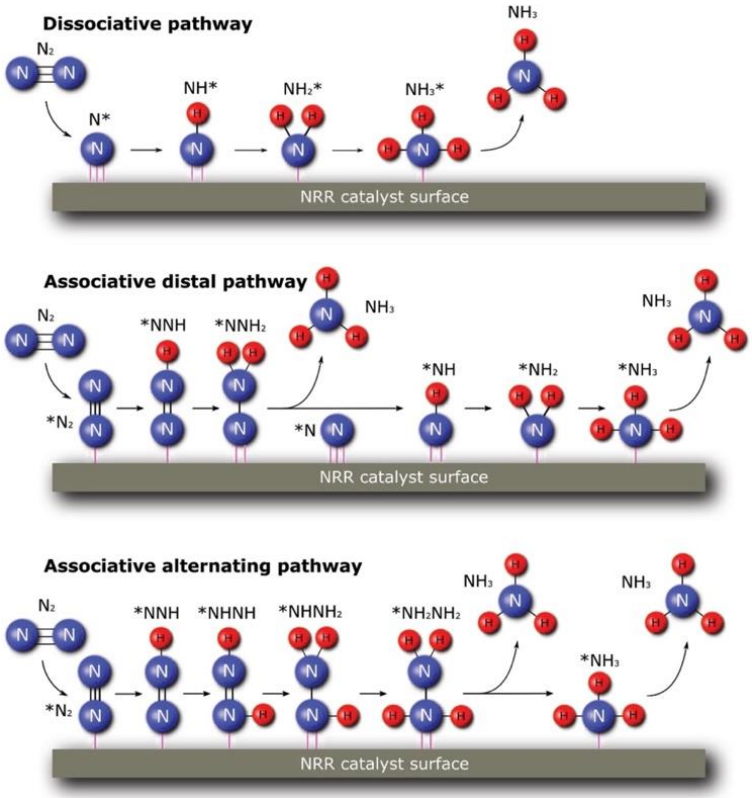


Figure 1.2. The possible reaction mechanism of NRR.

Schematic illustrating the dissociative pathway, associative distal, and associative alternating pathways. * Represents an adsorption site. Reprinted with permission from reference [37]. Copyright (2019), WILEY-VCH.

1.4.2 Competing hydrogen evolution reaction

One of the main challenges in aqueous nitrogen reduction reaction (NRR) is the competing hydrogen evolution reaction (HER), which generally proceeds at a much higher rate in aqueous solutions [39]. As illustrated in Figure 1.2, the NRR pathway begins with the adsorption of the N_2

molecule on the catalyst surface, followed by a series of proton–electron transfer steps. Each of these steps can be either thermodynamically favorable (downhill) or unfavorable (uphill). To ensure that all steps proceed downhill in free energy, an external potential known as the limiting potential (U_L), must be applied. As can be seen in Figure 1.3, Calculations of U_L for two different pure metal facets have shown that none of the studied metals are capable of initiating NRR before HER. In other words, the limiting potential for HER is consistently less negative than that for NRR, meaning HER turns on earlier and dominates the reaction under typical electrochemical conditions for the studied metals [40].

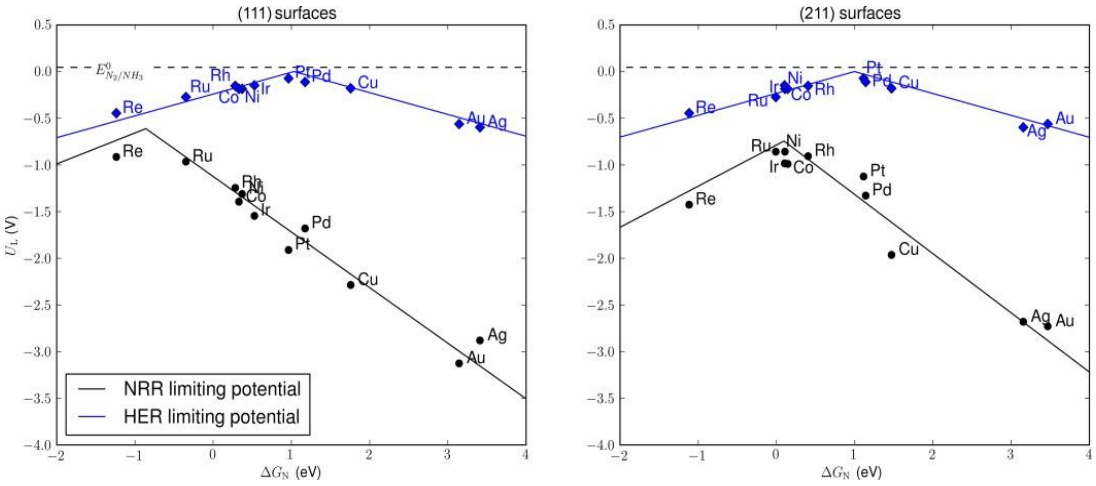


Figure 1.3 Volcano plots comparing the limiting potentials of HER and NRR.

The overpotentials for HER shown in blue and NRR in black, and each metal is labeled for the (111) surface on the left and the (211) surface on the right. Reprinted with permission from reference [40]. Copyright (2019), WILEY-VCH.

The NRR activity of different materials are usually compared by their NH_3 yield rate and faradaic efficiency (FE). Faradaic efficiency indicates the proportion of the total electrical current that contributes to producing ammonia, rather than being consumed to side reactions like hydrogen evolution through HER. In other words, it shows how efficiently the current is used for the desired chemical transformation [41].

Despite this prediction of HER dominance over NRR by many theoretical studies, experimental results have not always agreed with this picture, and in fact, have often been contradictory. On one side, many studies in recent years have reported measurable NRR activity for a wide range of metals and non-metals, with some reports even claiming high faradaic efficiencies at applied potentials less negative than the theoretically required limiting potential. To name just a few,

Mo_2N with a NH_3 yield rate of 78.4 μg h^{-1} mg_{cat}^{-1} and a FE of 4.5% at a potential of -0.3 V vs RHE, in 0.1 M HCl solution, with a potential determining step associated with a free energy barrier of 0.58 eV, [42], Ag nanosheet with a FE of 4.8% and a NH_3 yield rate of 4.62×10^{-11} mol s^{-1} cm^{-2} at -0.6 V vs RHE in 0.1 M HCl [43], Mo_2C with a FE of 8.13% and NH_3 yield of 95.1 μg h^{-1} mg^{-1}_{cat} at potential of −0.3 V, with an energy barrier calculated to be -1.15 eV [44]. There are also some even showing very large FE, higher than 50%, that proposes the reduction of inert N_2 easier than water reduction, including Au-Ni with a yield rate of 7.4 μg h^{-1} mg^{-1}_{cat} and FE of 67.8% at -0.14 V vs. RHE in 0.05 M H_2SO_4 solution, while their DFT calculation shows that the energy barrier is 1.13 eV, Au nanoparticles with a yield rate of 9.22 μg h^{-1} cm^{-2}, and FE of 73.32% in 0.1 M Li_2SO_4, and Bi nanocrystals with a NH_3 yield rate of 0.052 mmol cm^{-2} h^{-1} and 66% faradaic efficiency in 0.5 M K_2SO_4 solution [45–47].

However, even in the cases with high FEs, the NH_3 yields are still very low, leading to NH_3 concentration in a few parts-per-million (ppm) or lower than ppm range, where measurements are extremely sensitive to contamination and other experimental errors. This leads us to the next major challenge in NRR research: the false positives in NRR.

1.4.3 False positives in NRR and control tests

Many different sources of contamination can interfere with nitrogen reduction studies, and therefore several control tests have been defined to ensure that the measured NH_3 truly originates from N_2 reduction and not from external nitrogen species. The most widely accepted are: (i) Running the test at OCP under N_2 (ii) the Ar test, performed with and without applying a potential, and (iii) the $^{15}N_2$ isotope test, where this gas is purged into the solution, a potential is applied to the cathode and the resulting NH_3 is quantified to confirm that it is indeed $^{15}NH_3$. While nearly all reported NRR studies include at least some of these control tests, they are not always performed correctly. For example, Ar test duration is sometimes too short, background levels are not identified, or the the isotope labeling test is done only qualitatively instead of quantitatively, and without the purification of $^{15}N_2$ before the test, which can contain a lot of reducible ^{15}N contaminations that can lead to $^{15}NH_3$ production [48].

A relatively straightforward source of contamination are traces of NH_3 that may already be present in the system. This includes ammonia carried in the purging gas, adsorbed on glassware, dissolved in the electrolyte, or even released from the precursors used in catalyst synthesis. These sources can usually be detected by running the system under a purge, without applying any

potential, for a few hours. Izelaar et al. [49] measured these levels systematically and showed that NH_3 contamination are usually in the range of 1 to 6 nmol cm^{-2} for laboratory latex and nitrile gloves, Celgard membrane, carbon paper, Pt foil, and electrodeposited Cu on carbon paper. Compared to NH_3 amount usually measured in different studies, these ranges are not significant if the experiment is handled carefully, particularly when proper cleaning procedures are followed.

The more critical and difficult challenge is contamination from N-species such as NO_x species, which can be reduced to NH_3 much more easily than N_2, since these reactions are thermodynamically and kinetically more favorable [50]. This means that even trace amounts of N-species can be converted into NH_3 under applied potentials, leading to false positives. These amounts can be substantially higher than the aforementioned NH_3 contamination. For example, NO_3^- was measured at approximately 1500 nmol cm^{-2} on a Cu electrode electrodeposited onto carbon paper [49].

To minimize the N-species reduction problems, control and purification steps are essential. Gas lines should be equipped with traps to remove residual NH_3 and NO_x. Commercial scrubbers are available, but homemade systems using strong oxidizers such as $KMnO_4$ are also commonly applied to convert NO_x to soluble species and trap them before entering the electrochemical cell [50]. Still, even with gas purification, contamination can persist in the electrolyte or remain adsorbed on the catalyst surface.

When strict controls are followed, many catalysts that were once believed to be active for NRR have been shown to produce only false positives. Examples of these catalysts, showing no NRR activity include Mo_2N [48], Pt/C, and Pd/C [51], Au/C [51,52], Ru, and Rh [51,53], α-Mo_2C, θ-Fe_3C, and χ-Fe_5C_2 [54], Bi [52,55], CoMo thin films [56], VN, Nb_4N_5 [57], Pd nanosheets [58], and Re [53]. An overview of some of these papers can be seen in Table 1.1 Selected papers that reported false positives for NRR in aqueous solutions, highlighting the typical scales of NH_3 observed from contaminations, and summarizing potential contamination sources, the control experiments performed to identify false positives, and the origins of any misleading signals. Some of the selected studies shown in Table 1.1, are discussed.

Table 1.1 Selected papers that reported false positives for NRR in aqueous solutions

Catalyst	Electrolyte	Highest amount of measured NH_3	False positive detection method	Possible source of false signal	Ref
Mo_2N/Ti	0.1 M HCl	0.455 ppm in 6 ml (2.73 μg) after 1 hour	Isotope labeling with purified $^{15}N_2$: No $^{15}NH_3$ detected, but significant $^{14}NH_3$ observed (no Ar control performed beforehand).	From chemical decomposition of Mo_2N.	[48]
Pt, Pd, Ru, Rh and Au, all on C paper	0.1 M HCl	0.0025 ppm in 40 ml (0.1 μg) after 1 hour for Pt/C (highest detected NH_3 was on this metal)	Repeated testing on the same electrode.	N-species on the catalyst surface that convert to NH_3.	[51]
Fe_3C, Fe_2C, Mo_2C, all on C paper	0.1 M KOH	0.124 ppm in 20 ml (2.48 μg) after 2 hours	Almost same amounts of NH_3 recorded when purged by Ar and at OCP.	Reduction of NO_2^- in the electrochemical system.	[54]
Au/C and Bi/C	0.5 M K_2SO_4 having initial pH of 3.5	Below detection limit after 1 hour	Below detection limit for both N_2 and Ar.	N/A	[52]
CoMo on n-type Si	50 mM H_2SO_4	0.2 ppm in 20 ml (4.0 μg) after 20 minutes	Isotope-labeling experiments with purified $^{15}N_2$: No increase in $^{15}NH_4^+$, but substantial $^{14}NH_4^+$ increase consistently observed.	N-impurities incorporated in CoMo thin films during sputtering, even under Ar atmosphere	[56]
NbN and VN on Carbon paper	0.05 M H2SO4	≈ 1.7 ppm in 15 ml (25.5 μg) after 2 hours	Comparable NH_3 amounts when purged by Ar.	Reduction of N atoms of the catalyst.	[57]

Note: All reported NH_3 amounts in this table have been converted to μg and ppm to allow easier comparison between studies. For the exact values and detailed explanations of observed inactivity or false positives, please refer to the original publications.

Metal nitrides have studied as potential NRR catalysts, with reported NRR activity for systems such as VN nanoparticles [59], Mo_2N [60], TiN [61], CrN [62] and Cr_2N [63]. They are mainly appealing for NRR studies due to their proposed Mars–van Krevelen (MvK) mechanism [64], where it is proposed that the lattice nitrogen is electrochemically reduced to ammonia, and the

resulting vacancies are replaced by gaseous N_2. However, some recent studies using isotope-labeling and rigorous contamination controls have revealed a different picture. For Mo_2N, VN, and NbN, no NRR activity could be confirmed:

Hu et al. studied the NRR activity of Mo_2N coated on Ti and detected NH_3 after the test. However, isotope labeling control test with $^{15}N_2$ purged into the cell indicated no $^{15}NH_3$ formation. Instead, $^{14}NH_3$ was detected which was attributed to the chemical decomposition of Mo_2N under the applied potential [48]. Before realizing the NRR inactivity of Mo_2N, the researchers conducted linear sweep voltammetry (LSV) to indicated NRR activity. LSV is a common electrochemical technique in which the potential of the working electrode is swept linearly over time while the resulting current is recorded. In NRR studies, researchers often perform LSV both under Ar-saturated and N_2-saturated electrolytes, comparing the two curves to identify potential regions where N_2 reduction might occur. The idea is that any additional current under N_2, which is usually in the range of a few milliamperes, could indicate catalytic N_2 reduction. However, this approach can be misleading and may simply be measurement errors or side reactions like N-species reduction rather than genuine N_2 reduction [50]. For Mo_2N, the LSV curves under N_2 purging appeared more negative compared to those in Ar-saturated electrolyte. However, as discussed above, this shift was found not to reflect genuine NRR activity [48].

In the case of NbN and VN supported on carbon paper [57], the measured ammonia was essentially identical under N_2 and Ar, indicating that the detected product did not originate from electrochemical N_2 reduction. Instead, the source of NH_3 was traced to the reduction of lattice nitrogen atoms, released from the catalyst itself during operation. This observation is important because it directly demonstrates how materials with a high intrinsic nitrogen content can generate misleading signals that mimic NRR activity. Interestingly, the rate of NH_3 release was not constant but decreased over time before stabilizing after about six hours, consistent with gradual depletion of reducible nitrogen from the lattice.

Noble metals have been repeatedly reported to be active for NRR, as summarized in the review paper by Rao et al. [65]. However, their genuine NRR activity is challenged by Cai et al. [51]. They examined the NRR activity of some of the noble metals including Pt, Pd, Ru, Rh, and Au deposited on carbon paper. The measurements led to detectable NH_3 during NRR, but repeated measurements in the same conditions led to no detectable NH_3. It shows that NH_3 was sourced from N-species already on the surface of the electrodes before reaction, and not from N_2

reduction. They showed that the N-species were not easily removed from the electrode surface with simple washing or rinsing with water, but cyclic voltammetry was able to "clean" the electrodes, demonstrating the need for a rigorous pre-treatment of electrodes.

Keeping these pitfalls in mind, it is important to evaluate each reported study in NRR with caution.

1.4.4 Selection of Ag-Sn for NRR study

The volcano plot in Figure 1.3 clearly shows that none of the studied pure metals, even the noble ones, are efficient electrocatalysts for NRR. They all require much more negative potentials to initiate NRR, while HER proceeds far more easily on their surfaces. This limitation has pushed many researchers to search for materials with improved characteristics, especially those that can lower the limiting potential.

Among different approaches such as single-atom catalysis [66–68], electrolyte engineering [69], or doping [70,71], the alloying strategy has emerged as one of the most widely studied. A broad range of alloy systems have been investigated for NRR, from bimetallic alloys [72–74] to other types including carbides [75,76], nitrides [77] and sulfides of metals [78].

Previous theoretical studies have shown that certain transition metals (TMs), such as Mo, Fe, and Ti, are particularly effective at interacting with N_2 molecules through N–metal bonds [79]. This is attributed to the presence of both vacant and occupied d orbitals, which enable an "acceptance–donation" pathway for electron transfer that weakens the N_2 bonds. In this process, it is proposed that the vacant d orbitals of the metal can accept lone-pair electrons from N_2, while the occupied d orbitals can donate electrons into the π* antibonding orbitals of N_2 [80]. The main drawback of these transition metals, however, is their strong affinity for hydrogen, which tends to occupy the active sites and promote HER instead of NRR [81].

Interestingly, certain main-group metals were shown to establish similar electronic interactions with N_2, but with a noticeably lower affinity for hydrogen bonding [81]. It has been suggested that elements such as Ga and Bi possess both empty and filled orbitals that allow for an "acceptance–donation" mechanism. For example, Ga ($4s^2 4p^1$) undergoes sp^3 hybridization, leaving behind one vacant orbital and three singly occupied ones, while Bi with its 6p band can donate electrons into the π* antibonding orbital of N_2 [47]. Indeed, various main-group metals, including Ga, Bi, and Sn based materials, have been reported to show promising activity toward NRR, as summarized in the cited review paper [81].

Overall, main-group metals offer some advantages for NRR, including their reportedly inherently weaker tendency for HER and their unique electronic structures that reported to favor N_2 adsorption and activation. These characteristics make them attractive candidates for designing hybrid systems. In particular, combining transition metals with main-group elements provides an opportunity to exploit d–p orbital hybridization, creating a more favorable electronic environment for N_2 activation. This strategy has also been extended to the design of active electrocatalysts for NO_3^- and NO_2^- reduction to NH_3, where p–d orbital hybridization is believed to enhance activity by tuning the electronic structure and promoting the adsorption and transformation of key intermediates. Recently, this strategy was implemented by doping Sn (p orbitals) into an Ag (d orbitals) host, which resulted in the development of a highly active catalyst for NO_3^- reduction to NH_3, achieving a Faradaic efficiency of 95.5 ± 1.85% and an NH_3 yield rate of 482.3 ± 14.1 mg h^{-1} $mgcat^{-1}$ [82]. The broad applicability of the p–d orbital hybridization strategy is further highlighted by its success with other p-block metals, such as Bi and In, which, when incorporated into Ag, have shown remarkable performance for NH_3 production [82]. In another study, this approach has been explored for NRR itself, where alloying Cu (d orbitals) with Ga (p orbitals) was found to enhance activity by lowering the energy barrier for the hydrogenation of N_2 [83]. Inspired by the demonstrated benefits of p–d hybridization in both NO_3RR and NRR, we selected Ag and Sn as our system of interest. This choice was further motivated by the fact that the individual metals, in the form of Ag films [84], Ag nanosheets [43], Sn nanoparticles [85], and Sn dendrites [86], have each reported to show reasonable NRR activity in aqueous solutions.

The performance of Ag-Sn for NRR is explored in chapter 3, including detailed analyses of its activity, and the mechanistic understanding of its behavior. The objectives of this section were to synthesize Ag–Sn alloys, to reliably measure its NRR activity, and to understand the underlying reasons for its observed activity or inactivity. This approach allowed us to critically assess whether this alloying strategy, successful in other electrochemical reactions such as NO_3RR and CO_2RR, are effective in NRR electrocatalysis.

1.5 Indirect NRR

As mentioned earlier, a major source of error in NRR studies arises from the unintended reduction of NO_x species to NH_3, which is both thermodynamically and kinetically much easier on a wide range of materials [50]. This feature, however, can also be viewed as an opportunity. If the reduction of NO_x to NH_3 is inherently more favorable, then this pathway can be intentionally utilized for ammonia production. In an indirect or hybrid strategies, N_2 is first converted into reactive nitrogen intermediates such as NO_x by another process, and these intermediates are then electrochemically reduced to NH_3. The electrochemical part of this approach falls within the research area known as the electrochemical reduction of NO_x (NO_xRR). In the following section, we first address the fundamentals of NO_xRR and the electrocatalysts developed for this reaction. We then discuss a sonochemical method for producing NO_x directly from N_2, which can serve as the initial step in hybrid systems. These discussions provide a foundation for better understanding the concepts and results presented in Chapter 4 (sonoelectrochemical pathways for NH_3 production.)

1.5.1 NH_3 production by NO_x reduction

As can be seen in Figure 1.4 [50], the standard electrode potential (E^0) for NO_x reduction is much more positive than that for N_2, indicating a lower ΔG and a more thermodynamically favorable reaction.

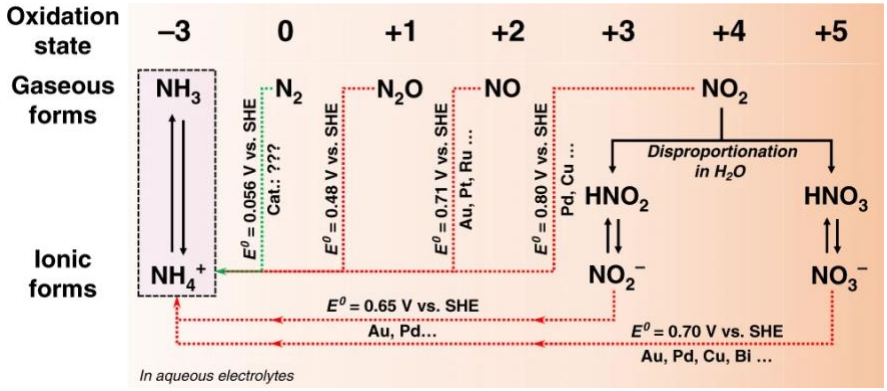


Figure 1.4 Electrochemical routes to NH_3/NH_4^+.

Pathways from N_2, gaseous NO_x, and ionic NO_x species, showing their standard redox potentials (vs. SHE) and examples of corresponding electrocatalysts for each pathway. Reprinted from reference [50].

NO_x reduction to ammonia is a valuable process, with applications such as converting NO_x contaminants from industrial and agricultural wastewater into NH_3 [87,88].

NO_xRR occurs at the cathode surface, where NO_x ions, such as nitrate (NO_3^-) and nitrite (NO_2^-) are reduced to ammonia. In NO_xRR studies, NO_x is typically provided by dissolving salts like KNO_3 and KNO_2 in concentrations as high as 1 M in a conductive electrolyte, such as a 1 M KOH solution [89]. This approach ensures a steady supply of NO_x^- ions, facilitating efficient electrochemical reduction. The accessibility of the cathode to these dissolved reactants is another factor contributing to the higher rates and FEs observed in NOxRR. In NRR, the solubility of N_2 in water is relatively low, approximately 20 mg/L (20 ppm) at 20°C under 1 atm pressure [90] which limits the availability of the reactant. In contrast, NO_x^- ions are readily available in the electrolyte in higher concentrations, enhancing the efficiency of the reduction process. Compared with NRR, NO_3RR can achieve ammonia yield rates several orders of magnitude higher, reaching high levels such as 263 mg $h^{-1}cm^{-2}$ [91], and Faradaic efficiencies reaching 100% [92]. The reduction of NO_3^- to NO_2^- is generally regarded as the limiting step in NO_xRR for NH_3 production. As a result, many studies concentrate primarily on NO_3RR, probably with the reasoning once a catalyst is developed that performs well for NO_3RR, it would also be effective for NO_2RR, since NO_2^- reduction is more favorable [93].

There has been a growing interest in NO_xRR, and this shift becomes clear when comparing its publication trend with that of NRR over recent years. A survey of Scopus data shows that NRR publications reached a peak in 2022, after which the growth slowed (Figure 1.5). This slowdown may reflect the repeated observation of very low ammonia yields and faradaic efficiencies, the emergence of reported false positives, and the discouraging experience of some researchers who observed negligible NRR activity in their own experiments. As a result, many groups might have redirected their focus toward NO_xRR, where higher activities and efficiencies can be achieved more readily. The publication rate for NO_xRR has now overtaken that of NRR.

It is important, however, to place these two fields in their proper context. While both ultimately target NH_3 as the product, their challenges and applications are fundamentally different. The continued study of NRR is essential for the development of truly sustainable NH_3 production routes from N_2 that can replace H-B process. NO_xRR is particularly attractive for environmental applications, such as wastewater remediation and nitrate/nitrite removal, where the simultaneous production of value-added NH_3 makes it more appealing. In this sense, NO_xRR should be viewed

as a complementary pathway: practically important and technologically promising, but not a replacement for the fundamental challenge represented by NRR.

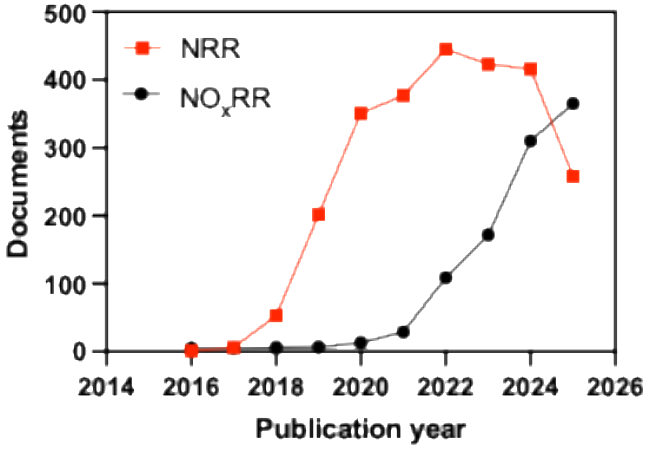


Figure 1.5 Publication trends for NRR and NO_xRR to NH_3.

The plot shows the annual number of publications retrieved from Scopus in August 2025, by searching for nitrogen reduction reaction (NRR) and various keywords of NO_3^- and NO_2^- reduction reactions (review articles excluded). These data are intended to illustrate general trends in the field; exact publication numbers should not be inferred from this figure.

1.5.2 NO_XRR Electrocatalysts

The choose of electrocatalysts used for NO_xRR is significant for the selectivity, activity, and stability of NO_xRR for NH_3 production, as the catalyst surface controls adsorption energies, reaction pathways, and competing HER [94]. Over the past years, a wide range of materials have been explored for NO_3RR to NH_3, including noble metals such as Ru [92], Ir [95], Pd [96], transition metals such as Cu [97], Co [98], Ni [94], and metal oxides [99,100].

Among the studied metals, Cu and Cu-based materials have demonstrated relatively higher activity and selectivity for converting nitrate to ammonia [101]. A polycrystalline copper loaded on self-supporting carbon fiber showed an ammonia yield of 101.4 μmol h^{-1} cm^{-2} and with a FE of 94 % at – 0.266 V vs. RHE [102]. In another study, amorphous Cu coated on carbon nanofibers demonstrated a yield rate of: 1.42 mol h^{-1} g^{-1} with an FE of 95.7% [103].

This distinctive performance of Cu can be rationalized by theoretical calculations, which provide insights into the competition between NO_3RR and HER on different metal surfaces (Figure 1.6) [104]. In these analyses, the parameter $U_L(NO_3RR) - U_L(H_2)$ reflects the relative preference of a catalyst for NO_3RR over hydrogen evolution, while $U_L(NO_3RR)$ itself represents the intrinsic

activity toward nitrate reduction. Catalysts that fall in the upper-right region of this plot are therefore considered the most promising, as they simultaneously exhibit high activity and high selectivity. Notably, Cu stands out in this regard: although it requires very negative potentials to activate N_2 for NRR (UL more negative than −2 V vs RHE), its onset potential for NO_3RR is significantly milder, around −0.23 V vs RHE. This highlights why Cu is particularly attractive for NO_3RR, as it combines accessible reaction energetics with a favorable balance between nitrate reduction and competing HER. Based on these specific characteristics, Cu was selected as the electrocatalyst for our second project, which is described in Chapter 4.

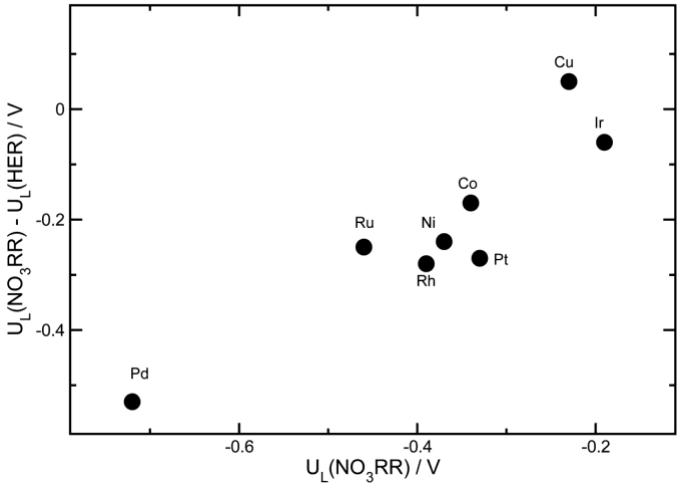


Figure 1.6 The difference between the limiting potentials for NO_3RR and HER, Reprinted from reference [104].

For indirect NRR, the NOxRR first requires the conversion of N_2 into NOx species. These processes will be discussed in the following subchapter.

1.5.3 Ultrasound-assisted N_2 breaking

Ultrasound consists of sound waves with frequencies above the audible range (typically >20 kHz) and is widely used in cleaning, sonar, and chemical processes. When a liquid is exposed to these high-energy waves, repeated compression and rarefaction events occur, causing bubbles to form and oscillate within the medium [88]. These cavitation bubbles can collapse violently, generating extremely high pressures and local temperatures, sometimes exceeding 5000 K, and creating conditions capable of driving demanding chemical reactions, such as the oxidation of N_2 [87]. While the possibility of breaking N_2 bonding to produce NO_x species has been shown in different studies [105], with the first one going back to 1936 [106], the exact mechanism for this conversion is not understood well.

The possibility of directly activating N_2 by cavitation has been debated. As mentioned before, molecular nitrogen is highly stable and requires a large amount of energy to break its triple bond, even higher than the energy released by cavitation, making its direct activation challenging [107]. In fact, earlier studies have shown that molecular oxygen is generally necessary for N_2 activation and the subsequent formation of NO_x species [105]. During acoustic cavitation, homolytic cleavage of H_2O and O_2 molecules can happen. This produces reactive oxygen species (ROS), including OH• and O_2• radicals, which then interact with molecular nitrogen to generate NO_x^- [108].

Different amounts of NO_x have been reported following sonication of N_2-containing gases (e.g. pure N_2 or air). These amounts depend strongly on the sonicator's characteristics such as power, and frequency, and also on the volume of water, and on the type of gas dissolved or purged through the solution. Reported values vary from as little as 0.06 µM NO_x when using a 35 kHz sonicator for 650 mL of water, with N_2 purged into the solution, to 0.35 µM under identical conditions but with air purging instead of N_2 [109]. In more extreme setups, with mixtures of N_2 and O_2 and higher frequency (900 kHz) in a smaller volume of water (~100 mL), NO_x generation rates reach ~7.8 µM per minute [110], which over 60 min corresponds to around 797 µg of NO_x.

Interestingly, adding an inert noble gas such as argon also enhances NO_x production compared with N_2 alone. As can be seen in Figure 1.7, in experiments with 28 kHz sonication, the NO_2^- + NO_3^- concentration reached from below 5 µM for N_2 to ~15 µM after 90 minutes in an N_2 + Ar environment [111]. The authors of this paper proposed that the presence of Ar leads to the occurrence of more violent cavitation collapse events. This was attributed to the low thermal conductivity of Ar that allow bubbles to reach higher temperatures, and creating energetic collapse conditions, forming more oxidative radicals for N_2 oxidation.

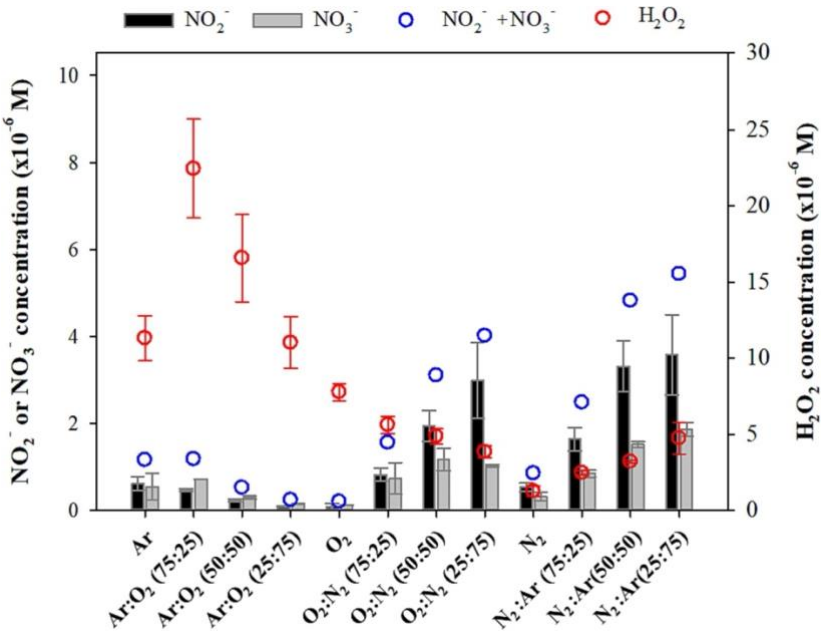


Figure 1.7 Concentrations of NO_2^-, NO_3^-, and H_2O_2 generated sonochemically. Under saturation/closed conditions with Ar, O_2, and N_2 at 28 kHz after 90 min of irradiation. Reprinted from reference [111].

The ultrasound-assisted conversion of N_2 to NO_x has demonstrated a promising pathway for generating reactive nitrogen intermediates. However, the efficiency of this approach can be further improved by integrating it with contact-electro-catalysis, a strategy that enables direct electron transfer at the solid–liquid interface to accelerate reaction kinetics. In the following section, we introduce how contact-electrocatalysis can complement sonochemical processes and potentially offer a more effective route for N_2 activation and NOx production.

1.5.4 Contact-electro-catalysis

The concept of contact-electro-catalysis (CEC) was first introduced by Wang et al. in 2022 [112]. It builds on the phenomenon of contact electrification, where dielectric materials such as polytetrafluoroethylene (PTFE), fluorinated ethylene propylene (FEP), and polyvinylidene fluoride (PVDF) can transfer electrons during the repeated process of contact and separation at the solid–liquid interface. In this framework, the transferred electrons can also participate in subsequent chemical reactions. Efforts have since been devoted to understanding and applying this principle, particularly because electrons can generate some reactive oxygen species (ROS) such as OH• and H• radicals [113], which can themselves take part in chemical reactions. In this way, contact-electro-catalysis effectively acts as a new catalytic pathway for driving chemical transformations.

Although the effect of CEC for ROS generation is widely accepted, the exact mechanism is still under debate. This uncertainty partly comes from the fact that sonochemical mechanisms themselves are not completely understood, and the addition of contact-electro-catalysis makes the picture even more complex. One of the latest suggestions is that not all contact-electrons can take part in the chemical reactions to produce ROS. In fact, only a very small portion (less than 0.1%) of the electrons is proposed to have enough energy to initiate radical formation reactions, while cavitation in ultrasound is proposed to "activate" these electrons (Figure 1.8) [114]. However, no clear definition is provided for what exactly counts an "activated" electron, nor is it fully explained how cavitation transfers its energy to them.

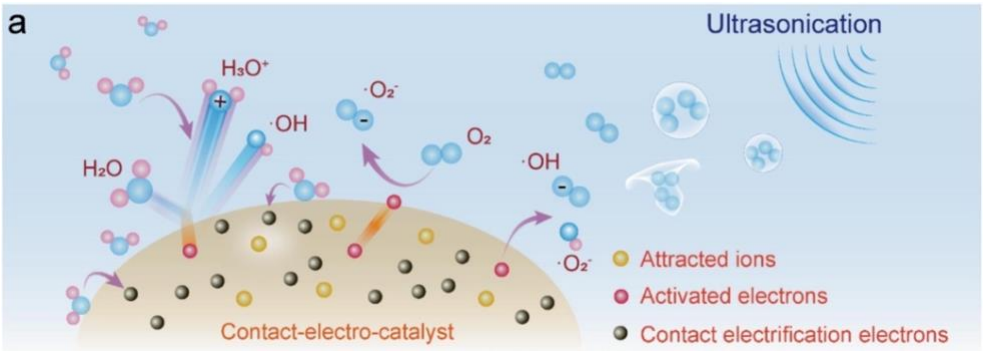


Figure 1.8 A proposed mechanism of contact-electro-catalysis during ultrasonication.

Reprinted with permission from reference [114]. Copyright (2025), Elsevier.

In another study, DFT calculations showed that the high pressure formed by bubbles cavitation, can increase the energy gap for electron transfer between PTFE with H_2O and O_2 to generate ROS by around 17%, but this change is not particularly large, and more importantly, the role of the high temperatures generated during cavitation events was not taken into account [112]. To reduce this mechanistic complexity of sonication, CEC was also explored using ball milling [112]. It was shown that a critical milling speed is required to weaken the O_2 antibonding and promote electron transfer from the PTFE electron donor to generate ROS. The authors examined the partial density of states (PDOS) of O_2 as the electron acceptor in a coexistence model at different PTFE–O_2 distances to illustrate this effect. At higher milling speeds, the stronger impact energy was assumed to bring PTFE chains and O_2 molecules closer, reducing the separation distance. This distance dependent effect was confirmed by molecular orbital configurations, which showed that electron transfer occurs from PTFE into the π* antibonding orbital of O_2 to form superoxide radicals. The calculated energy barrier for this transition dropped from 3.88 eV to 2.54 eV as the

distance decreased, indicating that higher-energy mechanical inputs can directly lower the threshold for ROS generation.

Overall, a higher degree of cavitation generally translates into stronger contact-electro-catalysis. This can be attributed to several factors acting simultaneously: more intense contact-electrification events, a greater number of electrons accumulated on the catalyst surface, and an increased ability to overcome the energy barriers required for O_2 and H_2O electron transfers to PTFE.

In a practical point of view, contact-electro-catalysis has recently been explored in various fields, such as water pollutant degradation [115], electrochemical H_2O_2 generation [113], metal recovery from electronic wastewater [116], and the oxidation of methane (CH_4) to value-added chemicals like formaldehyde (HCHO) and methanol (CH_3OH) [117].

In a recent study, PTFE was employed as a contact-electro-catalyst in an ultrasonic bath for ammonia (NH_3) synthesis, with nitrogen reduction reaction [118]. NH_3 formation occurred entirely through the contact-electro-catalytic effect of PTFE activated by ultrasonic agitation, without applying an external electrochemical potential. The proposed mechanism involves OH• and H• radical generation through contact electrification. OH• radicals subsequently combine to form H_2O_2, while H• radicals react with N_2 to yield NH_3. Although this mechanism is supported by experimentally measured OH• and H• radicals when the system is purged by N_2, it does not explain why NH_3 is produced when the system is purged by N_2:O_2 at 8:2 ratio, where signals of OH• and $O2•^-$ was observed but no signal was detected for H•. The NH_3 yield in this setup was limited, likely due to side reactions**,** particularly the competitive oxidation of N_2 into NO_x species.

A more recent study have shown that OH• radicals produced by PTFE can facilitate the formation of nitric acid and other nitrogen oxides under similar sonochemical conditions, with N_2 and O_2 in the system (Figure 1.9) [119].

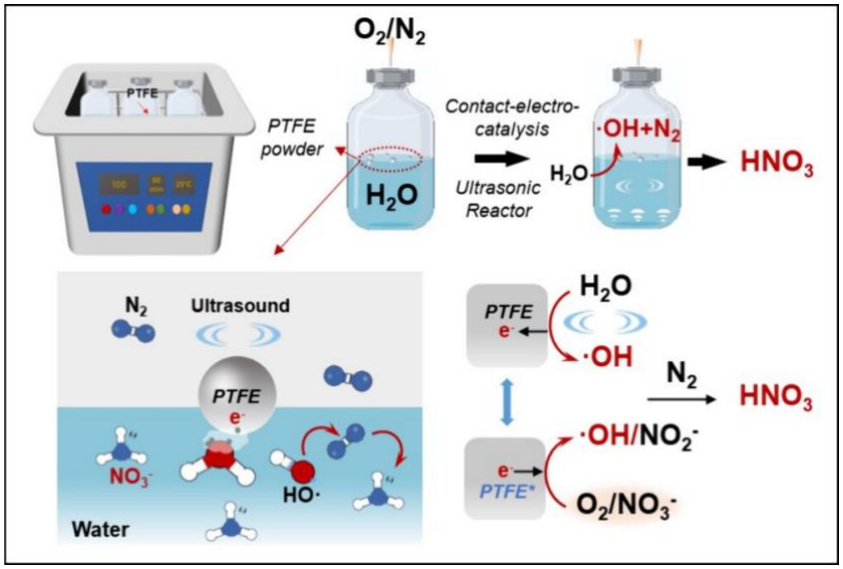


Figure 1.9 Experimental setup schematic for HNO_3 synthesis.

Via PTFE-assisted contact-electro-catalysis. The proposed reactions with OH• can also be seen. Reprinted with permission from reference [119]. Copyright (2025), American Chemical Society.

The simultaneous formation of NO_x and NH_3 on PTFE demonstrates that contact-electro-catalysis can create both oxidative and reductive microenvironments for reactions. This dual reactivity highlights the potential of strategically coupling CEC with complementary catalytic processes, such as electrocatalysis, to achieve more precise control over reaction pathways and selectively target desired products. To date, and to the best of our knowledge, such a deliberate coupling strategy has not been explored for NH_3 synthesis, nor for other applications where employing both oxidative and reductive conditions could provide advantages. This approach has been explored in chapter 4.

1.6 Thesis objectives and structure

The structure of this thesis is built around two complementary approaches to green ammonia production, designed to explore both the potential and limitations of current strategies and propose new directions for efficient N_2-to-NH_3 conversion. The first approach focuses on the alloying strategy, one of the most explored methods in this field. The second approach explored a hybrid system that combines electrochemical NRR with ultrasound-assisted N_2 activation. Together, these two approaches are connected by a unified goal: first, to demonstrate whether the studied alloying strategy works for NRR, and second, to propose and validate a new hybrid methodology for N_2 activation and ammonia production.

The thesis is structured as follows:

Chapter 1 provides a comprehensive introduction and literature review. It begins by highlighting the urgency of replacing fossil fuels and the significance of carbon-free ammonia production. The literature review is presented in two main sections that reflect the thesis objectives. The first section addresses the challenges of direct NRR, including the competing HER, false positives in NRR research and reviews the alloying strategy and showing the rationale for selecting Ag–Sn alloy for study. The second section, starting from section 1.5, is focused on in-direct NRR, and reviews the strategies for pre-activating N_2 to enhance ammonia production. This includes a review of Li-mediated NRR, plasma-assisted NRR, NO_x reduction to NH_3, and methods such as ultrasound and contact-electro-catalysts, which inspired the hybrid approach developed in this work.

Chapter 2 describes the experimental methodologies employed in both research directions, detailing synthesis procedures, electrochemical setups, characterization techniques, and reaction conditions.

Chapter 3 presents the first article, named "Exploring Ag_3Sn Alloy for Nitrogen Electroreduction to Ammonia" which investigates the performance of Ag_3Sn for NRR, including detailed analyses of its activity, selectivity, and the mechanistic understanding of its behavior. Ag_3Sn was selected for investigation due to its high reported potential for the nitrogen reduction reaction (NRR). The objectives of this section were to synthesize Ag–Sn alloys, to reliably measure the NRR activity of Ag_3Sn, and to understand the underlying reasons for its observed activity or inactivity. This approach allowed us to critically assess whether this alloying strategy, successful in other electrochemical reactions such as NO_3RR and CO_2RR, are effective in NRR electrocatalysis.

Chapter 4 presents the second article, named "Breaking the nitrogen triple bond: a sonoelectrochemical pathway to ammonia synthesis boosted by contact-electro-catalysis" focused on the sonoelectrochemical NRR system coupled with PTFE, exploring how ultrasound-assisted activation and contact-electro-catalysis influence reaction rates and ammonia yields. Here, the objectives were to investigate the feasibility of sonoelectrochemical NRR, and to examine whether the reaction rate can be enhanced through the addition of contact-electro-catalysts such as PTFE, and to understand the influence of key parameters, including the purging gas composition and PTFE loading, on system performance.

Finally, Chapter 5 summarizes the main findings of the thesis, discusses their implications, and outlines potential directions for future research in green ammonia electrosynthesis.

2 EXPERIMENTAL

Figure 2.1 illustrates an overview on the experiments performed in thesis.

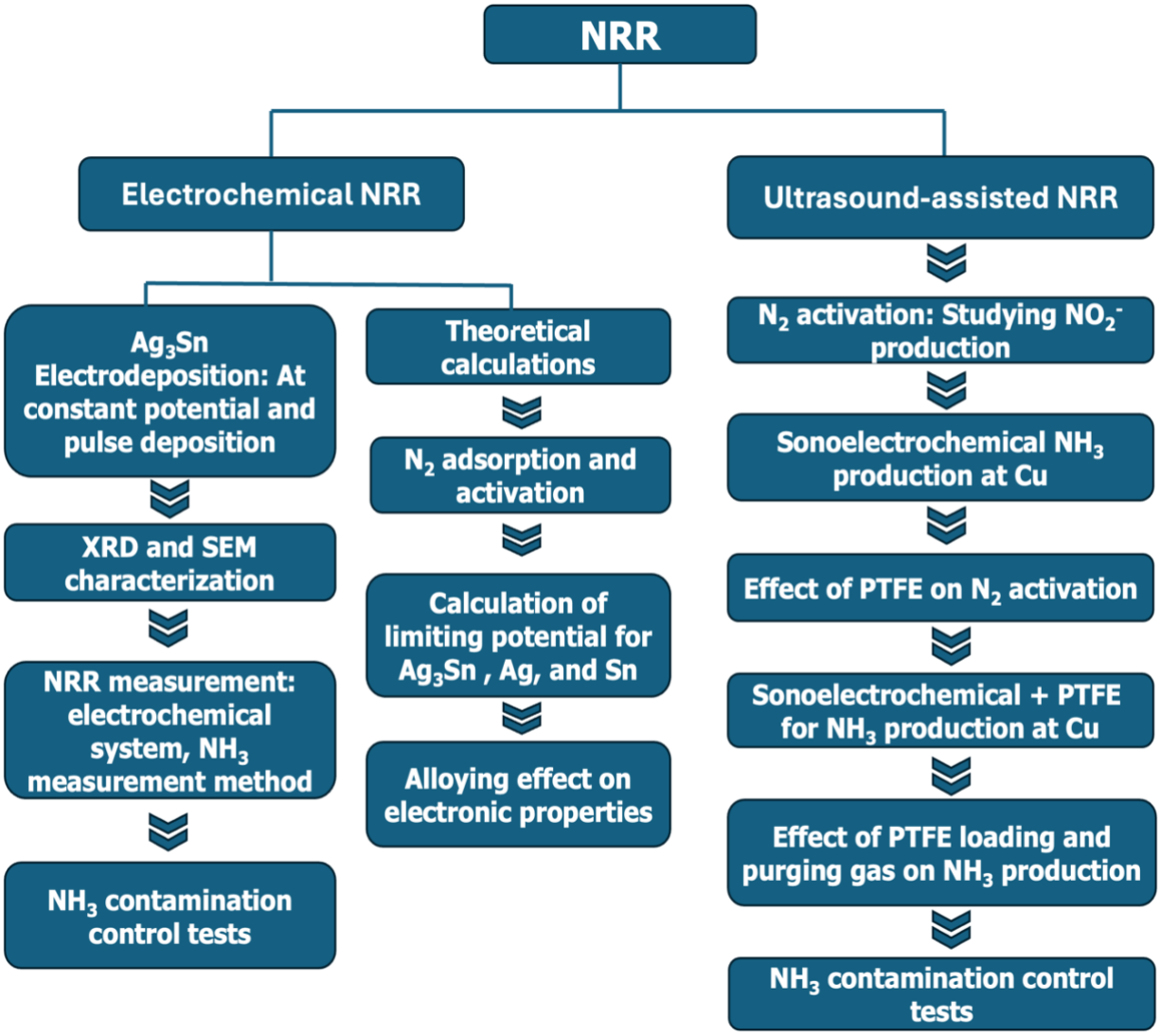


Figure 2.1 Methodological flowchart summarizing the experiments performed.

The experimental details will first explain the methodology of the Ag_3Sn project, and then those of the ultrasound-assisted NRR at Cu.

2.1 Exploring Ag_3Sn for electrochemical NRR

2.1.1 Carbon cloth activation

Carbon cloth was selected as the substrate for electrodeposition of Ag_3Sn. This material can support a relatively high loading of deposited catalyst while remaining inactive toward NRR [120], which minimizes interference from the substrate itself. A challenge, however, arises from the inherently hydrophobic nature of carbon cloth, which makes it difficult to achieve a smooth and homogeneous electrodeposition layer. To address this, the carbon cloth was electrochemically activated before Ag_3Sn deposition.

Electrochemical activation is reported to introduce oxygen-containing functional groups (such as –OH, –COOH, and C=O) onto the carbon surface [121], that can increase surface hydrophilicity, which in turn improving electrolyte wetting and facilitating uniform nucleation during subsequent electrodeposition. In our case, activation of the carbon cloth promoted uniform Ag_3Sn deposition across the substrate, avoiding the clustered growth and detachment of the deposit.

For the activation step, the carbon cloth substrate was first cut into 2 × 1 cm^2 pieces, giving a total accessible surface area of 4 cm^2 when both sides were considered for Ag_3Sn deposition. Prior to electrochemical treatment, the pieces were rinsed thoroughly with deionized water, followed by degreasing in acetone using ultrasonication for 10 minutes.

Electrochemical activation was then performed in a three-electrode configuration. The carbon cloth served as the working electrode (anode), Ag/AgCl was used as the reference electrode, and a platinum mesh acted as the counter electrode (cathode). The electrolyte was 2 M H_2SO_4, and a constant current density of 60 mA cm^{-2} was applied for 10 minutes. Under these anodic conditions, oxygen-containing surface groups are introduced onto the carbon surface, which improves hydrophilicity. After activation, the carbon cloth was removed from the cell, rinsed several times with deionized water to eliminate any residual acid, and finally dried in air before being used for Ag_3Sn electrodeposition.

2.1.2 Ag_3Sn electrodeposition

Electrodeposition was selected as the synthesis method because it requires relatively simple facilities and provides a good flexibility in controlling the alloy composition and morphology [122]. The activated carbon cloth (ACC) was then used as the substrate for Ag_3Sn electrodeposition. To prepare the electrodeposition bath, 0.2 M thiourea [$SC(NH_2)_2$], 0.025 M $SnSO_4$, and 0.01 M

Ag_2SO_4 were dissolved in 50 mL of 2 M H_2SO_4 solution. The electrolyte was prepared following the procedure of reference [123]. A three-electrode cell was employed, in which the ACC was placed as the working electrode, Ag/AgCl was used as the reference, and a platinum mesh served as the counter electrode.

Initially, Ag_3Sn was electrodeposited on non-activated carbon cloth at a constant potential of –0.65 V vs. Ag/AgCl. SEM analysis showed poor coverage and weak adhesion of the Ag–Sn alloy. When the same potential was applied to activated carbon cloth, the deposited amount increased, but the coverage was still not satisfactory. To address this, pulse electrodeposition was employed. This technique is known to provide improved control over nucleation and growth compared to direct current deposition [124], thereby enhancing coverage and adhesion.

Pulse electrodeposition was first tested with on/off ratios of 2:1, 1:1, and 1:2. Among these, the 2:1 ratio resulted in the highest catalyst loading. Based on this outcome, a range of pulse times was studied, specifically 2 s/1 s, 1 s/0.5 s, 0.5 s/0.25 s, 0.25 s/0.125 s, 0.005 s/0.0025 s, and 0.0025 s/0.0012 s (on/off). In all cases, the applied potential during the pulse "on" period was –0.65 V vs. Ag/AgCl, and the total electrodeposition time was fixed at 3 hours. After deposition, the samples were rinsed thoroughly with deionized water and dried in air. The Ag_3Sn catalyst deposited on activated carbon cloth is hereafter referred to as Ag_3Sn/ACC.

2.1.3 Physicochemical characterization

The deposition of the coating on the activated carbon cloth surface was examined using scanning electron microscopy (SEM, TESCAN VEGA3). SEM allowed us to study the surface morphology at different magnifications and to evaluate how the coating spread over the fibrous structure of the ACC. Energy-dispersive X-ray spectroscopy (EDS) was used to determine the elemental composition of the samples, which helped confirm the presence of the deposited elements and assess their distribution across the surface. Finally, X-ray diffraction (XRD, PANalytical X'Pert Pro) was carried out to investigate the crystallographic structure of the synthesized coating. This technique provided insights into the degree of crystallinity and possible phase formation resulting from the deposition process.

2.1.4 Electrochemical measurements

For the electrochemical measurements, a two-compartment H-type cell was used. The two chambers were separated by a Nafion membrane. A platinum mesh was used as the anode, while the cathode was the Ag_3Sn deposited on activated carbon cloth (Ag_3Sn/ACC). A Hg/HgO electrode was used as the reference electrode, and all potentials reported in this work are given against the reversible hydrogen electrode (RHE).

Before each experiment, the Nafion membrane (2 × 2 cm^2) was cleaned and activated. This was done in three steps: first, boiling it for one hour in Milli-Q water containing 3% H_2O_2; second, boiling it again for one hour in 1.2 M H_2SO_4; and finally, boiling in fresh Milli-Q water for one more hour to remove the remaining acid. The membrane was then kept in Milli-Q water until use.

Two different electrolytes were prepared for the experiments: a neutral electrolyte consisting of 30 ml of 0.5 M K_2SO_4 (pH ≈ 7), and a basic electrolyte consisting of 30 ml of 2 M KOH (pH ≈ 13.5). These electrolytes were used to study the NRR activity in aqueous media.

To make sure that the introduced N_2 gas was free from contamination, especially ammonia and NO_x, it was passed through a purification system before entering the electrochemical cell. First, N_2 was bubbled through 500 ml of 1 M H_2SO_4 to trap any NH_3 present. Then, it was passed through 10 ml of a solution containing 1 M $KMnO_4$ + 1 M KOH to remove NO_x species. As a last step before the gas entered the cell, it was bubbled through 10 ml of the same electrolyte used in the cell. After the electrochemical cell, an additional trap containing 5 ml of 0.1 M H_2SO_4 solution was used to collect any NH_3 that might escape from the cell with the outlet gas.

Before applying any potential, the whole system was purged with N_2 for one hour to ensure complete saturation of the electrolyte. The electrochemical tests were then carried out by applying constant potentials of -0.2, -0.4, -0.6, -0.8, and -1 V vs. RHE for 18 hours, while maintaining an N_2 flow of 20 ml min^{-1} through the traps and into the cell. After each experiment, the produced NH_3 was quantified as described later.

Control tests were also performed to verify the true source of the detected NH_3. Three types of controls were used: (i) operating the system with the same electrode and gas flow but without applying any potential, while purging with either N_2 or Ar for 18 hours, (ii) applying the same constant potentials but replacing N_2 with Ar (Air Liquide, 99.999%), and (iii) replacing the Ag_3Sn/ACC electrode with a bare activated carbon cloth (ACC) electrode. The electrolysis tests

were intentionally performed for long durations (18 h) to increase the NH_3 concentration in the electrolyte, which makes its detection and quantification more reliable.

2.1.5 Ammonia measurement

The amount of NH_3 produced during the electrochemical tests was determined using two different methods depending on the electrolyte.

For experiments performed in 2 M KOH, the indophenol blue method was used following the procedure in [125]. After the NRR test, 10 ml of the electrolyte was extracted. To this, 0.4 ml of a solution containing 1 g of phenol dissolved in 10 ml of ethanol was added. Then, 1 ml of a solution containing 0.1 g of sodium hydroxide, 2 ml of sodium hypochlorite, and 2 g of sodium citrate dihydrate in 10 ml of water was added. Finally, 0.4 ml of 0.5 wt% $C_5FeN_6Na_2O$ solution was added. The addition of these reagents caused the solution to turn greener in samples with higher NH_4^+ concentrations. The mixture was then kept in the dark for 2 hours to allow full color development. The absorbance of the resulting solution was measured at 655 nm using a UV-Vis spectrophotometer (Agilent Cary 60).

For measurements in the 0.1 M H_2SO_4 trap and in 0.5 M K_2SO_4 electrolyte, the salicylate method was applied following reference [126]. In this method, 2 ml of the electrolyte was mixed with 2 ml of 1 M NaOH solution containing 5 wt% salicylic acid and 5 wt% sodium citrate. Then, 1 ml of 0.05 M NaClO and 0.2 ml of 1 wt% $C_5FeN_6Na_2O$ were added. The mixture was stored in a vial in the dark for 2 hours, after which the absorbance was recorded at 655 nm.

To quantify NH_3, calibration curves were prepared using 0.5, 1, 2, and 3 ppm NH_4Cl solutions in the corresponding electrolyte. Their absorbance was measured at 655 nm, and a linear relationship between absorbance and concentration was established. The NH_3 concentration in the unknown samples was then determined using this calibration curve.

2.1.6 Theoretical calculations

The theoretical calculations were performed by the collaborating team at Concordia University, and the details of the methods are provided in section 3.5.7 of this thesis.

2.2 Ultrasound-assisted NRR

2.2.1 Sonoelectrochemcial system

The electrochemical cell was positioned in a conventional ultrasonic bath (Branson 1800, 70 W, 40 kHz), using a custom-made holder to keep it fixed during the experiments. The system was continuously purged with different gases at a flow rate of 20 mL min^{-1}. Before entering the electrochemical cell, the gases were purified by passing through a sequence of traps designed to remove possible contaminants. The first trap contained 500 mL of 1 M H_2SO_4, which eliminated traces of NH_3. This was followed by a smaller trap (30 mL) containing 1 M $KMnO_4$ and 1 M KOH, intended to capture NO_x species. The final trap, positioned just before the gas entered the electrochemical cell, was filled with 20 mL of 0.5 M Na_2SO_4 solution. Each gas was purged into the system for 30 minutes prior to the start of the experiments to ensure a stable environment.

The electrolyte consisted of 30 mL of 0.5 M Na_2SO_4, in which different concentrations of PTFE were dispersed for comparison. The electrochemical setup used a single-compartment cell based on a 100 mL beaker containing the electrolyte. A 1 × 1 cm^2 copper foil served as the cathode (placed on both sides of the cell), and a 2 × 2 cm^2 platinum mesh was used as the anode. The copper cathode was prepared before each experiment by mechanical polishing, followed by ultrasonic cleaning in acetone for 10 minutes to ensure a reproducible clean surface. During the experiments, the applied current density at the copper cathode was fixed at −10 mA cm^{-2}.

A series of conditions were investigated to study the influence of different parameters. These included the PTFE content in the electrolyte (0, 10, 20, 60, 100, and 200 mg), the presence or absence of ultrasonic treatment, and the type of purging gas. The gas atmospheres tested were pure N_2, pure Ar, pure air, and two mixtures: 50:50 N_2 + Ar and 50:50 air + Ar. Each experiment was conducted for one hour under controlled conditions.

2.2.2 NH_3 and NO_2^- measurement

NH_3 was measured by the salicylate method that is explained in section 2.1.5. A calibration curve for NH_4^+ quantification was prepared using NH_4Cl standard solutions with concentrations of 0.5, 1, 2, 3, and 7 µg mL^{-1}. All standards were made in 0.5 M Na_2SO_4 to ensure consistency with the experimental electrolyte.

For the quantification of NO_2^-, a commercially available nitrite test kit was used. After each electrolysis experiment, 35 mg of the provided reagent was added to 3 mL of the electrolyte

sample. The mixture was then kept in the dark for 10 minutes to allow full development of the characteristic color before measurement [53]. A calibration curve was generated in parallel by preparing KNO_2 solutions with concentrations of 0.05, 0.5, and 1 µg mL^{-1} in 0.5 M Na_2SO_4, followed by UV-Vis absorbance measurements at 540 nm.

When analyzing electrolytes that contained PTFE, additional dilution steps were required to avoid interference from suspended particles. In these cases, each sample was diluted sevenfold with 0.5 M Na_2SO_4 before measurement, ensuring reproducibility across different PTFE concentrations.

3 Ag_3Sn ALLOY FOR NITROGEN ELECTROREDUCTION

Ag_3Sn alloy for nitrogen electroreduction: false positives and theoretical bases of inactivity

Alliage Ag_3Sn pour l'électroréduction de l'azote : faux positifs et bases théoriques de l'inactivité

Authors:

Arash Toghraei[+],[a] Mehdi Shamekhi[+],[b,c] Gilles H. Peslherbe,[b,c,d,e] and Daniel Guay*[a]

[a] Énergie, Matériaux et Télécommunications, Institut National de la Recherche Scientifique (INRS), Varennes, QC J3X 1P7, Canada

[b] Department of Physics, Concordia University, Montreal, QC H4B 1R6, Canada

[c] Center for Research in Molecular Modeling, Concordia University, Montreal, QC H4B 1R6, Canada

[d] Department of Chemistry and Biochemistry, Concordia University, Montreal, QC H4B 1R6, Canada

[e] Prof. G. H. Peslherbe, Department of Chemical and Materials Engineering, Concordia University, Montreal, QC H4B 1R6, Canada

[+] These authors contributed equally to this work.

Contribution of authors:

Arash Toghraei carried out the experimental work, including sample synthesis, characterization by SEM and XRD, and electrochemical testing, and wrote the corresponding section of the manuscript. Mehdi Shamekhi performed the theoretical studies, including DFT calculations, and drafted the theoretical section. Prof. Daniel Guay and Prof. Gilles H. Peslherbe supervised the project, with Prof. Guay focusing primarily on the experimental aspects and Prof. Peslherbe on the theoretical aspects. All authors contributed to the editing and revision of the manuscript.

3.1 Abstract

The electrochemical nitrogen reduction reaction (NRR) has emerged as a promising route for the production of green ammonia (NH_3). In many studies, alloying strategies have been employed to

enhance the performance of electrocatalysts in this process. This study assesses the NRR activity of a silver-tin (Ag-Sn) alloy, a mixture of metals, each of which has been previously reported for its high selectivity toward the NRR. Extended control experiments revealed that the detected NH_3 stemmed from contamination rather than catalytic activity. Complementary density functional theory calculations demonstrated that, despite a lower theoretical onset potential for Ag_3Sn (compared to pure Ag and Sn), the required overpotentials remained prohibitively high. These results underscore the importance of rigorous, long-duration controls and baseline contamination assessments to avoid misattributing the production of NH_3 to N_2 reduction.

3.2 Introduction

Ammonia (NH_3) is a key component of industrial fertilizers and has been estimated to sustain the livelihoods of about half of the world's population [127]. However, the industrial production of NH_3 *via* the Haber-Bosch process releases about 1.4% of the total world CO_2 emissions each year [128]. A sustainable method to produce carbon-free (green) NH_3 would not only eliminate these CO_2 emissions but also enable its use as a clean energy carrier, with NH_3 regarded as the fuel of the future [16]. A promising method is the electrochemical nitrogen reduction reaction (NRR), which allows the direct conversion of N_2 to NH_3 in an electrochemical cell, where N_2 reacts with solvated protons and electrons that are driven to the surface of the cathode *via* a power source. However, despite years of research, this method remains at low technology maturity levels (TRLs), typically 1-3 [129]. This is mainly due to the strong N≡N triple bond and weak activation of N2 at the surface of any known electrocatalysts. At the negative potentials required for NRR, the competing hydrogen evolution reaction (HER) is usually dominant, and most of the protons/electrons combine to produce H_2 rather than NH_3, resulting in low selectivity for the NRR [50].

In recent years, several metal and non-metal based electrocatalysts have been reported as active for the NRR [130,131]. However, NH_3 yields have remained low, typically in the range of parts per million (ppm). These low yields make the results highly susceptible to measurement errors and contamination. Recently, protocols have been suggested to minimize the effects of false positives [50,53]. Following these protocols that emphasize rigorous control tests, no NRR activity was reported for Mo_2N [48], Pt/C and Pd/C [51], Au/C [51,52], Ru and Rh [51,53], α-Mo_2C, θ-Fe_3C, and χ-Fe_5C_2 [54], Bi [52,55], CoMo thin films [56], VN, Nb_4N_5 [57], Pd nanosheets [58],

and Re [53]. In many cases, contamination of the purging gas and/or the reduction of N species other than N_2 was identified as the major source of error.

Keeping these false-positive pitfalls in mind, we aimed to synthesize a potentially active alloy and investigate its activity toward NRR by running different control tests. We selected the alloy by mixing metals that exhibit low hydrogen adsorption in an effort to minimize the HER. Another key criterion was combining a d-band metal with a p-orbital metal to benefit from p–d orbital hybridization. This strategy has been applied to develop active electrocatalysts for NO_3^- and NO_2^- reduction to NH_3, as p–d orbital hybridization is proposed to enhance activity by modulating the electronic structure and facilitating intermediate reaction steps [82,132]. Recently, this approach has been applied in the search for more active materials for the NRR, where alloying Cu (d orbital) with Ga (p orbital) showed an enhanced activity by decreasing the reaction energy barrier for hydrogenation of N_2 [83].

In the present study, Ag and Sn were chosen based on these criteria, and because the pure metals, in the form of Ag film [84], Ag nanosheets [43], Sn nanoparticles [85] and Sn dendrites [86], were reported to show reasonable NRR activity in aqueous solutions. However, it should be noted that these studies did not strictly follow the rigorous protocols described above and might have reported false positive results. This work combines experimental electrochemical tests and computational density functional theory (DFT) analysis to investigate the NRR activity of Ag_3Sn supported on activated carbon cloth (ACC) in basic and neutral electrolytes.

3.3 Results and discussion

3.3.1 Ag_3Sn electrodeposition

An Ag_3Sn alloy was electrodeposited onto the surface of carbon cloth, which was selected as the substrate due to its documented inactivity for NRR [120]. It was hypothesized that the porosity of the carbon cloth substrate would enable the deposition of high loadings of Ag_3Sn, thereby providing a large active surface area for NRR. Figure 3.1 shows a piece of the carbon cloth substrate and a schematic of the electrodeposition setup.

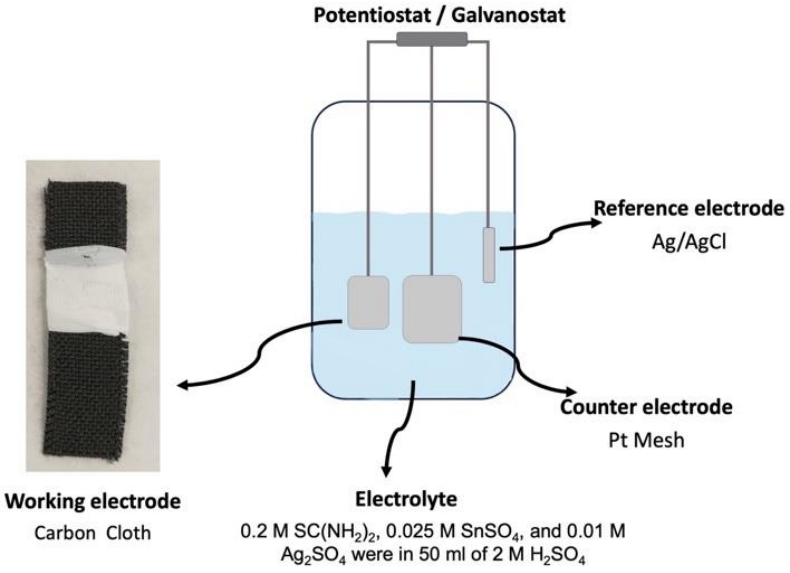


Figure 3.1 Schematic of the electrodeposition bath.

And optical image of the carbon cloth used as substrate.

The electrodeposition bath was prepared by dissolving 0.2 M $SC(NH_2)_2$, 0.025 M $SnSO_4$, and 0.01 M Ag_2SO_4 in 50 mL of 2 M H_2SO_4, following the method described by Wang *et al.* [123]. We observed that the deposit started to detach from the substrate after only 30 s of electrodeposition at a constant potential of -0.65 V *vs.* Ag/AgCl. The scanning electron microscope (SEM) images in Figure 3.2 clearly show poor coverage of the carbon cloth substrate by the deposit. This phenomenon can be attributed to the hydrophobic nature of the carbon cloth, which prevents uniform metallic deposition on its surface.

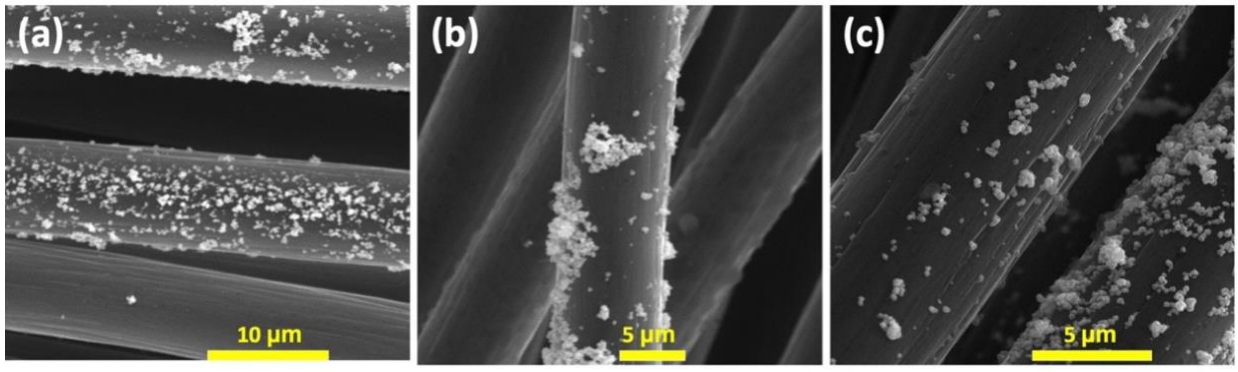


Figure 3.2 Scanning electron microscope (SEM) images at different magnification.

For Ag-Sn electrodeposited at -0.65 V vs. Ag/AgCl for 30 seconds on non-activated carbon cloth.

To circumvent this limitation, the carbon cloth was electrochemically activated in a 2 M H_2SO_4 solution before electrodeposition, which increased the hydrophilicity of the substrate (as shown in Figure 3.3, and the SEM in Figure 3.4).

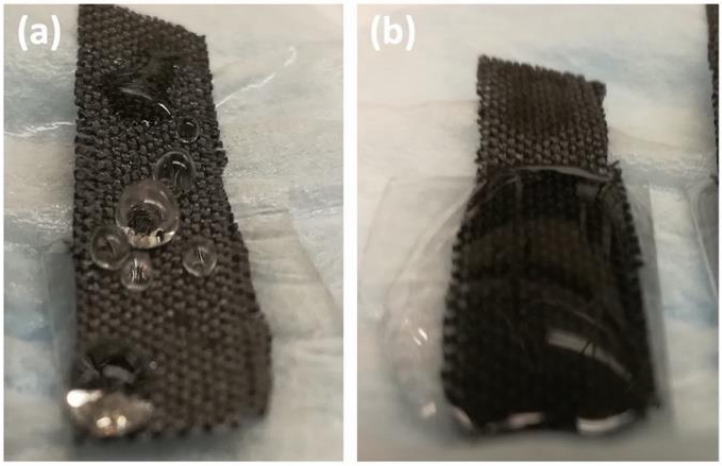


Figure 3.3 Images of water droplet deposited on carbon cloth:

(a) before and (b) after carbon activation.

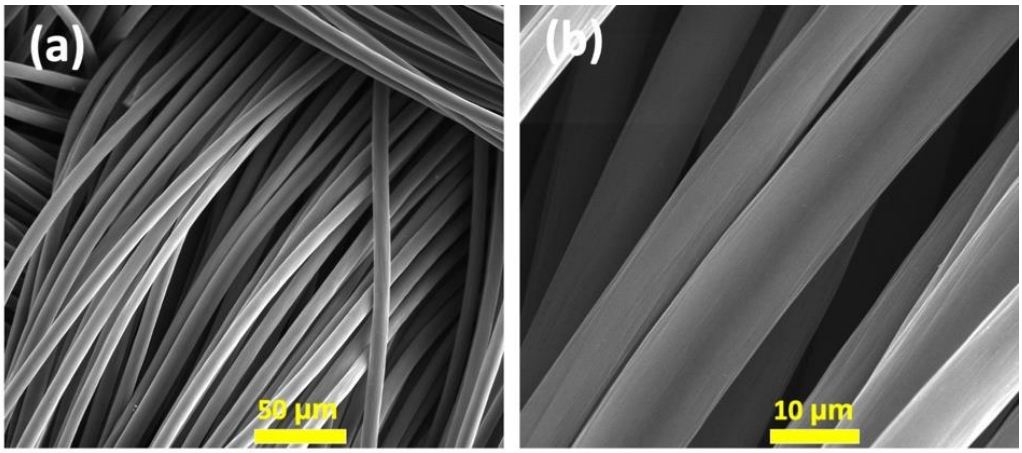


Figure 3.4 SEM images of the electrochemically activated carbon cloth.

As demonstrated in the SEM images of Figure 3.5 and the energy dispersive X-ray spectrometry (EDS) elemental mapping of Figure 3.6, the Ag-Sn deposition coverage was augmented. However, poor adhesion of the coating to the substrate was still observed, with some material detaching from the surface during the water rinse. In order to improve coverage and enhance adhesion, a pulse-electrodeposition method was utilized to synthesize Ag3Sn on the activated carbon cloth surface.

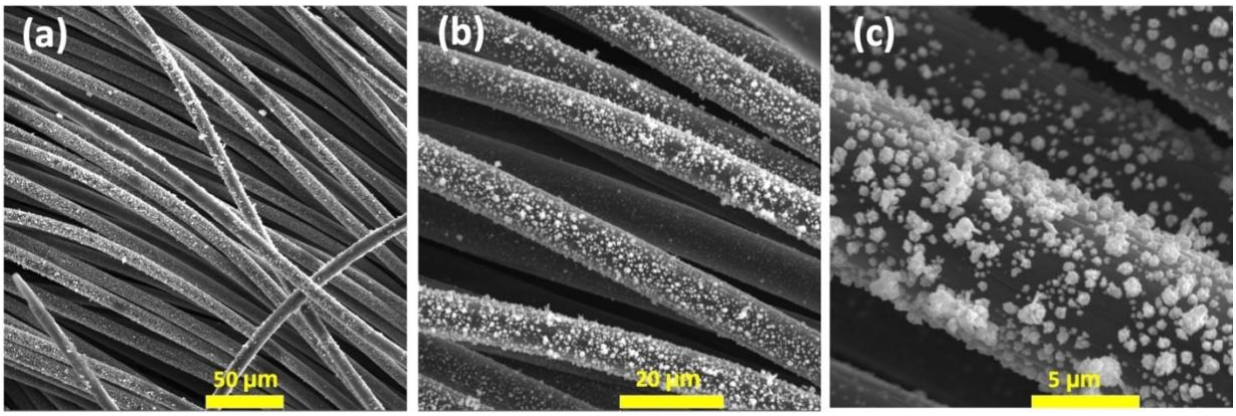


Figure 3.5 SEM images of Ag-Sn:

Electrodeposited during 3 hours at a constant potential of -0.65 V vs. Ag/AgCl on activated carbon cloth.

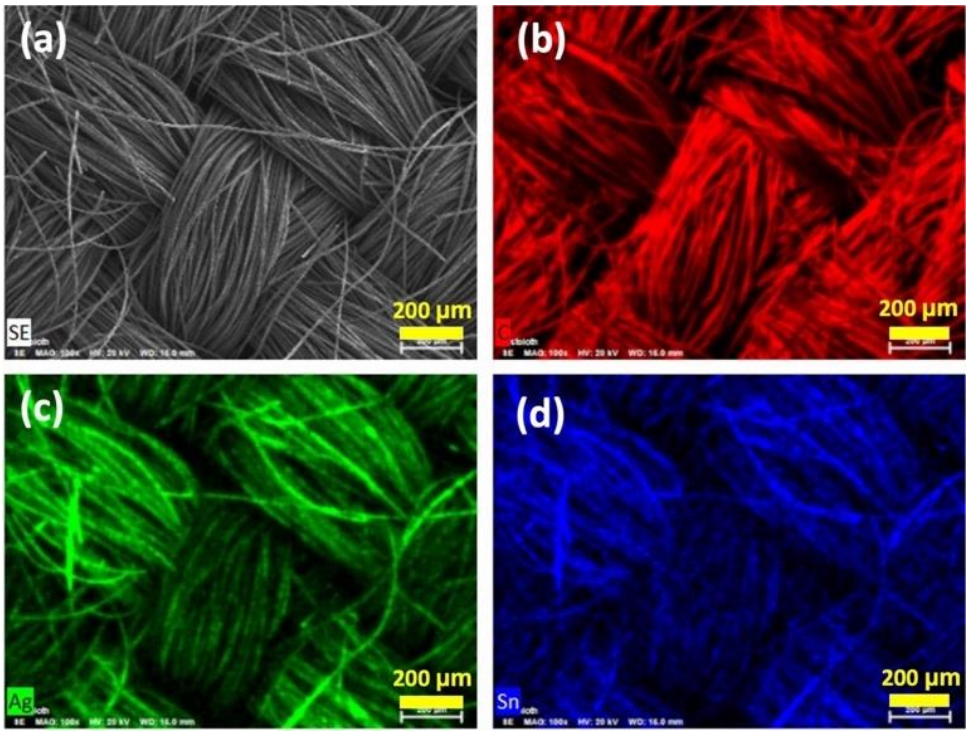


Figure 3.6 Energy-dispersive X-ray spectroscopy elemental mapping of Ag-Sn.

Electrodeposited on activated carbon cloth at a constant potential of -0.65 V vs. Ag/AgCl for 3 hours. (a) SEM image (b) C (c) Ag and (d) Sn elements.

Figure 3.7 presents the SEM images of samples fabricated using varying pulse durations.

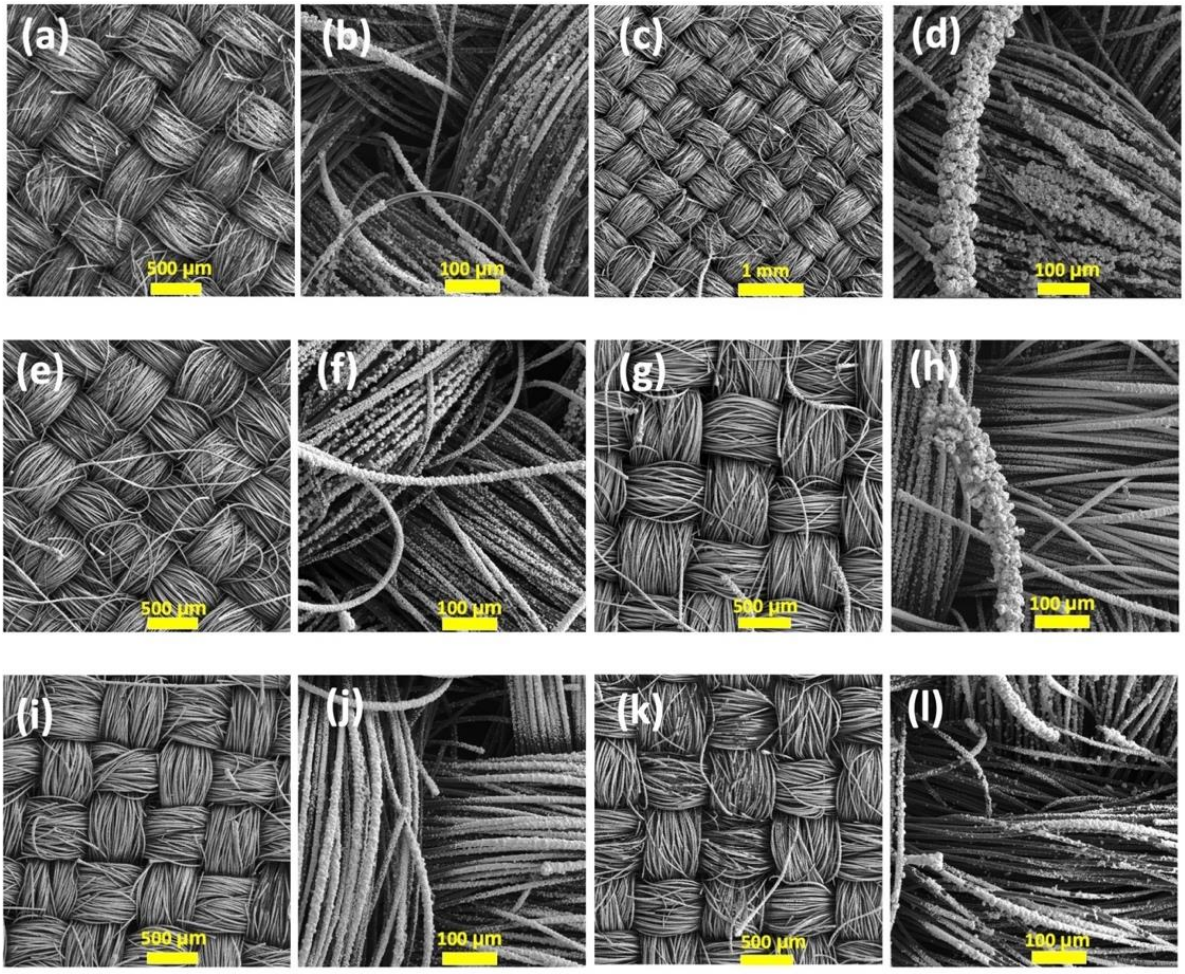


Figure 3.7 SEM images of Ag-Sn pulse electrodeposited on activated carbon cloth.

At -0.65 V vs. Ag/AgCl at different magnifications. The pulse on/off times are as follow. (a-b) 2 s / 1 s; (c-d) 1 s / 0.5 s; (e-f) 0.5 s / 0.25 s; (g-h) 0.25 s / 0.125 s; (i-j) 0.005s/ 0.0025s; and (k-l) 0.0025s/0.0012s.

The pulse-on/off timing was optimized to maximize catalyst loading. Figure 3.8 presents the results of the SEM and EDS elemental mapping of the sample that was synthesized under the optimized pulse conditions of 0.005 s on and 0.0025 s off. As demonstrated in Figure 3.8 (a–c), the Ag-Sn coating exhibits uniform coverage of the activated carbon cloth surface, with micron-sized particles distributed evenly across the substrate. At higher magnifications, the granular nature of the film becomes more apparent. Each agglomerated particle, typically less than 1 µm in size, consists of smaller grains, with sizes as low as 0.1-0.2 µm that have grown on one another, forming clusters with a rough texture. Figure 3.8 c, taken from a more internal region of the carbon cloth, highlights these particles more distinctly, where the coverage appears slightly sparser due to limited deposition in deeper areas. The elemental distribution maps depicted in

Figure 3.8 (d–g) substantiate the homogeneous dispersion of silver and tin over the substrate's surface.

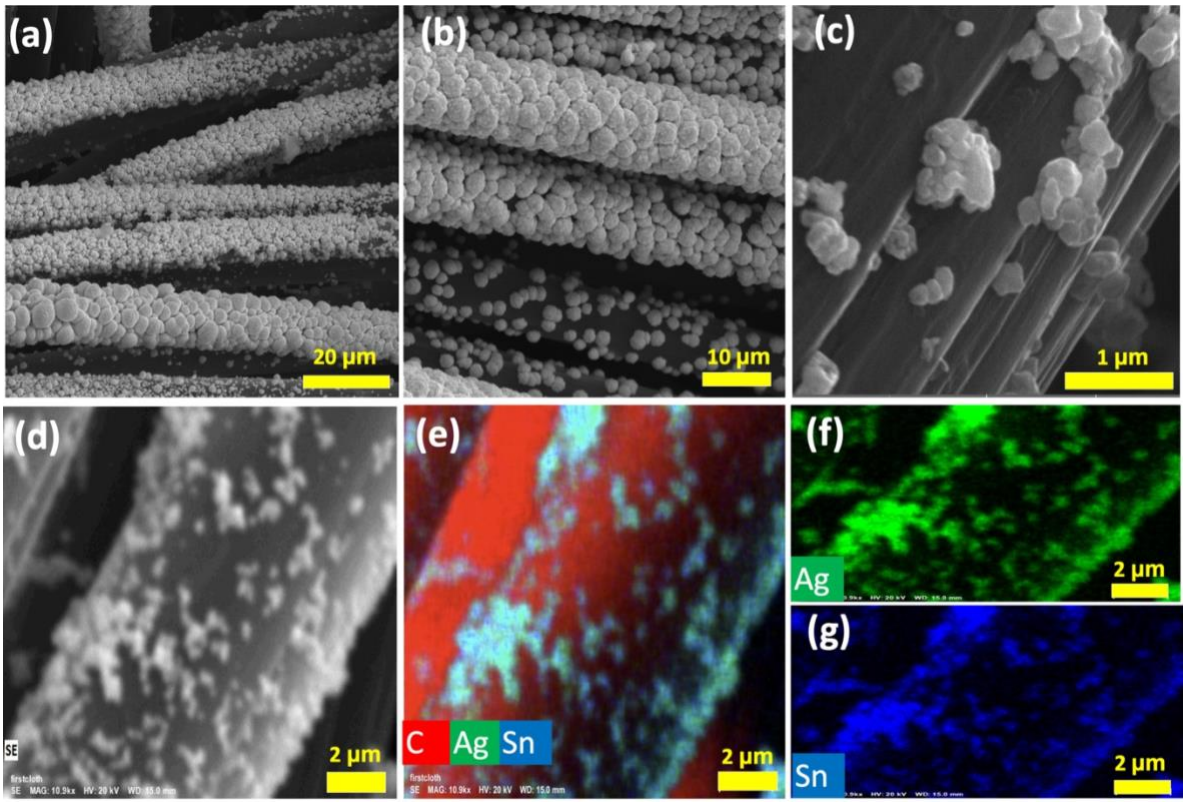


Figure 3.8 (a-c) SEM images of the Ag-Sn coating on activated carbon cloth;

(d) SEM image with corresponding EDS elemental mapping of (e) C, Ag, and Sn combined, (f) Ag, and (g) Sn separately.

EDS analysis revealed a composition of 18.5 at% Ag, 5.4 at% Sn, and 76.1 at% C. Figure 3.9 presents the X-ray diffraction analysis (XRD) pattern of the synthesized sample, showing diffraction peaks corresponding to Ag_3Sn (ICDD 01-071-0530). Additional peaks at 25.4° and 43.5° are attributed to the carbon substrate [133]. Scherrer analysis of the diffraction peaks gives an average crystallite size of ~26 nm, which is markedly smaller than the micrometer-sized particles observed by SEM (Figure 1c). This confirms that the micrometer-scale particles are polycrystalline aggregates composed of nanometer-sized crystallites.

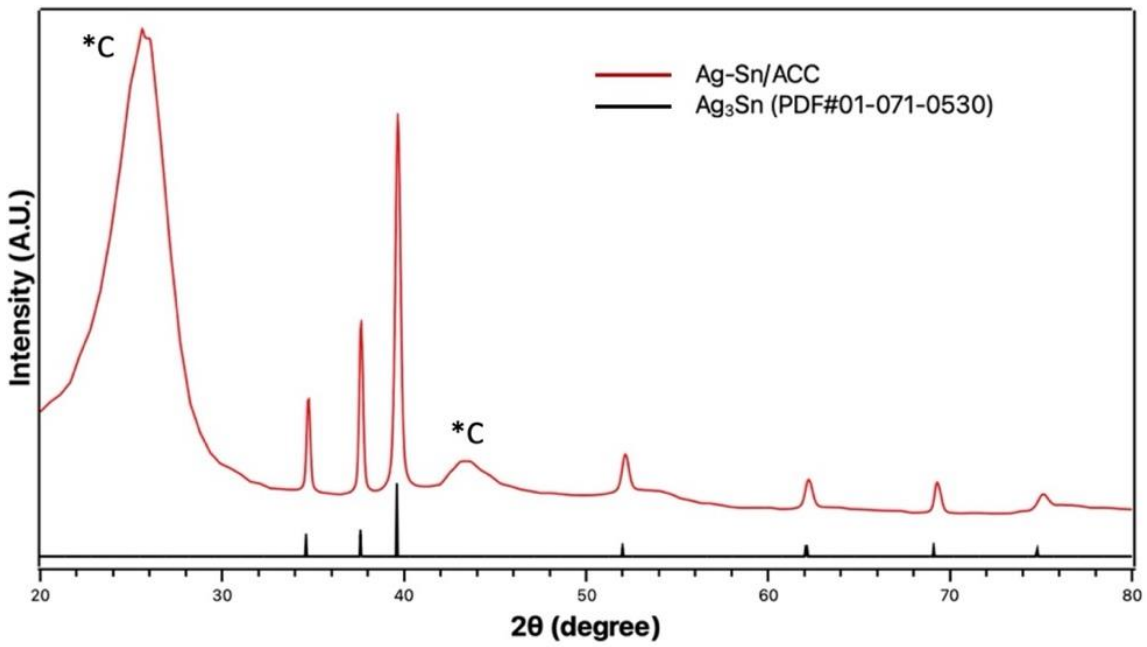


Figure 3.9 XRD pattern of the synthesized Ag_3Sn on activated carbon cloth substrate.

3.3.2 NRR electrocatalytic performance

The NRR activity of Ag3Sn/ACC samples was evaluated in a 2 M KOH solution (pH = 13.5). To purify the purging gas, different chemical traps were placed along its flow path (see Figure 3.10).

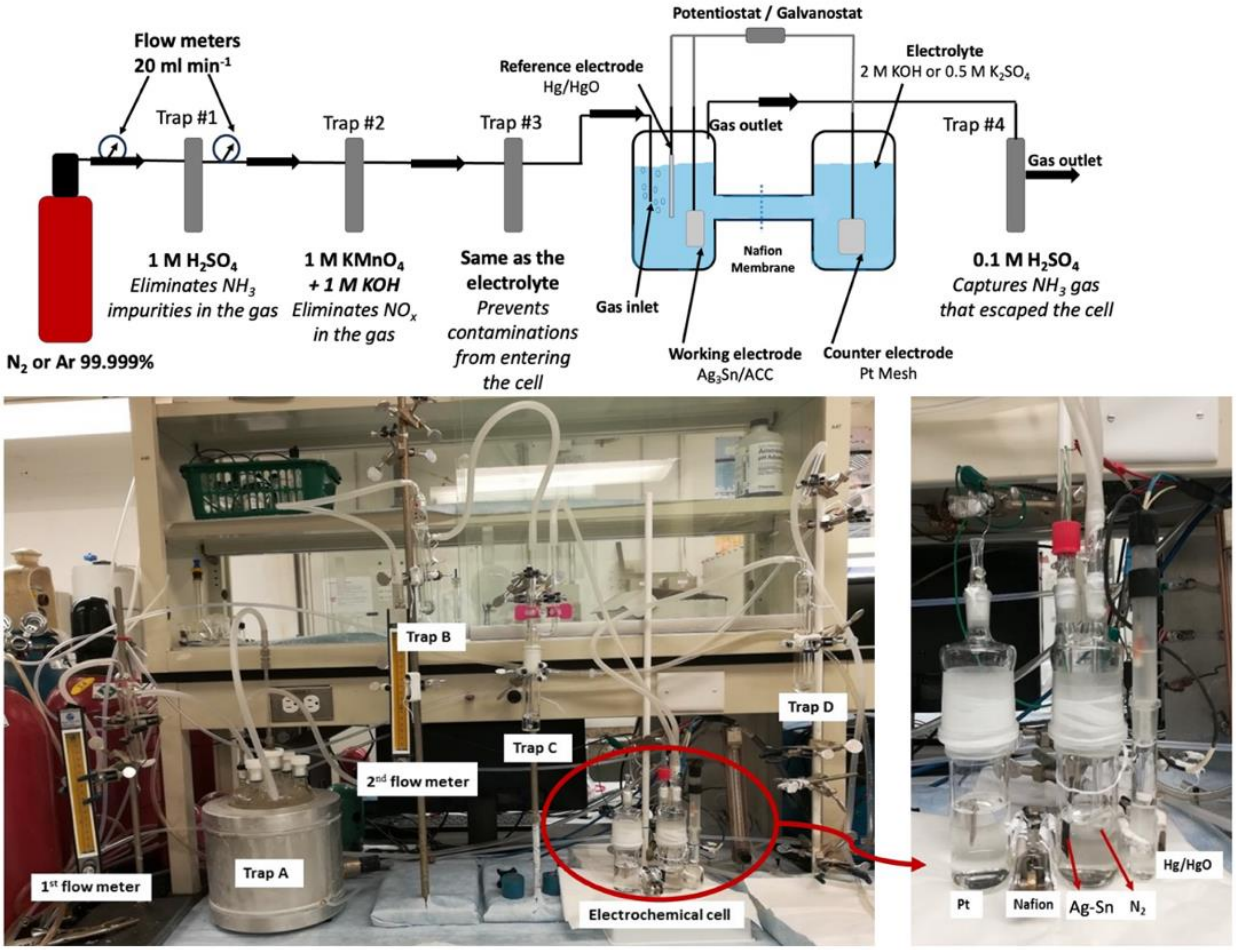


Figure 3.10 Schematic (top) and photograph of the system (bottom)

that was used to purify the purging gas and the electrochemical cell used for examining NRR.

The calibration curves employed for the measurement of NH_3 in various electrolytes and in the 0.1 M H_2SO_4 trap are presented in Figure 3.11. The estimated limits of detection for the 2 M KOH electrolyte and 0.1 M H_2SO_4 trap solution were 38.8 and 16.6 μM (equals to 0.7 and 0.3 μg/ml), respectively.

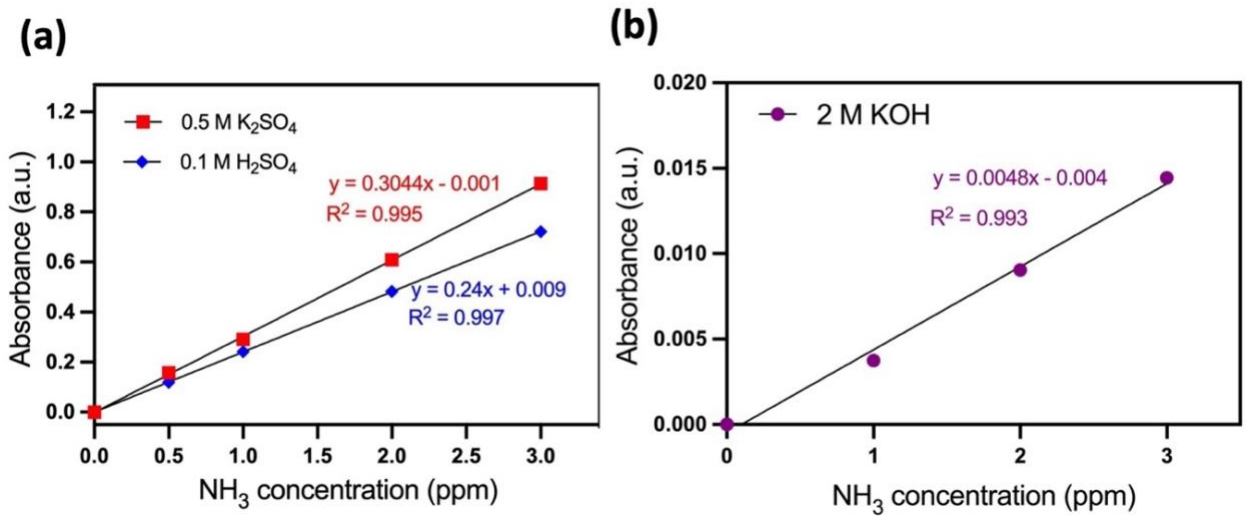


Figure 3.11 Calibration curves used to detect NH_3.

In (a) 0.5 M K_2SO_4 and 0.1 M H_2SO_4, and (b) 2 M KOH.

Representative chronoamperometric curves are presented in Figure 3.12 for the Ag_3Sn/ACC specimen in 2 M KOH under a potential of -0.6 V *vs.* RHE. The electrolytes were purged with either Ar or N_2. The current density exhibited a nearly identical response independent of the nature of the gas purged into the electrolyte. The NH_3 concentration was found to be below the detection limit in both the KOH electrolyte and the H_2SO_4 trap.

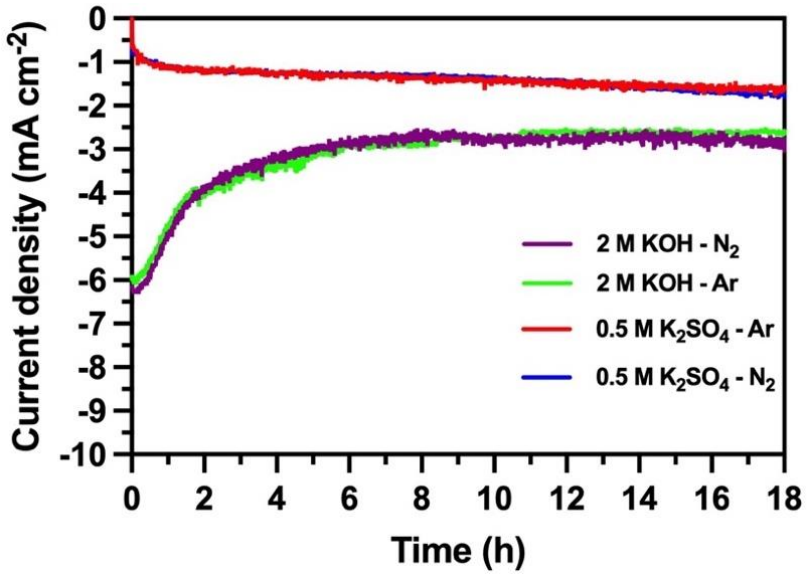


Figure 3.12 Chronoamperometric curves of the Ag_3Sn/ACC samples.

At -0.6 V *vs.* RHE in 2 M KOH solution and 0.5 M K_2SO_4 solutions. The cell was purged with either Ar or N_2.

The NRR activity of the Ag_3Sn/ACC sample was also evaluated in neutral 0.5 M K_2SO_4 electrolyte (pH = 7.0). The chronoamperometric curves under a potential of -0.6 V *vs.* RHE are presented in Figure 3.12 in both Ar- and N_2-purged 0.5 M K_2SO_4 electrolyte. In this electrolyte, as in the 2 M KOH electrolyte, the current density exhibited a nearly identical response independent of the nature of the gas purged into the electrolyte. However, the current responses were lower in 0.5 M K_2SO_4 than in 2 M KOH. It can be inferred that this phenomenon is most likely a consequence of the elevated HER rate observed in 2M KOH, a finding that can be attributed to the increased alkalinity of the medium and the elevated concentration of cations [134,135].

Figure 3.13 presents the total amount of NH_3 measured in the 0.5 M K_2SO_4 electrolyte purged by N_2 and Ar after the 18-hour test under different applied potentials.

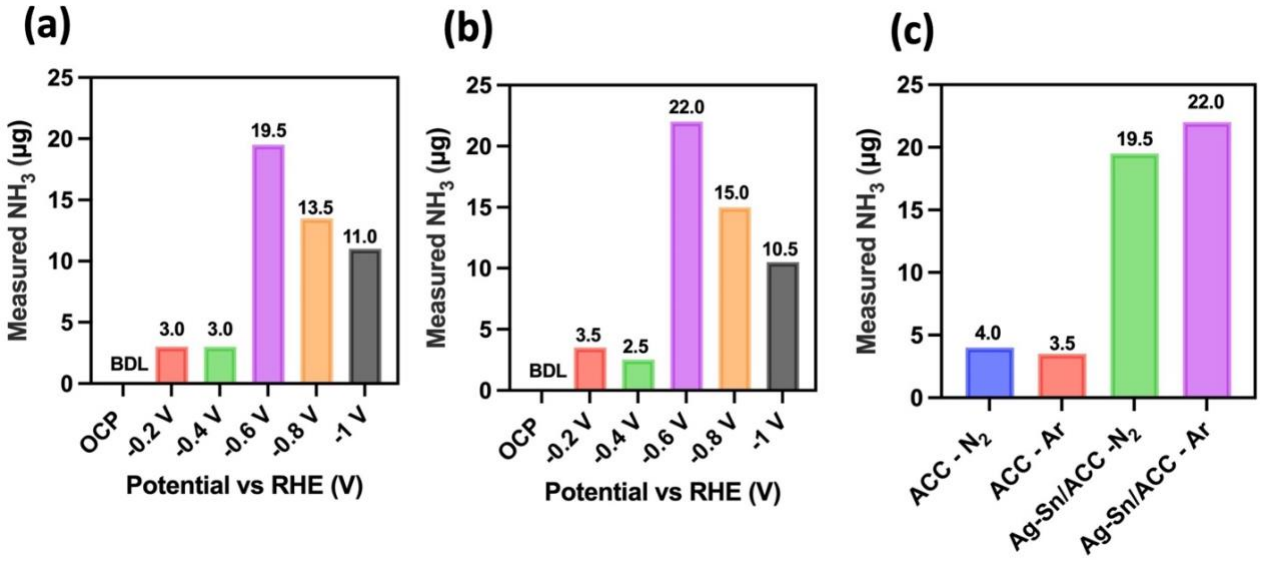


Figure 3.13 Amount of NH_3 after the 18-hour test.

Under open circuit potential and different applied potentials performed using freshly prepared Ag_3Sn/ACC samples in each case; the electrochemical cell was purged by (a) N_2, and (b) Ar. (c) Amount of NH_3 after the 18-hour control tests that were run at -0.6 V *vs.* RHE on ACC and Ag_3Sn/ACC. The electrolyte used was 0.5 M K_2SO_4 solution, and the purging gas is indicated.

The corresponding NH_3 concentrations are listed in Table 3.1.

Table 3.1 Concentration of NH_3.

Electrode	Potential (V vs. RHE)	Gas purged into the system	NH_3 measured in the electrolyte (ppm)	NH_3 measured in the H_2SO_4 trap (ppm)	Total NH_3 (µg)
Ag_3Sn/ACC	-0.2	N_2	BDL	0.6	3.0
Ag_3Sn/ACC	-0.4	N_2	BDL	0.6	3.0
Ag_3Sn/ACC	-0.6	N_2	0.4	1.5	19.5
Ag_3Sn/ACC	-0.8	N_2	0.4	0.3	13.5
Ag_3Sn/ACC	-1	N_2	0.3	0.4	11.0
Control test Ag_3Sn/ACC	OCP	N_2	BDL	BDL	BDL
Control test ACC	-0.6	N_2	BDL	0.8	4.0
Control test ACC	-0.6	Ar	BDL	0.7	3.5
Control test Ag_3Sn/ACC	OCP	Ar	BDL	BDL	BDL
Control test Ag_3Sn/ACC	-0.2	Ar	BDL	0.7	3.5
Control test Ag_3Sn/ACC	-0.4	Ar	BDL	0.5	2.5
Control test Ag_3Sn/ACC	-0.6	Ar	0.5	1.4	22.0
Control test Ag_3Sn/ACC	-0.8	Ar	0.4	0.6	15.0
Control test Ag_3Sn/ACC	-1.0	Ar	0.3	0.3	10.5

In the 0.5 M K_2SO_4 electrolyte (30 ml) and in the 0.1 M H_2SO_4 trap (5 ml) after performing each test for 18 hours at -0.6 V vs. RHE on Ag_3Sn sample deposited on activated carbon cloth (ACC) and on ACC as the control test. BDL is the acronym for "Below Detection Limit".

In each case, freshly synthesized samples were used. In this study, the amount of NH_3 was reported in mass (µg) rather than concentration units (e.g., µg/mL), and the total amount of NH_3 was calculated by summing the amounts measured in the electrolyte (30 mL) and in the trap (5 mL). Interestingly, except for the open circuit potential conditions (OCP), NH_3 was detected at all the different potentials. Initially, NH_3 production increases as the electrode potential becomes

more negative up to -0.6 V *vs.* RHE, then declines at more negative potentials (Figure 3.13 a). The maximum amount of NH3 was 19.5 µg at -0.6 V *vs.* RHE. The previous results suggest that the NRR activity of the Ag3Sn/ACC sample in neutral 0.5 M K_2SO_4 electrolyte is maximum at -0.6 V *vs.* RHE. The trend observed in this graph aligns with several studies that reported NRR activity for catalysts in aqueous solution [136,137]. However, verifying the source of NH_3 to be the reduction of N_2 at the surface of the catalyst is crucial. To do that, four control tests were done in 0.5 M K_2SO_4 solution using freshly synthesized samples to perform each of the control tests.

In the first control test, the Ag_3Sn/ACC sample was immersed in the K_2SO_4 solution and purged with N_2 for 18 hours without applying any potential (open circuit conditions). In the second test, the same procedure was followed using Ar instead of N_2. In both cases, the amount of NH_3 in the electrolyte and in the trap was below the detection limit. This confirms that the purging gases (N_2 and Ar) were free of NH_3 and that no measurable NH_3 contamination originated from the laboratory equipment (e.g., nitrile gloves, gas tubes, or glassware).

For the third control test, an ACC electrode was utilized in replacement of an Ag_3Sn/ACC electrode, and a potential of -0.6 V *vs.* RHE was applied. In this instance (Figure 3.13 c), 4.5 µg and 3.5 µg of NH_3 were produced under N_2 and Ar gas purging, respectively, a significant decrease compared to the 19.5 µg yielded by Ag_3Sn/ACC at the same electrode potential and under N_2 purging. These results suggest, at this stage, that Ag_3Sn is responsible for NH_3 production.

In the fourth and final control test, the system was purged with Ar instead of N_2. In that case, the electrode potential was varied, with freshly prepared Ag_3Sn/ACC electrodes utilized at each applied potential. As demonstrated in Figure 3.13, the presence of NH_3 was observed at all tested potentials under Ar, with values comparable to those detected under N_2. At the potential where NH_3 production was maximal (19.5 µg at −0.6 V *vs.* RHE), the amount measured under Ar was 22.0 µg, which exceeded the amount produced when N_2 gas was fed into the system.

Overall, the results in 2 M KOH and 0.5 M K_2SO_4 solutions showed that the Ag_3Sn alloy is inactive for the electroreduction of N_2 to NH_3 in aqueous media. The test in 0.5 M K_2SO_4, however, showed a false positive, while the one in 2 M KOH did not show any detectable NH_3. This can be explained by the poorer detection limit in 2 M KOH (≈0.7 µg/mL) compared to 0.5 M K2SO4 solution (≈0.3 µg/mL), as the maximum amount of NH_3 produced in 0.5 M K_2SO_4 was around 0.5 µg/mL, which would fall below the detectable range if similar levels were generated in the 2 M KOH solution.

It is worth noting that when the same cathode was reused for a second 18-hour electrolysis test in 0.5 M K_2SO_4, after being previously operated for 18 hours at -0.6 V vs. RHE, the results changed significantly. In the first run, 19.5 µg and 22.0 µg of NH_3 were detected under N_2 and Ar, respectively, while in the second run with the reused cathode and fresh electrolyte under identical conditions, the NH_3 amount dropped below the detection limit. Since all other parameters (electrolyte composition, potential, duration, and setup) were identical and only the cathode had undergone prior electrolysis, this result suggests that the NH_3 detected in the first run originated from the reduction of N-species initially present on the cathode surface. Similar observations have been reported in previous studies, where repeated tests on the same Pt/C electrode showed no NH3 production after the initial run, where the authors attributed the first detected NH_3 to the reduction of pre-existing N-species rather than N_2 reduction. Therefore, when following protocols where the N_2 test is conducted before the Ar test under identical conditions such as the one proposed by Andersen et al, it is important to ensure that both the electrode and electrolyte are freshly prepared. Otherwise, N-residues may already be depleted in the first test to produce NH3, leading to a misleadingly low/zero NH_3 yield in the subsequent Ar test.

It should, however, be noted that while a properly conducted Ar control test can help identify potential false positives, it cannot by itself confirm genuine NRR activity. If the Ar control test still shows apparent NRR activity, additional experiments, such as tests with a fixed amount of N_2, and quantitative isotopic $^{15}N_2$ labeling, should be performed to verify the true NRR activity of the catalyst.

3.3.3 Computational results

The NRR starts with the adsorption of N_2 on the surface of Ag_3Sn (001) as a non-electrochemical step. The selection of the (001) surface was guided by the XRD data shown in Figure 2, where the (001) reflection corresponds to the most intense diffraction peak, indicating its dominance under experimental conditions. In addition, previous computational studies have reported that the (001) facet possesses the lowest surface energy among the low-index planes, confirming its thermodynamic stability and justifying its choice for the DFT investigation.

The structure of the Ag_3Sn (001) can be seen in Figure 3.14.

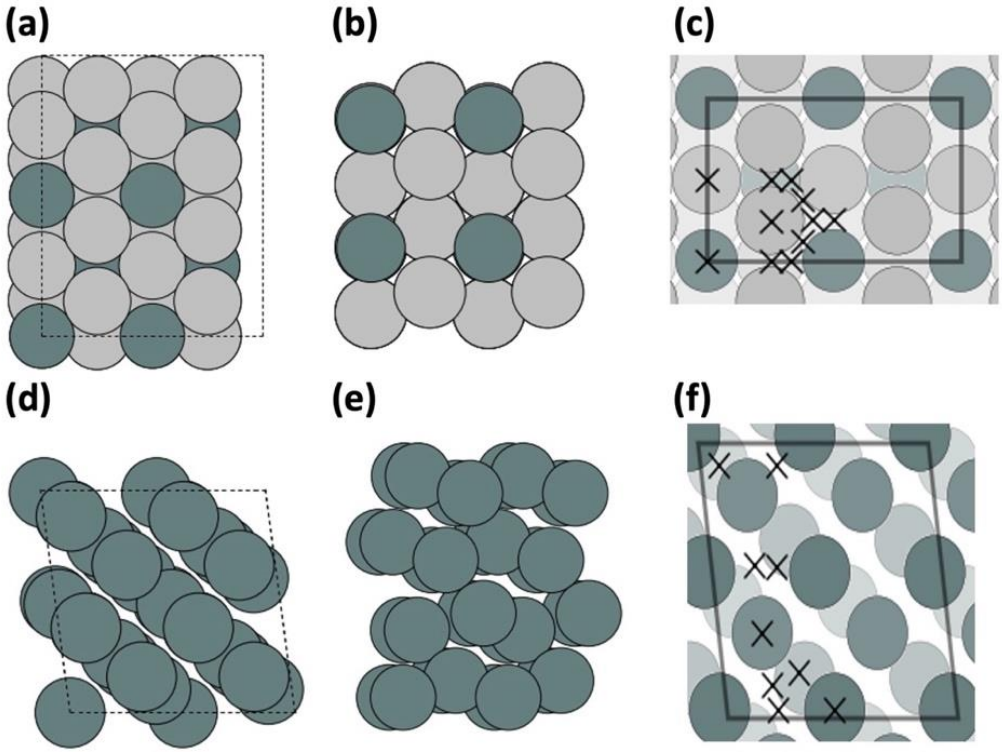


Figure 3.14 (a, b) Top and side views of Ag_3Sn (100) structure, respectively. (d, e) Top and side views of Sn (100) structure, respectively. (c, f) Adsorption sites investigated to determine the minimum energy configurations of NRR intermediates. Silver atoms are shown in gray, and tin atoms in green.

To find the minimum energy configuration, we investigated 11 different adsorption sites as depicted in Figure Figure 3.14 c. The calculated adsorption free energy for N_2 (ΔG_{*N_2}) on the surface of Ag_3Sn is 0.21 eV uphill in free energy (Figure 3.15).

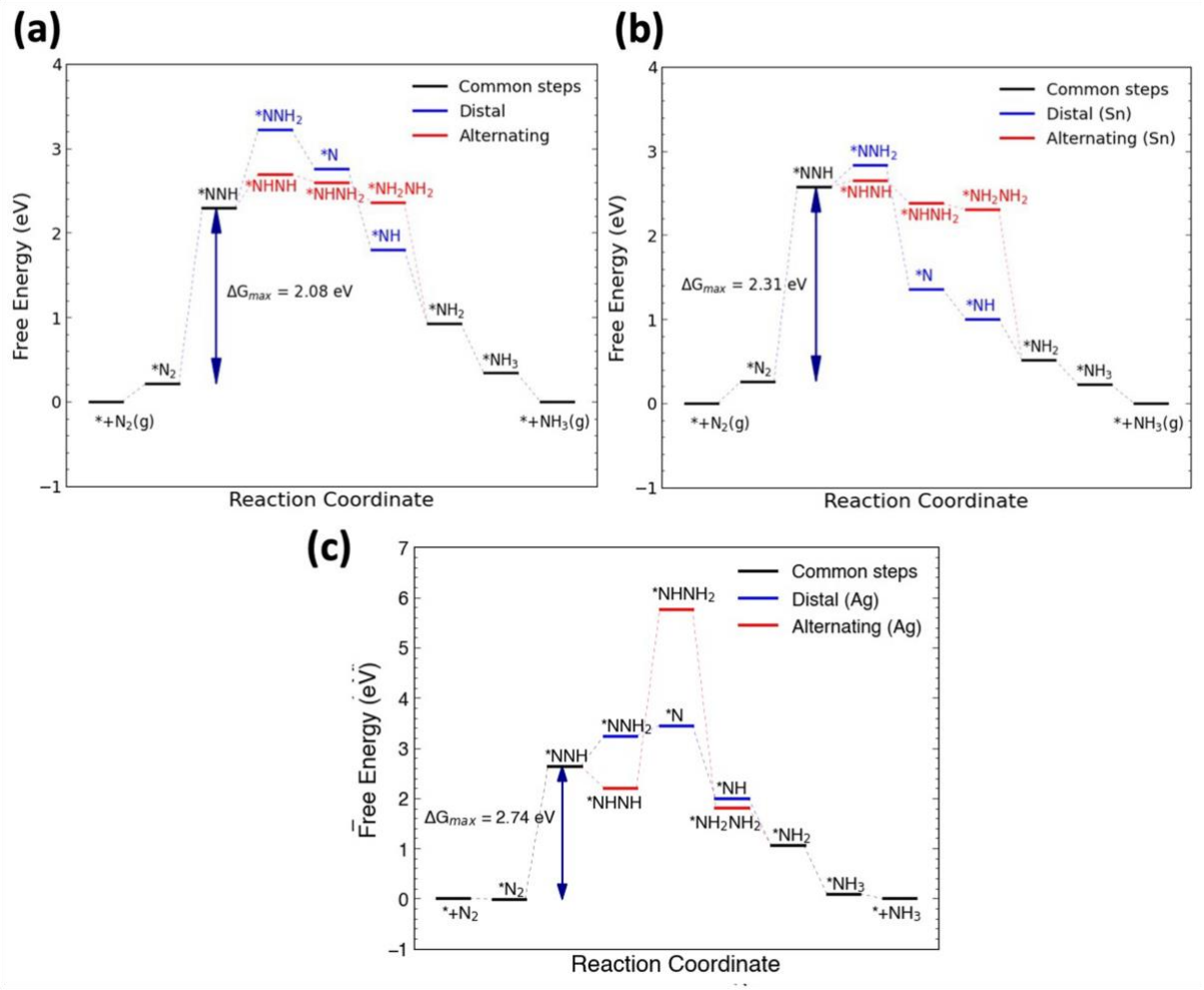


Figure 3.15 Free energy profiles of the distal and alternating pathways of the NRR.

For (a) Ag_3Sn (001), (b) β-Sn (100), and (c) Ag (111). The steps common to both pathways are shown in black, while intermediates specific to the distal and alternating pathways are indicated in blue and red, respectively. The PLS is marked with double-headed arrows.

Moreover, the N≡N bond length remained unchanged at 1.10 Å compared to that calculated for the isolated N_2 molecule, indicating no interaction between the surface and N_2. Moreover, the projected density of states (PDOS) confirms that there is no interaction between Ag_3Sn surface and N_2 as there is no significant change in the p-states of N_2 (Figure 3.16).

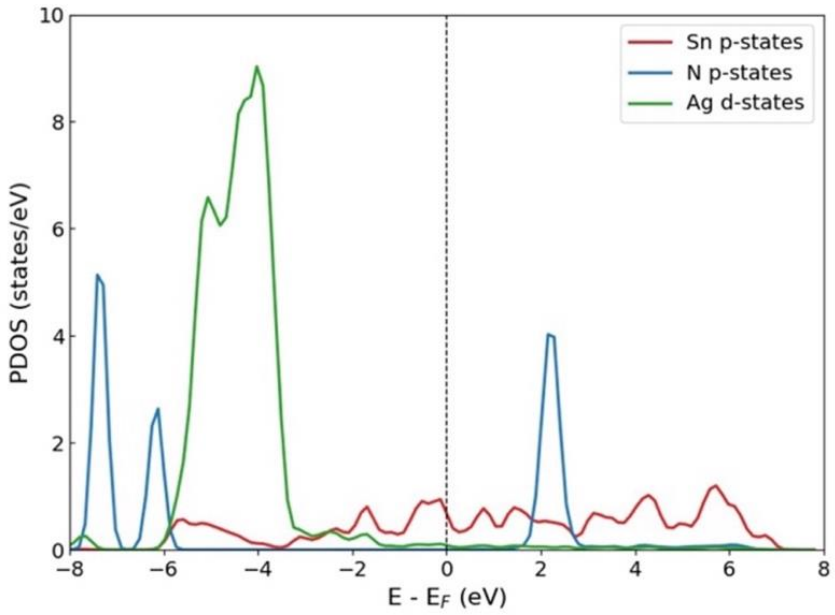


Figure 3.16 The PDOS of Ag_3Sn, showing d-states of Ag (green), p-states of Sn (red), and N (blue) for Ag_3Sn and physisorbed N_2.

Bader charge analysis also shows no charge transfer between $*N_2$ and Ag_3Sn. The weak interaction between N_2 and Ag is expected due to its low-lying d-states (Figure 3.16), however, some studies have claimed a strong interaction between the p-states of p block elements like Sn with N2 [47,138]. Therefore, we calculated the ΔG_{*N_2} on the surface of β-Sn (100), considering nine different adsorption sites (Figure 3.14 f). However, the calculated ΔG_{*N_2} was found to be 0.25 eV, indicative of an endergonic process and of a weak interaction between N_2 and Sn. This finding contrasts with previous reports that suggest a more favorable adsorption of N_2 on Sn-based catalysts.

The next step for NRR is the hydrogenation of $*N_2$ to *NNH that is 2.08 eV uphill in free energy on the surface of Ag_3Sn. The second electrochemical step is the hydrogenation of *NNH to $*NNH_2$ or *NHNH, which discriminates between distal and alternating pathways, respectively. The formation of *NHNH is less uphill in free energy compared to that of $*NNH_2$ and thus it is expected that NRR will proceed via the alternating pathway on the surface of Ag_3Sn. As depicted in Figure 4a, all proton-electron transfer steps become exergonic after the second hydrogenation step for distal and alternating pathways. Finally, the desorption of NH_3 from the surface is exergonic, which was expected due to the weak interaction between the surface and N_2. We evaluated $U_{limiting}$ by considering the largest free energy change for the electrochemical steps, which makes the $*N_2$

→ *NNH the potential limiting step (PLS) for the overall NRR. The large free energy change associated with the PLS is due to the poor activation of N_2 on the surface of the electrocatalyst. The minimum energy configuration of all NRR intermediates on the surface of Ag_3Sn is shown in Figure 3.17.

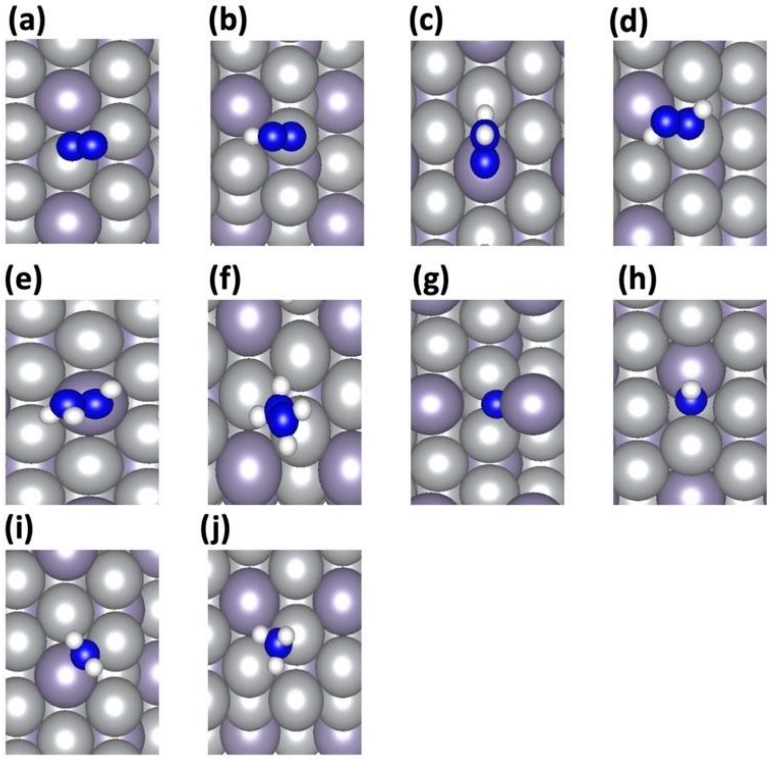


Figure 3.17 Minimum energy configuration of NRR intermediates on the surface of Ag_3Sn (Ag: silver, Sn: purple, N: Blue, H: White) for distal and alternating pathways: (a) N_2, (b) N_2H, (c) NH_2, (d) NHNH, (e) $NHNH_2$, (f) NH_2NH_2, (g) N, (h) NH, (i) NH_2, and (j) NH_3.

We also characterized the free energy profile for distal and alternating pathways on the surface of β-Sn (100) (Figure 3.15). As discussed earlier, the adsorption of N_2 is endergonic on β-Sn (100), similarly to adsorption on the Ag_3Sn surface, which results in a high free energy change for the first electrochemical step. The $*N_2$ → $*N_2H$ step is 2.31 eV uphill in free energy and this step is the PLS over β-Sn (100). Similarly to Ag_3Sn, *NHNH formation is less uphill in free energy compared to $*NNH_2$ formation, which makes the alternating pathway more favorable on β-Sn (100). All the remaining electrochemical steps and the desorption of NH_3 are downhill in free energy. We compare $U_{limiting}$ for Ag_3Sn (001), β-Sn (100) and Ag (111) in Figure 3.15. Despite a slightly lower Ulimiting of -2.08 V for Ag_3Sn compared to -2.31 V for β-Sn (100) and -2.74 V for

Ag (111), we predict that the Ag_3Sn alloy is inactive for NRR as it still requires high overpotentials ($\eta_{theoretical}$ = -2.14 V) for NRR at which HER will be dominant.

To enhance the catalytic activity and selectivity of an electrocatalyst, one should tune the electronic properties of the active site. As previously discussed, alloying is a simple yet effective strategy to modify the electronic structure of active sites. However, in our case, alloying did not significantly improve the activity, which can be further understood by examining the electronic structure of the active site, *i.e.* the PDOS of Ag_3Sn and β-Sn (100). Figure 3.18 compares the PDOS of the p states of Sn in the Ag_3Sn alloy and the Sn (100) surface. As shown, there is no substantial change in the PDOS of Sn, except a slight upshift of Sn *p*-states in the alloy, relative to pure Sn (100), that is consistent with Bader charge analysis, which reveals a net charge transfer of 0.20 e^- from Sn to neighboring Ag atoms. Although Sn is slightly more electronegative than Ag (1.96 vs. 1.93 on the Pauling scale), the surface coordination of Sn with six Ag atoms drives charge transfer from Sn to Ag. These results indicate that alloying Sn with Ag does not effectively modulate the electronic structure of Sn or Ag to enhance the catalytic activity of Ag_3Sn. The effectiveness of alloying critically depends on the choice of metals, as modulation of the electronic structure primarily arises from interatomic charge transfer. Notably, alloying *d*-metals with *p*-metals may not induce substantial changes in the electronic properties of the active site.

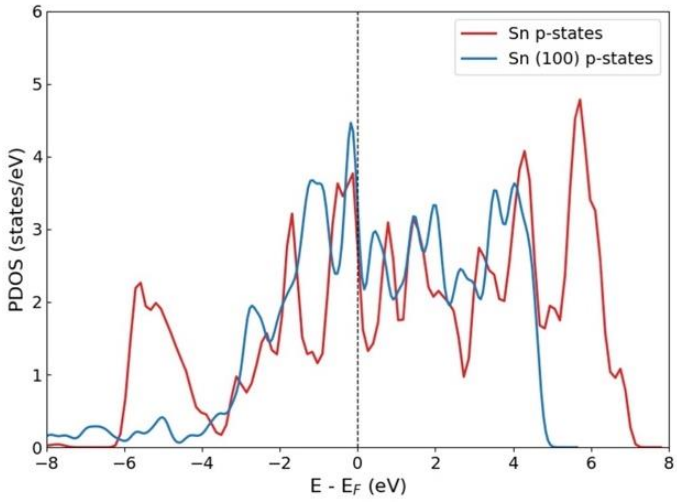


Figure 3.18 PDOS of into p-states for Sn in Ag_3Sn and β −Sn (100)

shown by red and blue, respectively. A noticeable change in PDOS is the peak between -6 eV and -4 eV in the Ag_3Sn, attributed to the hybridization of Sn p-states with Ag d-states.

The alloy's HER inertness was examined by calculating the adsorption free energies of *H and *OH, and comparing them with that of $*N_2$ to elucidate its surface affinity, as shown in Figure 6. DFT calculations show that H adsorption is endergonic (+0.60 eV), confirming intrinsically weak H binding and, therefore, poor HER activity on the surface of Ag_3Sn. Moreover, *OH adsorption is only mildly endergonic (+0.12 eV), indicating weak hydroxyl affinity and suggesting that significant OH coverage would require more alkaline potentials and/or specific interfacial stabilization, making persistent *OH poisoning unlikely under our standard conditions. These results confirm that the alloy was correctly designed to suppress HER.

While such comparisons help assess the intrinsic activity and selectivity of the alloy toward N_2 reduction, they do not account for other nitrogen-containing species that can also yield NH_3 under electrochemical conditions. Given our experimental observation that pre-existing N-species on the cathode surface can produce NH_3 even without N_2 activation, it was essential to consider possible alternative reaction pathways. Among these, nitrogen oxides (NO_x) are particularly important, as they are widely recognized in the literature as a major source of false-positive NH_3 detection in NRR studies. To clarify this possibility, we extended our DFT analysis to examine the adsorption and reduction energetics of NO and NO_2 species on Ag_3Sn.

Figure 3.19 compares the adsorption free energies of *NO and $*NO_2$ on the alloy surface and compares them to that of N_2. Results indicate that the adsorption free energy of NO (–0.11 eV) and NO_2 (–1.10 eV) is more favorable than that of $*N_2$ (+0.21 eV), showing that NO_x interacts more strongly with the surface. This strong adsorption implies that once NOx species are present, they can easily occupy surface sites and undergo reduction, potentially producing NH_3 even when N_2 activation is thermodynamically unfavorable. The strong alloy–NO interaction originates from the unpaired electron on the nitrogen atom of NO, which enhances its interaction with the surface of the alloy. This contrasts with molecular N_2, whose triple bond and closed-shell structure make adsorption and activation far more difficult. These findings highlight that NO_x reduction can outcompete N_2 activation on this surface, underscoring the importance of eliminating trace NO_x contamination when evaluating NRR activity. In other words, the alloy's apparent selectivity toward NH_3 formation may partly arise from NO_x reduction rather than from direct N_2 reduction. This observation led us to further investigate the nitrogen oxide reduction reaction (NORR) and the NO_2 reduction reaction (NO_2RR) mechanisms, as described in the following section.

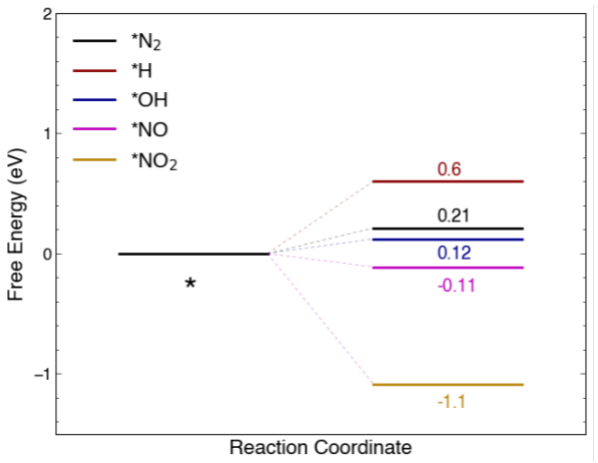


Figure 3.19 Adsorption free energies of key intermediates for competing reactions (*N_2, *H, *OH, *NO, and *NO_2) on the alloy surface.

The reduction of nitric oxide (NORR) follows a five-electron transfer reaction and a simpler pathway than the NRR. The process begins with the adsorption of *NO on the surface of the alloy, which is thermodynamically more favorable compared to that of *N_2 as discussed earlier. During the first proton–electron transfer step, the adsorbed *NO is hydrogenated to form *NOH which is 0.48 eV uphill in free energy (Figure 3.20 a). Further hydrogenation of *NOH leads to the formation of *N and the release of a water molecule, after which the pathway proceeds through *NH, *NH_2, and finally *NH_3 similar to the later stages of the NRR. As a result, the overall free-energy profile of the NORR lies consistently below that of the NRR, confirming that NO reduction is energetically more favorable. These results suggest that in the presence of even trace amounts of NO, NORR can dominate over both NRR and HER, providing a plausible explanation for the observed NH3 formation under experimental conditions.

The NO_2 reduction reaction (NO_2RR) proceeds through a seven-electron pathway that begins with the adsorption of NO_2. The adsorbed NO_2 is first hydrogenated to *NO_2H which is 1.11 eV uphill in free energy (Figure 3.20 b). The next step is the formation of *NO, accompanied by the release of a water molecule. The following hydrogenation steps are similar to those of NORR. Overall, these results confirm that the NO_2RR pathway is energetically favored over both NRR and HER. Interestingly, the PLS of NORR and NO_2RR is the hydrogenation of *N to *NH with ΔG_{max} = 2.06 eV at the surface of Ag_3Sn which is close to that of NRR (ΔG_{max} = 2.08 eV).

These findings underline a broader methodological implication for computational investigations of NRR. Computational studies that assess catalytic activity/selectivity solely based on N_2 and H adsorption may overlook critical competing reactions involving nitrogen oxides. As demonstrated

here, NO and NO_2 species bind more strongly to the alloy surface and undergo thermodynamically favorable reduction steps, which can easily lead to the formation of NH_3 even in the absence of N_2 activation. Therefore, a comprehensive computational framework for evaluating NRR activity should also include the adsorption and reduction of NO_x intermediates. Such an approach enables a more reliable distinction between genuine NRR activity and NO_x-derived NH_3 formation, ensuring that theoretical predictions are consistent with experimental observations and free from false-positive interpretations.

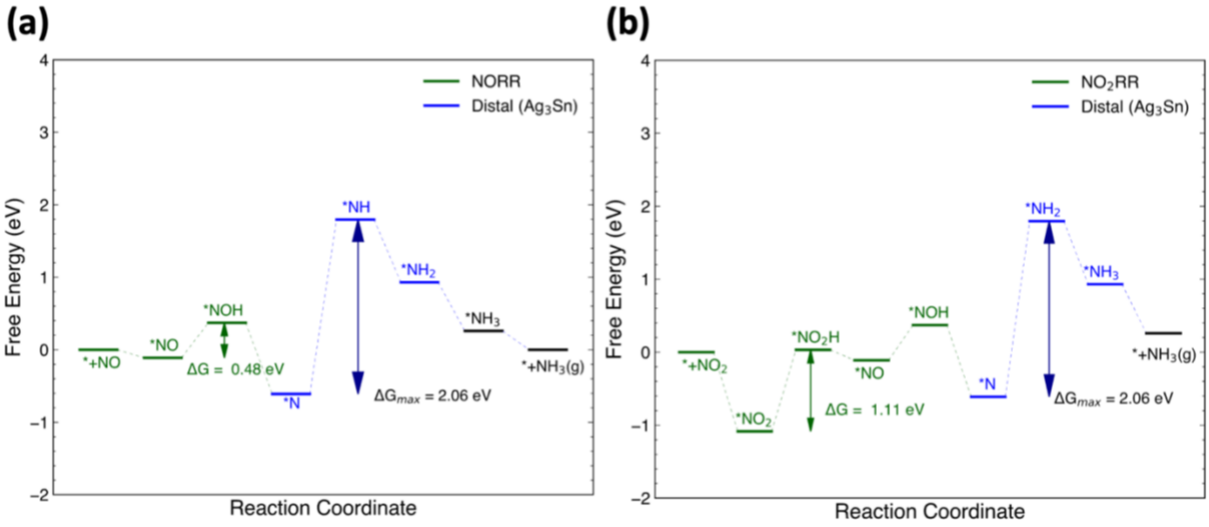


Figure 3.20. Free-energy profiles for (a) the nitric oxide reduction reaction (NORR) and (b) the nitrogen dioxide reduction reaction (NO_2RR) on the alloy surface. The green segments correspond to the NO_x reduction steps, the blue segments represent the distal NRR pathway, and the black segments denote the common intermediates for NRR.

3.4 Conclusion

Guided by reports indicating high NRR activity for Ag and Sn, complemented by their low HER activity, and the prospect of enhanced performance through p–d orbital hybridization for NRR, we undertook the synthesis of Ag_3Sn alloy through pulse electrodeposition on activated carbon cloth. Contrary to expectations, no measurable NRR activity was detected in a 2 M KOH solution following an 18-hour test at varying potentials. In the case of 0.5 M K_2SO_4, NH_3 was detected at various potentials, particularly those more negative than -0.6 V *vs.* RHE. However, when the Ar control test was performed using freshly prepared electrodes, it was observed that a comparable NH_3 amount was produced when equivalent potentials were applied. The results of the study indicated that the reduction of N-species on the cathode surface was the origin of the produced

NH_3, and Ag_3Sn was found to be inactive for the reduction of N_2 to NH_3 in the studied aqueous solutions. DFT calculations indicate that while Ag_3Sn has a slightly lower NRR $U_{limiting}$ compared to pure Ag or Sn, it nevertheless requires large overpotentials to make NRR thermodynamically feasible. The present study challenges the anticipated high NRR activity of Ag_3Sn. Also, it proposes a novel, cost-effective method for detecting false positives in the field of NRR, which consists of performing a few consecutive measurements under the same conditions and using the same electrode, looking for a decrease in the NH_3 production rate from one test to the other one.

3.5 Experimental section

3.5.1 Materials

Carbon cloth, Nafion® N-117 membrane, sulfuric acid (H_2SO_4, 95.0–98.0%), sodium citrate dihydrate ($C_6H_9Na_3O_9$, ≥ 99.0%), silver sulfate (Ag_2SO_4, ≥ 99.0%) and tin (II) sulfate ($SnSO_4$, ≥ 99.0%) were purchased from Fisher Scientific. Sodium nitroferricyanide dihydrate ($C_5FeN_6Na_2O{\cdot}2H_2O$, ≥ 99.0%), phenol ($C_6H_6O$, ≥ 99.5%), sodium hydroxide (NaOH, ≥ 99.0%), ammonium chloride (NH_4Cl, 99.5%), sodium hypochlorite solution (NaClO, chlorine ≥ 5.0%), acetone (CH_3COCH_3, ≥99.5%), and potassium permanganate ($KMnO_4$ ≥ 99.0%) were purchased from Sigma Aldrich. Milli-Q deionized (DI) water was used for rinsing samples and preparing the electrolytes. Ultrapure N_2 and Ar gases (both Grade 5.0) were purchased from Air Liquide.

3.5.2 Carbon cloth activation

Carbon cloth was cut into 2 × 1 cm^2 pieces and both sides with a total geometrical area of 4 cm^2 were used for Ag_3Sn deposition. Prior to electrochemical activation, it was rinsed with DI water and degreased in acetone using ultrasonication for 10 minutes. For carbon cloth activation, a constant current density of 60 mA cm^{-2} was applied for 10 minutes in a three-electrode cell. In this cell, the electrolyte was 2 M H_2SO_4 solutions, carbon cloth was used as the working electrode (anode), Ag/AgCl as the reference electrode, and the platinum mesh served as the counter electrode (cathode). After the activation, it was rinsed with water several times and left to dry in air.

3.5.3 Ag_3Sn electrodeposition

The activated carbon cloth was then used as the substrate for Ag_3Sn electrodeposition. To prepare the electrodeposition bath, 0.2 M $SC(NH_2)_2$, 0.025 M $SnSO_4$, and 0.01 M Ag_2SO_4 were dissolved

in 50 ml of 2 M H_2SO_4 solution. For electrodeposition, the aforementioned three-electrode cell was used, in which the activated carbon cloth was placed as the working electrode.

Firstly, Ag3Sn was electrodeposited on non-activated carbon cloth at a constant potential of -0.65 V vs. Ag/AgCl. This led to low coverage of Ag-Sn. Therefore, the alloy was electrodeposited at the same potential on the activated carbon cloth. Although the electrodeposited Ag-Sn amount was increased, the coverage remained insufficient. Therefore, we employed pulse electrodeposition.

The pulse electrodeposition method was used at different pulse on/off ratios of 2:1, 1:1, and 1:2. The samples deposited with a 2:1 ratio showed the highest catalyst loading. Then the pulse on/off times of 2 s / 1 s, 1 s / 0.5 s, 0.5 s/ 0.25 s, 0.25 s / 0.125 ms, 0.005 s / 0.0025 s, 0.0025 ms / 0.0012 ms, were chosen for the electrodeposition. The potential during the pulse "on" period was set at -0.65 V vs. Ag/AgCl. After the deposition for a total duration of 3 hours, the samples were rinsed with DI water and left to dry in air. The Ag3Sn catalyst that formed on the activated carbon cloth (ACC) will be referred to as Ag3Sn/ACC in this paper.

3.5.4 Physicochemical characterization

To study the coating deposition on the activated carbon cloth surface, SEM (TESCAN VEGA3) was used to take microscopic images at different magnifications and the chemical composition of different samples was studied by EDS. The crystallographic structure of the synthesized coating was studied by XRD (PANalytical X'Pert Pro). The average crystallite size of the deposited films was estimated from the broadening of the main XRD peaks using the Scherrer equation, with Cu Kα radiation.

3.5.5 Electrochemical measurements

A two-compartment cell was used in which a Nafion membrane separated the anode (platinum mesh) from the cathode (Ag_3Sn/ACC). A Hg/HgO electrode was used as the reference electrode. The measured potentials were reported vs. reversible hydrogen electrode (RHE) using the following formula: E_{RHE} = EHg/HgO + (0.059 pH) + 0.098.

Prior to the electrochemical tests, a piece of Nafion membrane (2 × 2 cm^2) was activated by the following procedure. First, it was boiled for one hour in Milli-Q water containing 3% vol/vol H_2O_2. Then it was boiled again for one hour in 1.2 M H_2SO_4. Then it was rinsed with water and boiled in fresh Milli-Q water for another hour.

Two different electrolytes were used. 30 ml of a neutral solution (0.5 M K_2SO_4, pH = 7) and a basic solution (2 M KOH, pH = 13.5) were prepared to evaluate NRR activity in aqueous media. To introduce pure N_2 gas into the electrochemical cell, N_2 gas was first purged through a 500 ml 1 M H_2SO_4 solution to remove NH_3 traces, followed by a 10 ml trap containing 1 M $KMnO_4$ + 1 M KOH to eliminate NO_x species. The last trap before introducing the gas into the electrochemical cell was 10 ml of the same solution that was used as the electrolyte. Moreover, after the electrochemical cell, 5 ml of 0.1 M H_2SO_4 solution was also placed to catch the NH_3 gas that escaped the electrochemical cell. Before applying a potential, the system was purged with N_2 for one hour. The electrochemical tests were done by applying different constant potentials of -0.2, -0.4, -0.6, -0.8, and -1 V vs. RHE for 18 hours while an N_2 flow rate of 20 ml min^{-1} was passed through the traps and purged into the electrochemical cell. After the test, the amount of produced NH_3 was measured as described later.

Different control tests were performed to verify the source of the produced NH_3. The first was to use the same electrode without applying any potential while the electrochemical cell was purged with either N_2 or Ar gas during 18 hours and measuring the NH_3 amount in the cell afterward. The second control tests consisted of applying a given electrode potential but by replacing N_2 with Ar (Air Liquide, 99.999%). The third control test consisted of using an activated carbon cloth (ACC) electrode instead of the Ag_3Sn/ACC catalyst. The electrolysis tests were performed for long periods (18 hours). This results in higher concentrations of produced NH_3 and easier detection and quantification.

3.5.6 Ammonia measurement

For the 2 M KOH solution, the indophenol blue method was used. Following the study [139], 10 mL of the electrolyte after the NRR test was extracted, and 0.4 mL of a solution containing 1 g of phenol in 10 mL of ethanol was added. Then, 1 ml of a solution containing 0.1 g of sodium hydroxide, 2 ml of sodium hypochlorite, and 2 g of sodium citrate dihydrate in 10 ml water were also added to the above solution. Then 0.4 ml of 0.5 wt% $C_5FeN_6Na_2O$ was added. Adding the above solutions turned the electrolyte greener for the solutions that had a higher amount of NH_4. The solution was kept in a dark place for 2 hours for color formation. Then, the absorbance of the solution was recorded at 655 nm using a UV-Vis spectrophotometer (Agilent Cary 60).

For the 0.1 M H_2SO_4 trap and the 0.5 M K_2SO_4 solution, the salicylate method was used [126]. In this method, 2 ml of the electrolyte was removed from the electrochemical cell and mixed with 2

ml of 1 M NaOH solution containing 5 wt% salicylic acid and 5 wt% sodium citrate. Subsequently, 1 ml of 0.05 M NaClO and 0.2 ml of 1 wt% $C_5FeN_6Na_2O$ were added to the solution and stored in a vial for 2 hours in a dark place. The absorbance of the UV-Vis spectrum at 655 nm was then measured.

The calibration curve was obtained by preparing 0.5, 1, 2, and 3 µg/ml NH4 solutions, (equals to 27.7, 55.4, and 110.8, and 166.3 µM NH4 dissolved in the corresponding electrolyte). Their absorbance was measured at a wavelength of 655 nm. By measuring the absorbance of these samples at 655 nm, a linear relationship between absorbance and concentration was established. In this way, the unknown NH_3 amount of a solution was estimated using the calibration curve. Using the slope of the calibration curves, the detection limit for each of the calibration curves with a confidence level of 95% was calculated based on the following formula, where SD is the standard deviation: Detection limit = 3.3 SD / Slope.

3.5.7 Density functional theory

GPAW 22.8.0, a Python code based on the projector-augmented wave method was used for DFT calculations [140]. The electronic interactions were described with the Bayesian error estimation functional with van der Waals correlation (BEEF-vdW) to accurately calculate adsorption free energies [141]. The ionic cores were described with pseudopotentials derived from the projector augmented wave (PAW) approach supplied with GPAW [142]. The bulk structures were cell-optimized to calculate the lattice parameters with a 700 eV plane-wave cutoff and the first Brillouin zone was sampled with Monkhorst-Pack 8 × 8 × 8 k-point grids. The calculated lattice parameters for Ag3Sn are a = 4.85, b = 6.07 and c = 5.26 Å which are in good agreement with the experimentally reported a = 4.78 b = 5.96 and c = 5.18 Å [143]. The optimized orthorhombic (Pmmn space group) unit cell of Ag3Sn was used to construct the (001) surface of the slab with four atomic layers. Periodic images were separated by 15 Å of vacuum in the direction perpendicular to the surface. To aid SCF convergence, the occupation of Kohn–Sham eigenstates was smeared by the Fermi–Dirac function with a width of 0.1 eV, and all energies were extrapolated to kBT = 0 eV. Monkhorst–Pack 3 × 3 × 1 k-point sampling was used for surfaces with plane-wave cutoff similar to bulk geometry-optimization calculations and a refined 9×9×1 grid was used for electronic structure and DOS calculations. The geometrical arrangement of the top two layers along with the adsorbates was optimized, with the two bottom layers fixed at their bulk positions. All structural optimizations were considered to be converged when the maximum

force on all movable atoms fell below 0.05 eVÅ−1. The Gibbs free energy of NRR intermediates and gas phase molecules were calculated by adding corrections to the DFT calculated electronic energies

$$G = E_{DFT} + ZPE + \int C_p dT - TS \qquad (1)$$

where E_{DFT} is electronic energy calculated by DFT. The zero-point energy (ZPE) was calculated by vibrational frequency analysis under the harmonic approximation and entropy (S) corrections were calculated using the ASE Thermochemistry package with the ideal gas and harmonic limit approximations at T = 298.15 K and P = 1 atm [144]. The ZPE and S values for gas-phase N_2, H_2 and NH_3 molecules were taken from the NIST web database. Finally, the adsorption free energy of each intermediate was calculated using the equation:

$$\Delta G_{*NxHy} = G_{*NxHy} - \frac{x}{2} GN_2 - \frac{y}{2} GH_2 - G_* \qquad (2)$$

The asterisk * denotes the electrocatalyst surface and x and y correspond to the number of nitrogen and hydrogen in the adsorbed intermediate, respectively. The theoretical overpotential ($\eta_{theoretical}$) for the NRR was calculated as:

$$\eta_{theoretical} = U_{limiting} - U_{equilibrium} \qquad (3)$$

where $U_{equilibrium}$ is the equilibrium potential of the N_2 reduction (0.06 V vs. RHE) and the limiting potential ($U_{limiting}$) is calculated via:

$$U_{limiting} = -{\Delta G_{max}}/{e} \qquad (4)$$

where ΔG_{max} is the maximum free energy change for a proton-electron transfer step along the NRR pathway.

3.5.8 NRR Mechanisms

The NRR can proceed via dissociative or associative pathways. In the dissociative pathway, the N≡N bond is cleaved in the initial step, and nitrogen adatoms (N) are hydrogenated to form NH_3. However, this pathway is plagued with high-energy barriers for the cleavage of the strong N≡N bond and is therefore not feasible under mild reaction conditions [145,146]. As a result, the associative mechanism is the dominant route under ambient conditions. The associative pathway is further classified into three pathways: distal, alternating, and enzymatic pathways as depicted in Figure 3.21.

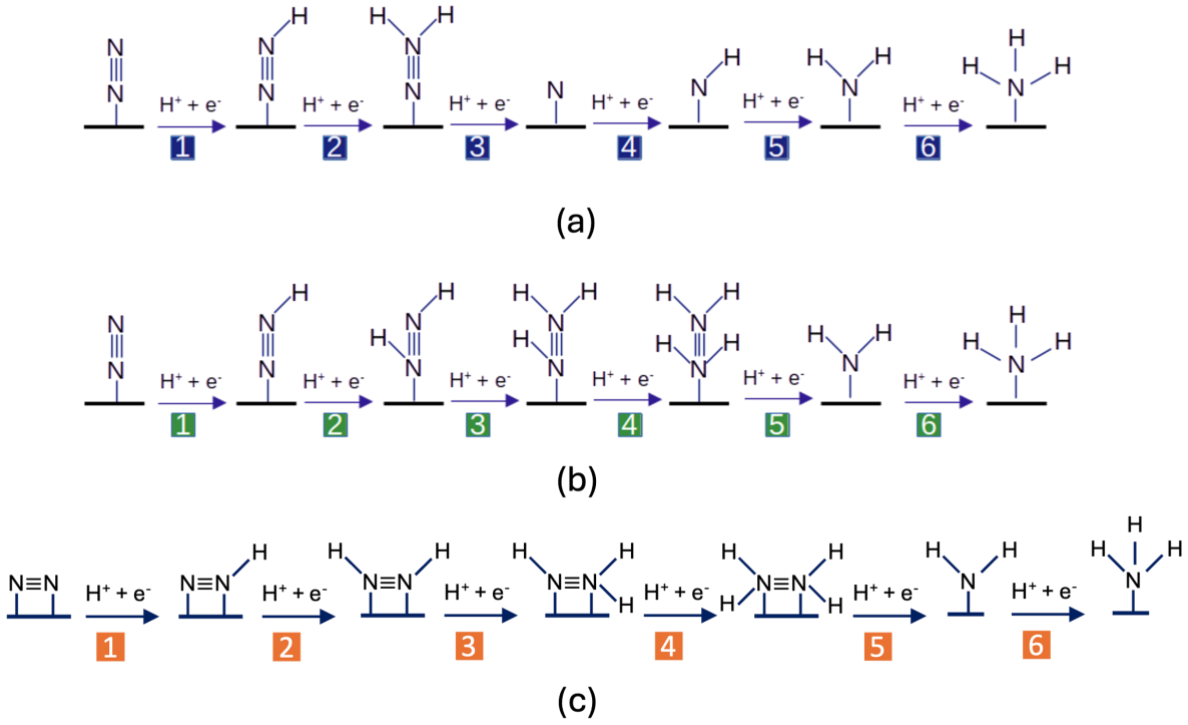


Figure 3.21 NRR associative mechanisms.

(a) distal, (b) alternating and (c) enzymatic. The hydrogenation sequence is shown by numbers.

The main difference between these pathways lies in the adsorption configuration of N_2 on the electrocatalyst surface. In both the distal and alternating pathways, N_2 adsorbs in an end-on configuration, where only one nitrogen atom is directly bonded to the surface. In contrast, the enzymatic pathway involves a side-on configuration, where both nitrogen atoms are simultaneously bonded to the catalyst surface. Previous studies have shown that the distal or the alternating pathways are the most favorable pathways for various groups of electrocatalysts, therefore, we consider the distal and alternating pathway in our calculations [147,148].

4 SONOELECTROCHEMICAL PATHWAY TO AMMONIA SYNTHESIS

Ultrasound-driven nitrogen oxidation: a sonoelectrochemical pathway to ammonia synthesis boosted by contact-electro-catalysis

Oxydation de l'azote induite par ultrasons : une voie sonoelectrochimique vers la synthèse d'ammoniac stimulée par la contact-électrocatalyse

Authors:

Arash Toghraei, Daniel Guay

Institut National de la Recherche scientifique (INRS), Centre Énergie, Matériaux et Télécommunications, Varennes, QC J3X 1P7, Canada

Contribution of authors:

Arash Toghraei developed the process, conducted the experimental tests, and prepared the first draft of the manuscript. Professor Daniel Guay supervised the project and handled the editing and revisions.

Ultrasound activates N_2, forming reactive NO_2^- and NO_3^- intermediates that are electrochemically reduced to NH_3 within a single system. Integrating ultrasound with contact-electro-catalysis significantly enhances N_2 activation and NH_3 yield, offering a simple hybrid pathway for sustainable NH_3 synthesis.

Ammonia (NH_3), essential for fertilizers, is mainly produced by the Haber-Bosch process, which emits approximately 1.5–1.6 kg of CO_2 per kg of NH_3 synthesized [149]. A promising alternative to this method is the electrochemical nitrogen (N_2) reduction reaction (NRR). A critical limitation of NRR in aqueous solutions is the difficulty of activating inert N_2 molecules [150]. To address this issue, researchers have used plasma treatment on N_2 gas to produce NO_2^- and NO_3^- species, which can be more readily reduced electrochemically to NH_3 [54]. However, the process is limited by high-energy consumption, the complexity of plasma infrastructure, and difficulties in controlling the process [151].

Ultrasound treatment is a simpler alternative for generating NO_2^- and NO_3^- species in aqueous systems. During sonochemical reactions in aqueous solutions, cavitation and the production of reactive radicals can convert N_2 gas to NO_2^- and NO_3^- [152].

Unlike plasma-assisted NO_2^- and NO_3^- production, which requires dedicated high-energy setups, ultrasound-based generation can be integrated into existing ultrasound processes (such as industrial or cleaning applications), allowing otherwise unused energy to contribute to NO_2^- and NO_3^- formation.

Recent studies show that introducing contact-electro-catalysts (CEC) can enhance sonochemical reaction rates. Materials such as polytetrafluoroethylene (PTFE), and fluorinated ethylene propylene (FEP), are triboelectric and can be mechanically polarized. Under ultrasonic excitation, these materials promote interfacial charge separation and electron transfer, thereby enhancing the generation of reactive oxygen species (ROS). [153] These reactive radicals can then interact with other substances in the solution, initiating or accelerating chemical reactions.

Although the role of CEC in ROS generation is widely accepted, the exact mechanism remains unclear. This uncertainty partly arises from the coexistence of sonochemical and mechanochemical effects during CEC, making it difficult to isolate their individual roles. A recent study suggests that while friction-induced mechanochemical processes generate electrons on the catalyst surface, only a very small fraction (less than 0.1%) have sufficient

energy to initiate ROS formation, and sonochemical ultrasound cavitation is proposed to activate these electrons. [154]

CEC can be used to produce NH_3. In a recent study, PTFE was used for NH_3 production with N_2 continuously purged into the solution. [118] In this study, NH_3 was generated without applying any external potential or using an electrochemical cell. NH_3 Generation relied solely on on the CEC effect of PTFE, which was activated by ultrasonic agitation. The proposed mechanism involves generating OH• and H• radicals via contact electrification. Then, OH• radicals combine to form H_2O_2, and H• radicals react with N_2 to produce NH_3. However, the observed NH_3 yield was limited, likely due to the competitive oxidation of N_2 into NO_2^- AND NO_3^- species. Previous research has demonstrated that CEC, such as PTFE, can generate nitric acid and other nitrogen oxides under similar conditions. [119] These papers together, reflect the coexistence of oxidative and reductive microenvironments during the process. This dual reactivity makes it difficult to favour the selective formation of NH_3, highlighting the need for a more controlled system to drive the reaction toward NH_3 production.

In the present study, we propose a novel strategy that employs sonochemical activation of N_2 for its subsequent electrochemical reduction to NH_3 on a copper foil. This strategy enhances performance by integrating CEC with electrocatalysis under ultrasound treatment. This hybrid method enables N_2 activation via CEC, and the generated NO_2^- and NO_3^- species undergo further reduction to NH_3 in an electrochemical reaction. We systematically examined the key parameters, including the PTFE amount and the type of purging gas, and their impact on reaction performance.

A single-compartment electrochemical cell opened to air was positioned in a conventional ultrasonic bath using a custom-designed holder and was continuously purged with various gases (N_2, Ar and air). The electrolyte consisted of 30 mL of 0.5 M Na_2SO_4, in which different amounts of PTFE were tested. The cathode was a 1 × 1 cm^2 copper foil, used on both sides, and the anode was a 2 × 2 cm^2 platinum mesh. During each experiment, the current density was maintained at −10 mA cm^{-2}. Reproducibility was evaluated by repeating representative experiments three times under identical conditions. Additional experimental details are provided in the Supporting Information.

To establish optimal operating conditions for subsequent NH_3 synthesis, we conducted a systematic series of control experiments to verify system cleanliness, delineate the

respective contributions of ultrasound and PTFE loading to NO_x generation, and identify parameters that maximize N_2 activation.

Figure 4.1 presents the calibration curves used to quantify NO_2^- and NH_4^+. The cleanliness of the system was verified by purging N_2, Ar, and air separately into the electrolyte for 1 h each without applying any potential. Under these conditions, the concentrations of NO_2^- and NH_4^+ remained below the detection limit (results not shown; baseline signal), confirming that neither the purging gases nor the electrochemical cell introduced measurable contamination.

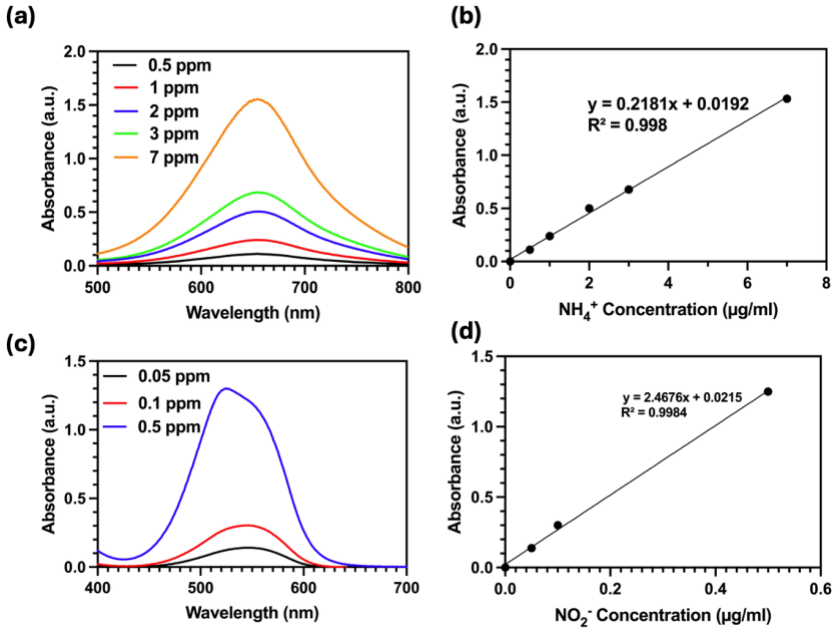


Figure 4.1. (a) UV-Vis spectra of various 0.5 M Na_2SO_4 solutions containing different NH_4^+ concentrations, prepared by dissolving NH_4Cl in 0.5 M Na_2SO_4; (b) calibration curve for NH_4^+ concentration based on peak intensity at 655 nm evaluated in (a); (c) UV-Vis spectra of various 0.5 M Na_2SO_4 solutions containing different NO_2^- concentrations, prepared by dissolving KNO_2 in 0.5 M Na_2SO_4; (d) calibration curve for NO_2^- concentration based on peak intensity at 540 nm evaluated in (c).

The influence of sonication and PTFE loading on N_2 activation was initially evaluated by measuring NO_2^- formation in a 0.5 M Na_2SO_4 electrolyte. Sonication was carried out for 1 h under a 50:50 N_2/Ar gas mixture in open-air conditions, with different amounts of PTFE added to the electrolyte. Argon was included because it has been suggested to enhance N_2 activation due to its higher heat capacity, which increases bubble temperatures during cavitation and thereby promotes radical formation and NO_x^- generation. [108] In the

presence of PTFE, this temperature increase may also help overcome surface energy barriers for electron transfer. [113] No electrochemical potential was applied during these experiments. NO_2^- concentrations were quantified using the calibration curve shown in Figure 4.1, and the corresponding results are presented in Figure 4.2.

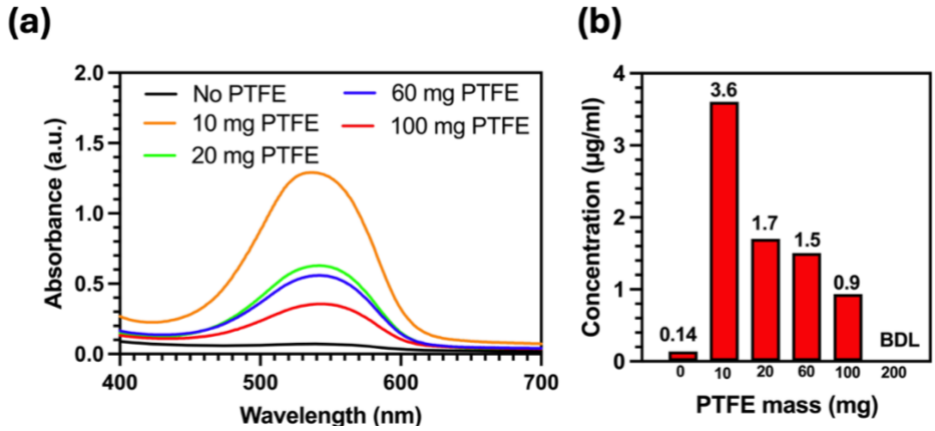


Figure 4.2. (a) UV-vis spectra and (b) the corresponding bar graph showing the amount of NO_2^- formed after 1 h of ultrasonic treatment with different amounts of PTFE in the solution. A 50:50 mixture of N_2 and Ar was continuously purged into a 30 mL solution of 0.5 M Na_2SO_4 during ultrasonic treatment. Each sample was diluted 7x with a 0.5 M Na_2SO_4 solution.

Under sonication without PTFE, the NO_2^- concentration reached 0.14 µg mL^{-1}, in agreement with literature reports of similar NO_2^- formation under comparable ultrasonic. [108,152] Although the underlying mechanisms are not yet fully understood, this behaviour is generally attributed to the extreme localized temperatures and pressures generated during acoustic cavitation.

Adding 10 mg of PTFE increased NO_2^- production by approximately 26-fold, reaching 3.6 µg mL^{-1} (Figure 4.2). This substantial enhancement may arise from the increased generation of reactive oxygen species (ROS) during the contact electrification that occurs when water interacts with PTFE. [155] These radicals can oxidize N_2, leading to the formation of NO_2^- (and NO_3^-) species. [156] However, further increasing the amount of PTFE reduced NO_2^- production. When the PTFE loading was increased from 10 mg to 20 mg, NO_2^- decreased by half, and it continued to decline to 0.9 µg mL^{-1} at 100 mg. Notably, at 200 mg of PTFE, NO_2^- was no longer detectable. A similar inverse trend at high PTFE loadings has been observed in other systems, such as PTFE-assisted H_2O_2 generation. [113]

In these experiments, it was observed that PTFE accumulates at the air-electrolyte interface, forming an air-PTFE-electrolyte interface. This could lead electron accumulation

at the PTFE-electrolyte interface, altering interfacial charge dynamics and ultimately suppressing the radical-driven reactions required for NO_x^- formation. [155] Although surfactants could improve PTFE dispersion and mitigate charge buildup, none was used here to avoid introducing additional variables that might affect the chemistry. In addition, the accumulation of PTFE at the surface of the electrolyte may hindered the diffusion of atmospheric O_2 into the electrolyte, thereby contributing to the reduced NO_2^- production observed at higher PTFE loadings.

Based on these observations, the optimal condition for maximizing N_2 activation, and thus enabling efficient downstream NH_3 production, was determined to be 10 mg of PTFE in 30 mL of 0.5 M Na_2SO_4. This PTFE amount was used for all subsequent experiments.

Next, electrochemical reduction was carried out in the single-compartment electrochemical cell opened to air under simultaneous ultrasound treatment. A constant current density of $-10\,mA\,cm^{-2}$ was applied, and a continuous flow of a 50:50 N_2/Ar gas mixture was maintained throughout the experiment. Copper was selected as the cathode because it is a well-established catalyst for reducing NO_3^- to NH_3. [157] Although its activity can be enhanced through strategies such as alloying, catalyst modification was not the focus of this study. Importantly, the chosen electrode material also needed to exhibit strong mechanical and chemical stability to withstand the intense conditions imposed by ultrasonic irradiation.

Figures Figure 4.3 andFigure 4.4 show that the amount of NH_3 produced on the Cu foil at $-10\,mA\,cm^{-2}$ remained below the detection limit when ultrasound was not applied. Likewise, replacing the N_2/Ar gas mixture with pure N_2 as the purging gas also resulted in undetectable NH_3 formation (results not shown; baseline sign al). These results are expected, given the well-known challenges of electrochemical N_2 reduction in aqueous media, where the hydrogen evolution reaction (HER) strongly competes with NRR and copper exhibits intrinsically low activity toward NH_3 production [158].

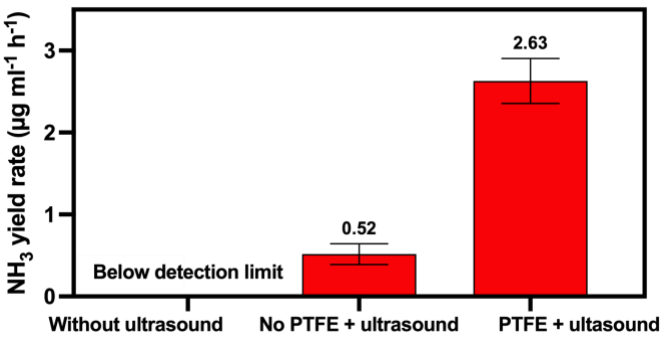


Figure 4.3. NH_3 yield rate under different conditions.

Electrolysis was conducted in a single-compartment electrochemical cell open to air for 1 h at −10 mA cm^{-2} on a Cu cathode in 30 mL of 0.5 M Na_2SO_4 with 50:50 N_2/Ar purging.

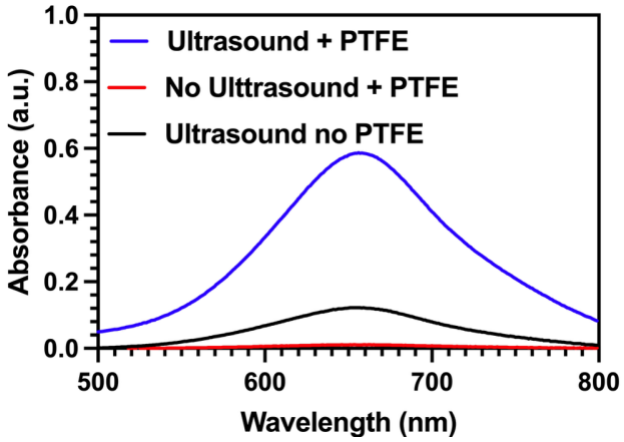


Figure 4.4. UV-Vis spectra corresponding to the produced NH_3 under different conditions.

With and without ultrasound and 10 mg PTFE. Electrolysis was conducted for 1 h at -10 mA/cm^2 on the Cu cathode in 30 mL of 0.5 M Na_2SO_4. A 50:50 mixture of N_2 and Ar was continuously purged into the solution during the ultrasonic treatment. The amount of NH_3 for the "no ultrasound", "ultrasound no PTFE", and "ultrasound + PTFE" was below the detection limit, 0.47, and 2.57 μg/mL.

An NH_3 production rate of 0.52 μg mL^{-1} h^{-1}, corresponding to 15.6 μg h^{-1}, was obtained during electrochemical reduction without PTFE when ultrasonic treatment was applied (Figure 1). To verify the origin of the detected NH_3, a control experiment was conducted in which the cell was purged with Ar while maintaining a current density of −10 mA cm^{-2} under ultrasound. In this case, NH_3 remained below the detection limit (result not shown; signal at baseline), confirming that the measured NH_3 originated from N_2 introduced into the solution.

At −10 mA cm^{-2}, applying ultrasonic treatment in the presence of 10 mg of PTFE as a CEC increased the NH_3 production rate five-fold, reaching 2.63 μg mL^{-1} h^{-1} (78.9 μg h^{-1})

(Figure 4.3). This substantial enhancement is consistent with the pronounced increase in NO_2^- formation observed upon adding PTFE to the electrolyte (Figure 4.2), suggesting that PTFE plays a key role in facilitating N_2 activation and generating a larger pool of reducible nitrogen intermediates that can be converted to NH_3 at the cathode. Post-reaction analysis showed that the NO_2^- concentration decreased to 0.02 μg mL^{-1} (Figure 4.5), indicating that nearly all NO_2^- was consumed during the electrochemical process.

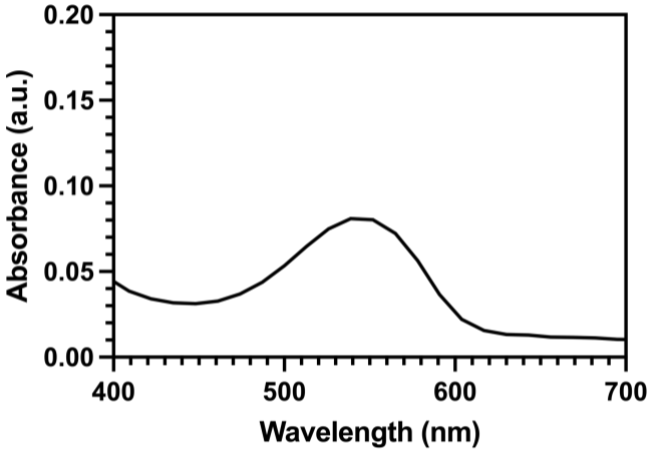


Figure 4.5. UV–vis spectra corresponding to 0.02 μg/mL of NO_2^- detected after 1 h of contact-electro-catalysis N_2 activation coupled with electrochemical reaction at -10 mA/cm^2 on Cu foil. A 50:50 mixture of N_2 and Ar was continuously purged into 30 mL of 0.5 M Na_2SO_4 solution containing 10 mg of PTFE under ultrasonic treatment. The graph shows the consumption of activated N_2 by the electrochemical reduction.

Figure 4.6 illustrate the quantity of NH_3 generated over a 2 h period, with sampling intervals at 30 min, 1 h, and 2 h. The data demonstrate a generally linear relationship, indicating continuous NH_3 production during the measurement period.

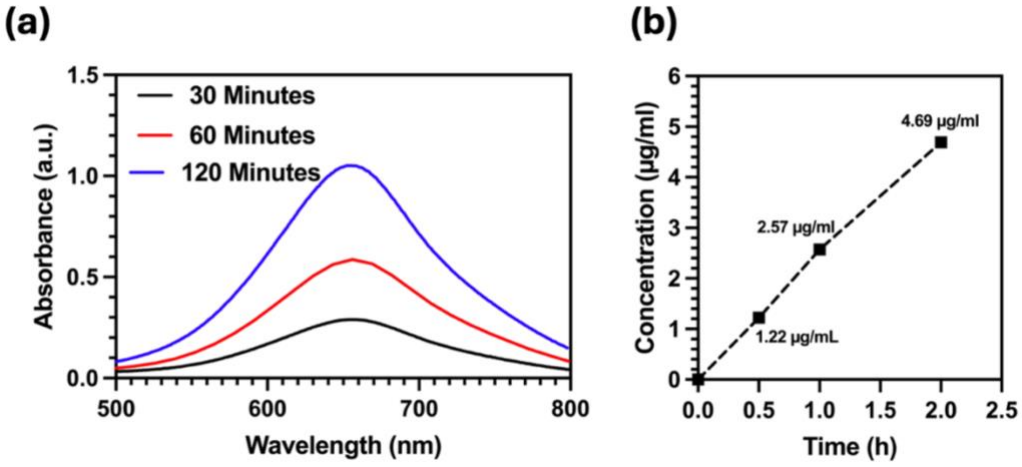


Figure 4.6. (a) The UV-vis spectra and (b) the corresponding NH_3 concentration–time plot illustrating the amount of NH_3 produced over 2 hours. A current density of -10 mA/cm^2 was applied. The electrolyte was 30 ml of 0.5 M Na_2SO_4, with 10 mg PTFE. A 50:50 mixture of N_2 and Ar was continuously purged into the solution during the ultrasonic treatment. The amounts of NH_3 after 30 min, 60 min, and 120 min were 1.22, 2.57, and 4.69 µg/mL, respectively.

To gain further insight into the pathway for NH_3 formation, we examined whether NH_3 could be generated solely through CEC in the absence of an applied potential on the Cu electrode. For this purpose, a 50:50 N_2/Ar mixture was bubbled into a 0.5 M Na_2SO_4 solution containing 10 mg of PTFE, and the system was subjected to ultrasonic treatment for 1 h without applying any current. Under these conditions, no detectable NH_3 was produced, confirming that CEC alone does not lead to NH_3 formation (results not shown; signal at baseline).

We then assessed whether CEC could oxidize NH_3. As shown in Figure 4.7, sonicating a 1 µg mL^{-1} NH_3 solution for 1 h caused only a slight decrease to 0.87 µg mL^{-1}, an effect observed solely in the presence of PTFE, indicating minor radical-driven NH_3 oxidation. This oxidation is minimal and could likely be further mitigated through adjustments to electrolyte or cell conditions, which were beyond the scope of this study.

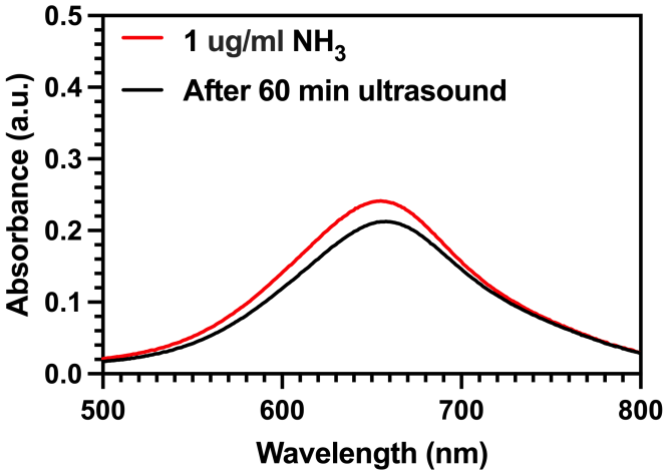


Figure 4.7. UV-vis spectra showing the effect of contact-electro-catalyst on the NH_3 amount dissolved in 0.5 M Na_2SO_4 after 60 min of ultrasound treatment in the presence of 10 mg PTFE. A 50:50 mixture of N_2 and Ar was continuously purged into the solution during the ultrasonic treatment. The amount of NH_3 decreased from 1 µg/mL to 0.87 µg/mL after the test.

Because the concurrent influence of ultrasound, PTFE, and electrochemical bias complicates mechanistic interpretation, and in light of literature reports showing that

ultrasound can oxidize N_2 to NO_3^- [119] and that NO_3^- can subsequently be reduced to NH_3 [159] on Cu, we quantified both NO_2^- and NO_3^- in the following experiments.

To disentangle the individual contributions of CEC-driven sonochemistry and electrochemical reduction, we first exposed the electrolyte containing 10 mg PTFE to ultrasound alone, without applying any potential, and quantified the resulting formation of oxidized nitrogen species. Under these conditions, the NO_2^- and NO_3^- production rate reached 3.50 and 6.08 $\mu g\,mL^{-1}\,h^{-1}$, respectively after 1 h of sonication in a 50:50 N_2/Ar atmosphere (Figure 4.8). These results confirm that ROS generated during sonication oxidize N_2 not only to NO_2^- but also to NO_3^-.

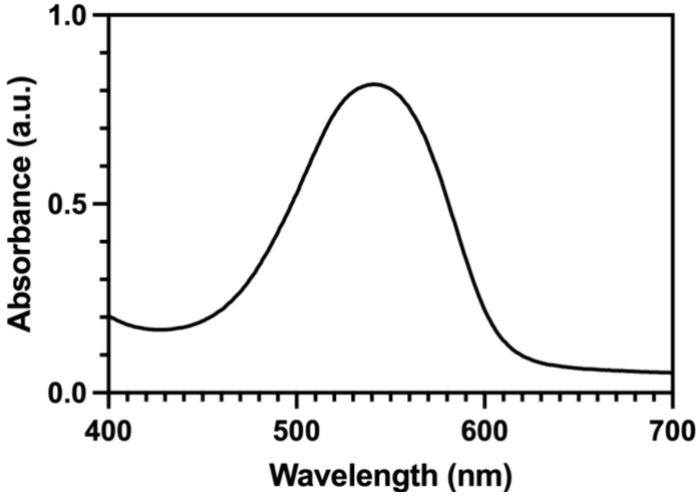


Figure 4.8. UV-vis spectra of the electrolyte reacted with Zn powder to reduce NO_3^- to NO_2^-. The amount of NO_2^- (9.58 µg/mL), subtracted from NO_2^- amount before reacting with Zn, (3.5 µg/mL) shows the amount of NO_3^- to be around 6.08 µg/mL after 1 h of ultrasonic treatment with 10 mg PTFE. A 50:50 mixture of N_2 and Ar was continuously purged into a 30 mL solution of 0.5 M Na_2SO_4 during the ultrasonic treatment. The solution was diluted 30x with 0.5 M Na_2SO_4 before the measurement.

Subsequently, electrochemical reduction was performed for 1 h at $-10\,mA\,cm^{-2}$ using this ultrasound-pretreated electrolyte, but without ultrasound. Under these decoupled conditions, the NH_3 production rate reached 2.89 $\mu g\,mL^{-1}\,h^{-1}$, closely matching the value obtained when ultrasound and electrochemical bias were applied simultaneously (2.63 $\mu g\,mL^{-1}\,h^{-1}$; Figure 4.9)

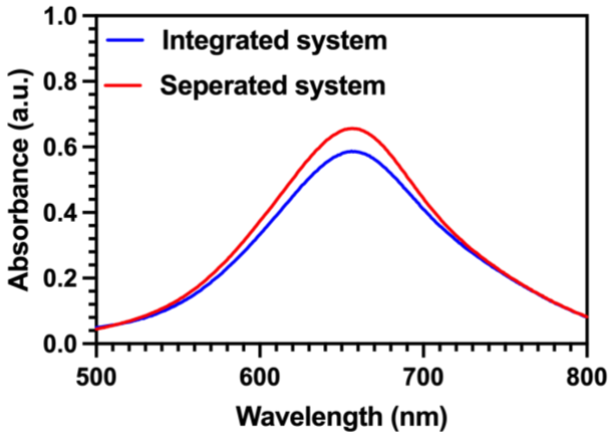


Figure 4.9 UV–Vis spectra corresponding to the produced NH_3 in the integrated and separated systems. In the separated system, a 50:50 mixture of N_2 and Ar was first purged into 30 mL of 0.5 M Na_2SO_4 under sonication in the presence of 10 mg PTFE, leading to the formation of NO_3^- and NO_2^- in the solution. The obtained solution was then used for electrochemical reduction at −10 mA/cm on a Cu cathode to produce NH_3. In the integrated system, NO_x formation and their reduction to NH_3 on Cu occurred simultaneously.

Together, these results support a mechanistic sequence in which CEC-assisted sonochemistry activates N_2 to NO_2^- and NO_3^- (NO_x) species, and the applied electrochemical potential subsequently reduces these intermediates to NH_3 (Figure 4.10).

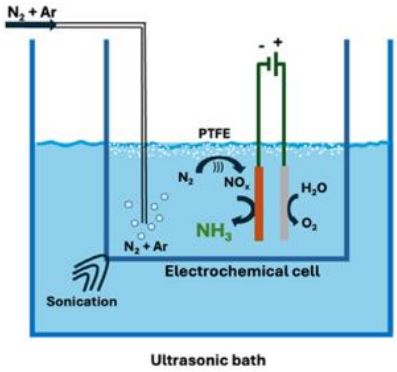


Figure 4.10 Schematic of the system and proposed mechanism for NH_3 production.

The Faradaic efficiency (FE%) for this decoupled process was 4.9%, nearly identical to the FE% of the coupled process, which was 4.33%.

We probed the purging-gas effect by comparing N_2/Ar, N_2, air, and air/Ar (Figure 4.11).

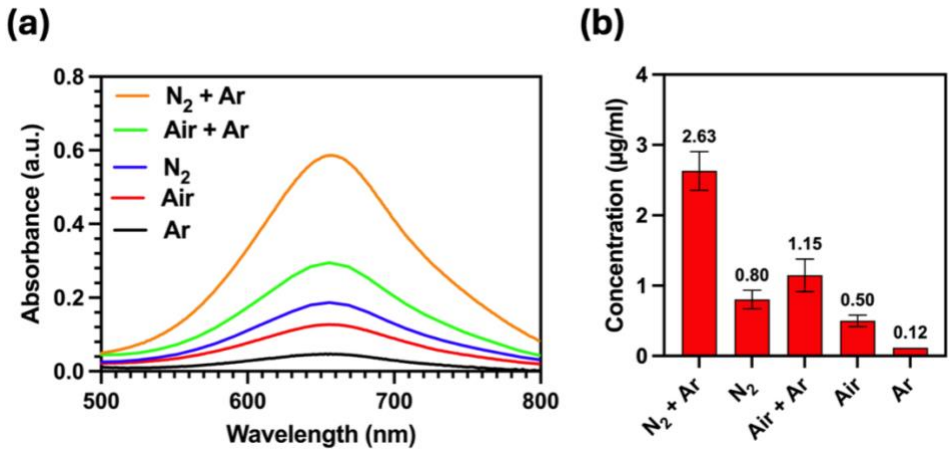


Figure 4.11. (a) UV-vis spectra and (b) corresponding bar graph, showing the amount of NH_3 produced after 1 h at a current density of -10 mA/cm² for the Cu cathode in 0.5 M Na_2SO_4 with ultrasound. The gases were mixed in a 50:50 ratio, and 10 mg of PTFE were added to all solutions.

The N_2/Ar mixture gave the highest NH_3 rate (2.63 µg mL^{-1} h^{-1}), whereas pure N_2 was much lower (0.8 µg mL^{-1} h^{-1}). This is consistent with Ar-enhanced acoustic cavitation: Ar's high molar mass and low thermal conductivity favor hotter, more adiabatic bubble collapse, increasing radical flux (•OH/•H) and promoting sonochemical activation of N_2 to NO_x^- intermediates that are subsequently reduced at the cathode to NH_3. Using air further decreased NH_3 (0.50 µg mL^{-1} h^{-1}) due to lower N_2 partial pressure, while adding Ar to air raised the rate (1.15 µg mL^{-1} h^{-1}), reinforcing the beneficial cavitation role of Ar. A pure Ar control (PTFE present, −10 mA cm^{-2}) yielded only 0.12 µg mL^{-1} h^{-1}, confirming that nitrogen-derived NO_x^- formed during CEC is required and that NH_3 arises from a two-step sequence: (i) Ar-amplified sonochemical N_2 activation to NO_2^-/NO_3^-, followed by (ii) electrochemical reduction of these intermediates to NH_3 (see Note S1).

To eliminate any influence of O_2 generated at the anode in the single-compartment cell, as well as any O_2 introduced through atmospheric contact in the open-cell configuration, we repeated the experiments in an H-type setup, where the anolyte and catholyte are separated by a membrane, and O_2 from the atmosphere can be minimized, while all other conditions, including 10 mg of PTFE at the cathode, were kept identical. The corresponding NH_3 UV–vis results are presented in Figure 4.12.

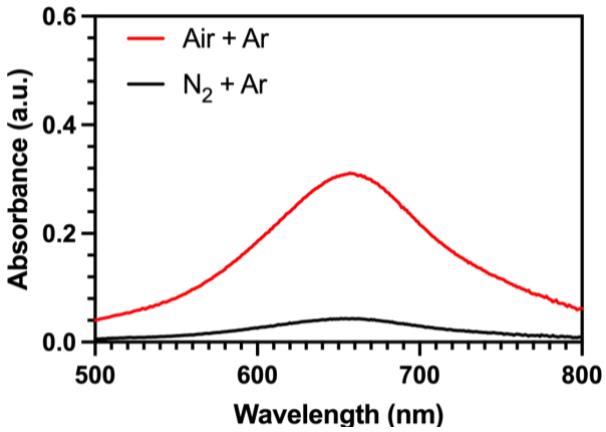


Figure 4.12 UV-vis spectra and showing the amount of NH_3 produced after 1 h in an H-type cell at a current density of -10 mA/cm² for the Cu cathode in 0.5 M Na_2SO_4 with ultrasound. The gases were mixed in a 50:50 ratio, and 10 mg of PTFE were added to the cathode chamber.

In agreement with our earlier observations and mechanistic hypothesis, purging with a 50:50 N_2/Ar mixture produced almost no NH_3 in the H-type cell (0.10 $\mu g\, mL^{-1}\, h^{-1}$), in sharp contrast to the 2.63 $\mu g\, mL^{-1}\, h^{-1}$ obtained in the single-compartment open-cell configuration. The marked reduction in NO_x^- intermediates when O_2 is excluded from contacting N_2 in the H-type cell, and the corresponding drop in NH_3 yield, reinforces our conclusion that O_2-assisted CEC activation of N_2 is essential for generating the NO_x species subsequently reduced to NH_3.

In conclusion, we demonstrate a new strategy that couples ultrasound-driven cavitation and CEC to activate N_2 and generate reactive NO_2^-/NO_3^- intermediates that can be selectively converted to NH_3 through electrochemical reduction. By harnessing and controlling the radical chemistry produced during CEC, this approach establishes a versatile platform for driving otherwise inaccessible N_2 activation pathways. Looking forward, the ability to decouple and tune the sonochemical and electrochemical steps opens opportunities for designing more efficient, modular processes and for extending this methodology to other difficult small-molecule transformations. This framework sets the stage for next-generation hybrid sonochemical–electrochemical systems capable of converting abundant, inert molecules into value-added products under mild conditions.

The authors gratefully acknowledge financial support from the Fonds de recherche du Québec – Société et culture (FRQSC) and Fonds de recherche du Québec – Nature et Technologies (FRQNT), through the "Programme intersectoriel Audace" (https://doi.org/10.69777/285517) and "Audace Plus - Volet Visée"

(https://doi.org/10.69777/340443). One of us (AT) acknowledge the financial support of the Fonds de recherche du Québec – Nature et Technologies (FRQNT) for PhD B2X scholarship.

Conflicts of interest

There are no conflicts to declare.

Data availability

All data supporting the findings of this study are available within the article and its SI. See DOI:

4.1 Note S1. Production of NH_3 under different purging gases

Different gas mixtures were examined to investigate the effects of Ar addition and dissolved O_2 on the NRR performance in the system. In previous sonochemical studies, conducted without contact-electro-catalysts, Ar purging has been suggested as a strategy to enhance the generation of NO_x^- species [108]. In our case, where 10 mg of PTFE was present in the electrolyte, we also observed a significant increase in the NH_3 production rate in the presence of Ar. As can be seen in Figure 4.11, purging the system with pure N_2, produces around 0.80 µg/ml/h of NH_3. However, purging the electrolyte with a gas mixture of 50:50 N_2 and Ar can produce 2.63 µg/ml/h NH_3, which is around 3.3 times higher than pure N_2. This increase can be attributed to the higher production of NO_x^- species in the presence of Ar which will be further reduced on the cathode surface to produce NH_3. It has been proposed that the increased production of NO_x^- may result from the higher heat ratio of Ar compared to N_2, which raises the temperature of the bubbles during cavitation, intensifying reactive radicals' formation, and thereby enhancing the likelihood of NO_x^- production at elevated temperatures [108]. In the presence of PTFE, the higher temperature of cavitation induced by Ar gas may provide more energy to overcome the energy barriers for electron exchange on the surface of PTFE [155].

When the system was purged with air instead of N_2, the production of NH_3 was decreased by approximately 1.6 times to 0.50 µg/ml/h. The observed difference is likely due to the lower partial pressure of N_2 in air relative to pure N_2. It is noticeable that purging air with Ar at a 50:50 ratio, will increase the NH_3 production rate to 1.15 µg/ml/h, further verifying the positive effect of Ar on NH_3 production rate.

4.2 EXPERIMENTAL SECTION

4.2.1 Materials and reagents

Sodium citrate dihydrate ($C_6H_9Na_3O_9 \cdot 2H_2O$, ≥ 99.0%), polytetrafluoroethylene (PTFE, 6-10 μm), sulfuric acid (H_2SO_4, 95.0–98.0%), sodium hydroxide (NaOH, ≥ 99.99%), and sodium sulfate anhydrous (Na_2SO_4, ≥ 99.0%) were purchased from Fisher Scientific. Sodium nitroferricyanide dihydrate ($C_5FeN_6Na_2O \cdot 2H_2O$, ≥ 99.0%), sodium hypochlorite solution (NaClO, chlorine ≥ 5.0%), ammonium chloride (NH_4Cl, 99.5%), potassium permanganate ($KMnO_4$ ≥ 99.0%), acetone (CH_3COCH_3, ≥ 99.5%), salicylic acid ($C_7H_6O_3$, ≥ 99.0%), potassium nitrite (KNO_2 ≥ 99.0%), and nitrite test kit (Spectroquant) were purchased from Sigma-Aldrich. Milli-Q deionized (DI) water was utilized for both sample rinsing and electrolyte preparation. Ultrapure N_2 and Ar gases (grade 5.0) and Air cylinders were supplied by Air Liquide. A conventional ultrasonic bath (Branson 1800, output: 70 W, 40 kHz) was used. A BioLogic SP-300 potentiostat/galvanostat was used to run the electrochemical tests. UV–Vis measurements were carried out with a Cary 60 spectrophotometer (Agilent Technologies).

4.2.2 System preparation

The electrochemical cell was placed in a conventional ultrasonic bath using a custom holder. The electrochemical cell was continuously purged with different types of gases at a flow rate of 20 mL min^{-1}. The purging gas was purified by passing through a series of gas traps. The first trap contained 500 mL of 1 M H_2SO_4 to remove traces of NH_3. This was followed by a 30 mL trap containing 1 M $KMnO_4$ and 1 M KOH to capture NO_x species. The final trap, placed just before the gas entered the electrochemical cell, contained 20 mL of 0.5 M Na_2SO_4 solution. Each gas was purged into the electrochemical cell for 30 min before starting the experiment.

The electrolyte consisted of 30 mL of 0.5 M Na_2SO_4, with varying amounts of PTFE tested. The cathode was a 1 × 1 cm^2 piece of copper foil used on both sides, and the anode was a 2 × 2 cm^2 platinum mesh. Prior to each experiment, the copper foil cathode was mechanically polished and subsequently cleaned by ultrasonic treatment in acetone for 10 min to ensure a clean surface. A single-compartment electrochemical cell, consisting of a 100 mL beaker filled with 30 mL of electrolyte, was placed in an ultrasonic bath. During each experiment, the current density at the copper cathode was maintained at −10 mA/cm^2. Experiments were conducted under varying conditions to assess the effects of different PTFE concentrations (0, 10, 20, 60, 100, and 200

mg). The effects of the presence or absence of ultrasonic treatment and the composition of the purging gas were investigated. The gas environments included 50:50 mixtures of N_2 + Ar and air + Ar, as well as pure N_2, pure Ar, and pure air. All experiments were run for 1 h. To evaluate stability over time, NH_3 production was measured after 30 min, 1 h, and 2 h during durability testing.

As a control to confirm NH_3 production in a different cell configuration, and in a more controlled gas environment, measurements were taken for one hour at -10 mA cm^{-2} on a copper cathode in a closed H-type cell separated by a Nafion membrane. Each compartment contained 30 mL of electrolyte, and the cell was purged with either N_2 + Ar or Ar + N_2 gas mixtures, and pure Ar. Before electrochemical tests in the H-type cell, a 2 × 2 cm^2 Nafion membrane piece was activated by sequential boiling, first for one hour in Milli-Q water with 3% (v/v) H_2O_2, followed by one hour in 1.2 M H_2SO_4, and a final one-hour boil in fresh Milli-Q water after rinsing.

4.2.3 NH_3, NO_2^-, and NO_3^- measurement and FE% calculation

The salicylate method was used to measure the amount of NH_3 after each test [126]. In this method, 2 ml of electrolyte were removed from the electrochemical cell and mixed with 2 ml of a 1 M NaOH solution containing 5 wt% $C_6H_9Na_3O_9 \cdot 2H_2O$ and $C_7H_6O_3$. Then, 0.2 mL of 1 wt% $C_5FeN_6Na_2O$ and 1 mL of 0.05 M NaClO were added to the mixture. The mixture was stored in a vial in the dark for two hours. After incubation, the absorbance at 655 nm was measured using UV-Vis spectroscopy. A calibration curve was generated using NH_4Cl standards at concentrations of 0.5, 1, 2, 3, and 7 µg/mL, each prepared in a 0.5 M Na_2SO_4 solution. NO_2^- was quantified using a nitrite test kit. First, 35 mg of reagent was added to 3 mL of electrolyte after the experiment. Then, the mixture was incubated in the dark for 10 min to allow color development [53]. For NO_3^- detection, the procedure proposed by Murray et al. was followed. [160] Briefly, 25 mg of Zn powder was added to the solution and shaken 20 times to reduce NO_3^- to NO_2^-. Afterwards, the total NO_2^- concentration (native NO_2^- plus NO_2^- generated from NO_3^-) was measured by the NO_2^- test method that described above. The NO_3^- concentration was determined from the difference between these two measurements. A calibration curve was established by preparing KNO_2 solutions at concentrations of 0.05, 0.5, and 1 µg/mL in 0.5 M Na_2SO_4 and measuring their UV-Vis absorbance at 540 nm. To detect NO_2^- in electrolytes containing different amounts of PTFE, the sample was diluted sevenfold with 0.5 M Na_2SO_4 prior to each measurement.

The Faradaic efficiency was calculated for the separated system, where NO_3^- and NO_2^- were first generated under sonication and the resulting solution was then electrochemically reduced to NH_3. Since both NO_3^- and NO_2^- were present in the electrolyte and contributed to NH_3 formation, and depleted after the reaction, the overall Faradaic efficiency was calculated using a weighted average electron number based on their relative molar contributions.

The reduction reactions require 8 e^- for NO_3^-RR and 6 e^- for NO_2^-RR to NH_3.

From their measured concentrations (6.08 μg mL^{-1} NO_3^- and 3.5 μg mL^{-1} NO_2^- in 30 mL), their molar fractions were first determined. Based on these fractions, the weighted average number of electrons transferred per mole of NH_3 formed was calculated to be:

n_{avg} = 7.12 e^-

The Faradaic efficiency was then calculated using:

$$FE\ (\%) = (n_{avg} \times F \times n_{NH_3}) / Q \times 100$$

where

$_{n}NH_3$ is the number of moles of produced NH_3 (calculated from 2.89 μg mL^{-1} in 30 mL), F is Faraday's constant (96485 C mol^{-1}), and Q is the total charge passed (72 C).

Using these values, the weighted Faradaic efficiency was calculated to be approximately 4.9%.

5 CONCLUSION

The development of the Haber–Bosch process marked the beginning of industrial ammonia production, enabling large-scale fertilizer production that transformed global agriculture. As a result, our planet once estimated to sustain around 4 billion people now supports more than 8 billion. However, this fossil-fuel–dependent process emits large amounts of CO_2 each year, driving the search for alternative routes to ammonia synthesis.

Electrochemical ammonia production from N_2 has emerged as a promising concept, especially when coupled with renewable energy sources. In principle, it allows direct NH_3 generation in an electrochemical cell. However, in aqueous electrolytes, the competing HER dominates, leading to low NH_3 yields. Alloying has been shown to be an effective strategy to improve the electrocatalytic NRR.

Motivated by reports of NRR activity for Ag and Sn, and their low HER activity and the prospect of p–d orbital hybridization, we synthesized Ag_3Sn alloy via pulse electrodeposition on activated carbon cloth. However, contrary to expectations, no genuine NRR activity was observed in aqueous solutions. In 2 M KOH, 18-hour electrolysis across a range of potentials yielded no detectable NH_3. In 0.5 M K_2SO_4, owing to a better NH_3 detection limit, NH_3 was detected, particularly at potentials more negative than –0.6 V vs. RHE, but identical amounts were also observed during Ar control tests with freshly prepared electrodes. This indicated that the detected NH_3 originated from N-species in the electrochemical system rather than electrochemical N_2 reduction. DFT calculations supported this conclusion: although Ag_3Sn showed a lower limiting potential for NRR compared to pure Ag or Sn, the required overpotentials remained prohibitively large. So overall, the anticipated NRR activity of Ag_3Sn was not confirmed.

Recognizing the fundamental difficulty of activating N_2 solely by electrochemical reduction in aqueous media, we introduced an additional activation pathway. We designed a hybrid approach combining ultrasound with electrocatalysis and further boosted the activation of N_2 by adding PTFE as contact-electro-catalyst under sonication. This method generates reactive nitrogen species prior to electrochemical reduction. To evaluate the degree of activation, we measured NO_2^- formation under continuous N_2 + Ar (50:50) purging without applied potential. Sonication alone produced 4.2 μg h^{-1} of NO_2^-, while PTFE presence increased it to 108 μg h^{-1}, showing its significant role in N_2 activation.

The enhanced activation led into higher NH_3 synthesis. At –10 mA cm^{-2} on a copper cathode, ultrasound with PTFE under sonication yielded 78.9 μg h^{-1} of NH_3, compared with only 15.6 μg h^{-1} under ultrasound alone. Without ultrasound, NH_3 remained below detection, highlighting the importance of N_2 activation. Gas composition was also critical: optimized amounts of O_2 and Ar enhanced N_2 activation and boosted NH_3 yields, while purging with ambient air provided only modest performance. Control experiments confirmed that NH_3 originated from electrochemical reduction of activated N_2, not from direct conversion of N_2 to NH_3 by contact-electro-catalysis.

Overall, this work demonstrates two key points. First, Ag_3Sn, despite expectation based on prior reports, did not exhibit measurable NRR activity under the tested aqueous conditions, and rigorous control protocols are essential to avoid false positives. Second, coupling ultrasound with contact-electro-catalysis offers a viable strategy to overcome the N_2 activation bottleneck, enabling the electrochemical NH_3 production. Beyond ammonia synthesis, this controllable hybrid approach may be applicable to other challenging molecular transformations.

5.1.1 Future perspective

A review of the literature highlights how unsettled the field of direct NRR still is. While many studies report promising results, supported by mechanisms such as doping, alloying, or electrolyte engineering, serious concerns remain. Control tests like Ar purging and $^{15}N_2$ labeling are not always performed with the necessary rigor, and theoretical calculations often neglect competing reactions such as HER or the fundamental difficulty of N_2 adsorption and activation. As a result, false positives are frequent, and several catalysts once reported as active have later shown no detectable NRR activity. This has led to a situation where, despite the large number of publications, reproducibility and reliability remain open questions.

Looking ahead, progress in this field will depend less on the rapid introduction of new catalysts without rigours control tests, and more on strengthening the foundations of the research itself. Publishing negative results should be valued more, as this would prevent the repetition of ineffective approaches.

In addition, future studies may benefit from exploring directions that goes beyond conventional catalyst design. While catalyst engineering has been central in fields such as water splitting and CO_2 reduction, in NRR it may not be sufficient on its own. Hybrid strategies such as the sonoelectrochemical one explored in this thesis can be a possible solution to activate the inert N_2. Although this work demonstrated the feasibility of such an approach, both the understanding of

the underlying mechanism and the catalytic performance can be further improved in future investigations.

In terms of improving performance, several parameters can be optimized. The ultrasonic characteristics, particularly the frequency and power have a strong influence on radical generation and reaction rate. Using a probe-type ultrasonic system instead of a bath may also be beneficial, as it can produce a higher concentration of reactive radicals. Additionally, the composition of the electrolyte, and the cathode surface properties that enhance NOxRR activity are worth detailed study. Moreover, future work can be focused on adjusting the cell configuration, exploring different purging gases, and introducing surfactants to increase PTFE content in the solution. Examining other types of contact-electro-catalysis could also be promising.

From a mechanistic perspective, improving in-situ analysis techniques to detect a broader range of radicals, covering N-species, OH, H and O radicals will help clarify the specific role of cavitation in contact-electro-catalysis and its impact on radical formation. Moreover, while sonoelectrochemical HER has been investigated to some extent, it is not clear how contact-electro-catalysis might change the HER activity. It is also important to determine how certain cations or anions in the electrolyte may either hinder or promote the overall reactivity.

The following challenges should be considered when studying sonoelectrochemical reactions: The harsh reaction environment can lead to degradation of the cathode or anode if they are not sufficiently stable. Moreover, recording electrochemical responses under ultrasonic conditions remains technically challenging, since acoustic waves can cause leakage or interference at the reference electrode. Moreover, the reference electrode itself may act as an unintended site for contact-electro-catalysis.

In summary, advancing aqueous NRR will require two parallel shifts: toward reproducibility and reliable measurement on the one hand, and toward creative integration of new processes on the other.

6 BIBLIOGRAPHY

[1] Z. Deng, B. Zhu, S.J. Davis, P. Ciais, D. Guan, P. Gong, Z. Liu, Global carbon emissions and decarbonization in 2024, Nat. Rev. Earth Environ. 6 (2025) 231–233.

[2] J. Lelieveld, A. Haines, R. Burnett, C. Tonne, K. Klingmüller, T. Münzel, A. Pozzer, Air pollution deaths attributable to fossil fuels: observational and modelling study, Bmj 383 (2023).

[3] K. Vohra, A. Vodonos, J. Schwartz, E.A. Marais, M.P. Sulprizio, L.J. Mickley, Global mortality from outdoor fine particle pollution generated by fossil fuel combustion: Results from GEOS-Chem, Environ. Res. 195 (2021) 110754. https://doi.org/https://doi.org/10.1016/j.envres.2021.110754.

[4] M.P.C. Weijnen, Z. Lukszo, S. Farahani, Shaping an inclusive energy transition, Springer Nature, 2021.

[5] K.W. Kolasinski, Frontiers of surface science, Curr. Opin. Solid State Mater. Sci. 10 (2006) 129–131.

[6] D. Polverini, N. Espinosa, U. Eynard, E. Leccisi, F. Ardente, F. Mathieux, Assessing the carbon footprint of photovoltaic modules through the EU Ecodesign Directive, Solar Energy 257 (2023) 1–9.

[7] H. Falfushynska, Navigating environmental concerns: Assessing the ecological footprint of photovoltaic-produced energy, Environments 11 (2024) 140.

[8] V. Frick, E. Matthies, J. Thøgersen, T. Santarius, Do online environments promote sufficiency or overconsumption? Online advertisement and social media effects on clothing, digital devices, and air travel consumption, Journal of Consumer Behaviour 20 (2021) 288–308.

[9] J.W. Erisman, M.A. Sutton, J. Galloway, Z. Klimont, W. Winiwarter, How a century of ammonia synthesis changed the world, Nat. Geosci. 1 (2008) 636–639. https://doi.org/10.1038/ngeo325.

[10] A. Temitope, Catalytic Processes for Ammonia Synthesis in Renewable Energy Systems, (2025).

[11] V. Kyriakou, I. Garagounis, A. Vourros, E. Vasileiou, M. Stoukides, An electrochemical haber-bosch process, Joule 4 (2020) 142–158.

[12] M. Capdevila-Cortada, Electrifying the Haber–Bosch, Nat. Catal. 2 (2019) 1055. https://doi.org/10.1038/s41929-019-0414-4.

[13] C. Smith, A.K. Hill, L. Torrente-Murciano, Current and future role of Haber–Bosch ammonia in a carbon-free energy landscape, Energy Environ. Sci. 13 (2020) 331–344. https://doi.org/10.1039/C9EE02873K.

[14] D. Tonelli, L. Rosa, P. Gabrielli, A. Parente, F. Contino, Cost-competitive decentralized ammonia fertilizer production can increase food security, Nat. Food 5 (2024) 469–479.

[15] S. Mingolla, L. Rosa, Low-carbon ammonia production is essential for resilient and sustainable agriculture, Nat. Food (2025) 1–12.

[16] D.R. MacFarlane, P. V Cherepanov, J. Choi, B.H.R. Suryanto, R.Y. Hodgetts, J.M. Bakker, F.M.F. Vallana, A.N. Simonov, A roadmap to the ammonia economy, Joule 4 (2020) 1186–1205.

[17] M. Al-Zareer, I. Dincer, M.A. Rosen, Development of an integrated system for electricity and hydrogen production from coal and water utilizing a novel chemical hydrogen storage technology, Fuel Processing Technology 167 (2017) 608–621. https://doi.org/https://doi.org/10.1016/j.fuproc.2017.07.011.

[18] D. Erdemir, I. Dincer, A perspective on the use of ammonia as a clean fuel: Challenges and solutions, Int. J. Energy Res. 45 (2021) 4827–4834. https://doi.org/https://doi.org/10.1002/er.6232.

[19] L. Yovino, G. Kim, R.K. Rahman, M. Pierro, S.S. Vasu, M. Winquist, G. Subbaraman, R. Steele, Flame Speed Measurements of Ammonia–Hydrogen Mixtures for Gas-Turbines, J. Eng. Gas Turbine. Power 147 (2025) 031030.

[20] G. Wang, J. Zhao, H. Zhang, X. Wang, H. Qin, K. Wu, C. Zhao, W. Fan, J. Xu, Ammonia Co-firing with coal: A review of the status and prospects, Energy & Fuels 38 (2024) 15861–15886.

[21] G. Mohi Ud Din, Z. Yu, Y. Lou, Y. He, W. Weng, Z. Wang, Ammonia Cofiring with Coal for a Sustainable Green Power Generation: Progress and Outlook, Energy & Fuels (2025).

[22] P. Shafie, A. DeChamplain, J. Lepine, Thermal Ammonia Decomposition for Hydrogen-Rich Fuel Production and the Role of Waste Heat Recovery, Int. J. Energy Res. 2024 (2024) 9534752.

[23] H.-T. Huang, D.-C. Lu, C.-X. Li, S.-L. Zhang, Advanced design strategies for highly efficient and durable anodes in direct ammonia solid oxide fuel cells, Int. J. Hydrogen Energy 87 (2024) 89–99.

[24] C.A. Fernandez, M.C. Hatzell, Editors' Choice—Economic Considerations for Low-Temperature Electrochemical Ammonia Production: Achieving Haber-Bosch Parity, J. Electrochem. Soc. 167 (2020) 143504. https://doi.org/10.1149/1945-7111/abc35b.

[25] F. Raganati, P. Ammendola, CO2 post-combustion capture: a critical review of current technologies and future directions, Energy & Fuels 38 (2024) 13858–13905.

[26] S. Rassenfoss, Louisiana Carbon Storage Projects Surging on Fatter Tax Breaks and Blue Fuel Visions, Journal of Petroleum Technology 75 (2023) 42–48.

[27] A.S. Aricò, S. Siracusano, N. Briguglio, V. Baglio, A. Di Blasi, V. Antonucci, Polymer electrolyte membrane water electrolysis: status of technologies and potential applications in combination with renewable power sources, J. Appl. Electrochem. 43 (2013) 107–118.

[28] Y. Zhai, Y. He, J. Shao, W. Zhang, X. Tong, Z. Wang, W. Weng, Review of Hydrogen-Driven Power-to-X Technology and Application Status in China, Processes 12 (2024) 1518.

[29] K.S. Lackner, S. Brennan, China 2049: Energy Security and Climate Change, in: A New Economic Growth Engine for China: Escaping the Middle-Income Trap by Not Doing More of the Same, World Scientific, 2012: pp. 213–238.

[30] J. Hwang, K. Maharjan, H. Cho, A review of hydrogen utilization in power generation and transportation sectors: Achievements and future challenges, Int. J. Hydrogen Energy 48 (2023) 28629–28648.

[31] N. Salmon, R. Bañares-Alcántara, Impact of process flexibility and imperfect forecasting on the operation and design of Haber–Bosch green ammonia, RSC Sustainability 1 (2023) 923–937.

[32] D.R. MacFarlane, P. v Cherepanov, J. Choi, B.H.R. Suryanto, R.Y. Hodgetts, J.M. Bakker, F.M. Ferrero Vallana, A.N. Simonov, A Roadmap to the Ammonia Economy, Joule 4 (2020) 1186–1205. https://doi.org/https://doi.org/10.1016/j.joule.2020.04.004.

[33] D. Erdemir, I. Dincer, A perspective on the use of ammonia as a clean fuel: Challenges and solutions, Int. J. Energy Res. 45 (2021) 4827–4834. https://doi.org/https://doi.org/10.1002/er.6232.

[34] M. Li, H. Huang, J. Low, C. Gao, R. Long, Y. Xiong, Recent Progress on Electrocatalyst and Photocatalyst Design for Nitrogen Reduction, Small Methods 3 (2019) 1800388. https://doi.org/https://doi.org/10.1002/smtd.201800388.

[35] L. Du, L. Xing, G. Zhang, X. Liu, D. Rawach, S. Sun, Engineering of electrocatalyst/electrolyte interface for ambient ammonia synthesis, SusMat 1 (2021) 150–173.

[36] W. Tan, H. Zhao, L. Ding, N. Ren, X. Yu, A. Wang, M. Zhao, Advancements in Electrocatalytic Nitrogen Reduction Reaction: A Review on the Role of Catalyst Electronic Structure and Design Strategies, ACS Appl. Nano Mater. 8 (2025) 2632–2651.

[37] X. Chen, Y. Guo, X. Du, Y. Zeng, J. Chu, C. Gong, J. Huang, C. Fan, X. Wang, J. Xiong, Atomic structure modification for electrochemical nitrogen reduction to ammonia, Adv. Energy Mater. 10 (2020) 1903172.

[38] S. Ghoshal, A. Ghosh, P. Roy, B. Ball, A. Pramanik, P. Sarkar, Recent progress in computational design of single-atom/cluster catalysts for electrochemical and solar-driven N2 fixation, ACS Catal. 12 (2022) 15541–15575.

[39] C. Choi, G.H. Gu, J. Noh, H.S. Park, Y. Jung, Understanding potential-dependent competition between electrocatalytic dinitrogen and proton reduction reactions, Nat. Commun. 12 (2021) 4353.

[40] J.H. Montoya, C. Tsai, A. Vojvodic, J.K. Nørskov, The challenge of electrochemical ammonia synthesis: a new perspective on the role of nitrogen scaling relations, ChemSusChem 8 (2015) 2180–2186.

[41] H. Liu, N. Guijarro, J. Luo, The pitfalls in electrocatalytic nitrogen reduction for ammonia synthesis, Journal of Energy Chemistry 61 (2021) 149–154. https://doi.org/10.1016/j.jechem.2021.01.039.

[42] X. Ren, G. Cui, L. Chen, F. Xie, Q. Wei, Z. Tian, X. Sun, Electrochemical N 2 fixation to NH 3 under ambient conditions: Mo 2 N nanorod as a highly efficient and selective catalyst, Chemical Communications 54 (2018) 8474–8477.

[43] H. Huang, L. Xia, X. Shi, A.M. Asiri, X. Sun, Ag nanosheets for efficient electrocatalytic N2 fixation to NH3 under ambient conditions, Chemical Communications 54 (2018) 11427–11430. https://doi.org/10.1039/C8CC06365F.

[44] X. Ren, J. Zhao, Q. Wei, Y. Ma, H. Guo, Q. Liu, Y. Wang, G. Cui, A.M. Asiri, B. Li, High-performance N2-to-NH3 conversion electrocatalyzed by Mo2C nanorod, ACS Cent. Sci. 5 (2018) 116–121.

[45] Z.-H. Xue, S.-N. Zhang, Y.-X. Lin, H. Su, G.-Y. Zhai, J.-T. Han, Q.-Y. Yu, X.-H. Li, M. Antonietti, J.-S. Chen, Electrochemical reduction of N2 into NH3 by donor–acceptor couples of Ni and Au nanoparticles with a 67.8% Faradaic efficiency, J. Am. Chem. Soc. 141 (2019) 14976–14980.

[46] L. Tan, N. Yang, X. Huang, L. Peng, C. Tong, M. Deng, X. Tang, L. Li, Q. Liao, Z. Wei, Synthesis of ammonia via electrochemical nitrogen reduction on high-index faceted Au nanoparticles with a high faradaic efficiency, Chemical Communications 55 (2019) 14482–14485.

[47] Y.-C. Hao, Y. Guo, L.-W. Chen, M. Shu, X.-Y. Wang, T.-A. Bu, W.-Y. Gao, N. Zhang, X. Su, X. Feng, J.-W. Zhou, B. Wang, C.-W. Hu, A.-X. Yin, R. Si, Y.-W. Zhang, C.-H. Yan, Promoting nitrogen electroreduction to ammonia with bismuth nanocrystals and potassium cations in water, Nat. Catal. 2 (2019) 448–456. https://doi.org/10.1038/s41929-019-0241-7.

[48] B. Hu, M. Hu, L. Seefeldt, T.L. Liu, Electrochemical Dinitrogen Reduction to Ammonia by Mo2N: Catalysis or Decomposition?, ACS Energy Lett. 4 (2019) 1053–1054. https://doi.org/10.1021/acsenergylett.9b00648.

[49] B. Izelaar, D. Ripepi, D.D. van Noordenne, P. Jungbacker, R. Kortlever, F.M. Mulder, Identification, Quantification, and Elimination of NOx and NH3 Impurities for Aqueous and Li-Mediated Nitrogen Reduction Experiments, ACS Energy Lett. 8 (2023) 3614–3620. https://doi.org/10.1021/acsenergylett.3c01130.

[50] J. Choi, B.H.R. Suryanto, D. Wang, H.L. Du, R.Y. Hodgetts, F.M. Ferrero Vallana, D.R. MacFarlane, A.N. Simonov, Identification and elimination of false positives in electrochemical nitrogen reduction studies, Nat. Commun. 11 (2020). https://doi.org/10.1038/s41467-020-19130-z.

[51] X. Cai, F. Yang, L. An, C. Fu, L. Luo, S. Shen, J. Zhang, Evaluation of Electrocatalytic Activity of Noble Metal Catalysts Toward Nitrogen Reduction Reaction in Aqueous Solutions under Ambient Conditions, ChemSusChem 15 (2022). https://doi.org/10.1002/cssc.202102234.

[52] J. Choi, J. Choi, H.L. Du, H.L. Du, C.K. Nguyen, C.K. Nguyen, B.H.R. Suryanto, A.N. Simonov, A.N. Simonov, D.R. MacFarlane, D.R. MacFarlane, Electroreduction of Nitrates, Nitrites, and Gaseous Nitrogen Oxides: A Potential Source of Ammonia in Dinitrogen Reduction Studies, ACS Energy Lett. 5 (2020) 2095–2097. https://doi.org/10.1021/acsenergylett.0c00924.

[53] S.Z. Andersen, V. Čolić, S. Yang, J.A. Schwalbe, A.C. Nielander, J.M. McEnaney, K. Enemark-Rasmussen, J.G. Baker, A.R. Singh, B.A. Rohr, M.J. Statt, S.J. Blair, S. Mezzavilla, J. Kibsgaard, P.C.K. Vesborg, M. Cargnello, S.F. Bent, T.F. Jaramillo, I.E.L. Stephens, J.K. Nørskov, I. Chorkendorff, A rigorous electrochemical ammonia synthesis protocol with quantitative isotope measurements, Nature 570 (2019) 504–508. https://doi.org/10.1038/s41586-019-1260-x.

[54] B. Izelaar, D. Ripepi, S. Asperti, A.I. Dugulan, R.W.A. Hendrikx, A.J. Böttger, F.M. Mulder, R. Kortlever, Revisiting the Electrochemical Nitrogen Reduction on Molybdenum and Iron Carbides: Promising Catalysts or False Positives?, ACS Catal. 13 (2023) 1649–1661. https://doi.org/10.1021/acscatal.2c04491.

[55] J. Choi, H.-L. Du, M. Chatti, B.H.R. Suryanto, A.N. Simonov, D.R. MacFarlane, Reassessment of the catalytic activity of bismuth for aqueous nitrogen electroreduction, Nat. Catal. 5 (2022) 382–384. https://doi.org/10.1038/s41929-022-00785-4.

[56] W. Yu, P. Buabthong, C.G. Read, N.F. Dalleska, N.S. Lewis, H.J. Lewerenz, H.B. Gray, K. Brinkert, Cathodic NH4+leaching of nitrogen impurities in CoMo thin-film electrodes in aqueous acidic solutions, Sustain. Energy Fuels 4 (2020) 5080–5087. https://doi.org/10.1039/d0se00674b.

[57] H.L. Du, T.R. Gengenbach, R. Hodgetts, D.R. Macfarlane, A.N. Simonov, Critical Assessment of the Electrocatalytic Activity of Vanadium and Niobium Nitrides toward Dinitrogen Reduction to Ammonia, ACS Sustain. Chem. Eng. 7 (2019) 6839–6850. https://doi.org/10.1021/acssuschemeng.8b06163.

[58] H. Liu, Y. Zhang, J. Luo, The removal of inevitable NOx species in catalysts and the selection of appropriate membrane for measuring electrocatalytic ammonia synthesis accurately, Journal of Energy Chemistry 49 (2020) 51–58. https://doi.org/10.1016/j.jechem.2020.01.029.

[59] X. Yang, J. Nash, J. Anibal, M. Dunwell, S. Kattel, E. Stavitski, K. Attenkofer, J.G. Chen, Y. Yan, B. Xu, Mechanistic insights into electrochemical nitrogen reduction reaction on vanadium nitride nanoparticles, J. Am. Chem. Soc. 140 (2018) 13387–13391.

[60] D.K. Yesudoss, G. Lee, S. Shanmugam, Strong catalyst support interactions in defect-rich γ-Mo2N nanoparticles loaded 2D-h-BN hybrid for highly selective nitrogen reduction reaction, Appl. Catal. B 287 (2021) 119952.

[61] S. Kang, J. Wang, S. Zhang, C. Zhao, G. Wang, W. Cai, H. Zhang, Plasma-etching enhanced titanium oxynitride active phase with high oxygen content for ambient electrosynthesis of ammonia, Electrochem. Commun. 100 (2019) 90–95.

[62] Z. Ma, J. Chen, D. Luo, T. Thersleff, R. Dronskowski, A. Slabon, Structural evolution of CrN nanocube electrocatalysts during nitrogen reduction reaction, Nanoscale 12 (2020) 19276–19283.

[63] J. Nash, X. Yang, J. Anibal, M. Dunwell, S. Yao, K. Attenkofer, J.G. Chen, Y. Yan, B. Xu, Elucidation of the active phase and deactivation mechanisms of chromium nitride in the electrochemical nitrogen reduction reaction, The Journal of Physical Chemistry C 123 (2019) 23967–23975.

[64] Z. Qiao, D. Johnson, A. Djire, Challenges and opportunities for nitrogen reduction to ammonia on transitional metal nitrides via Mars-van Krevelen mechanism, Cell Rep. Phys. Sci. 2 (2021).

[65] X. Rao, M. Liu, M. Chien, C. Inoue, J. Zhang, Y. Liu, Recent progress in noble metal electrocatalysts for nitrogen-to-ammonia conversion, Renewable and Sustainable Energy Reviews 168 (2022) 112845.

[66] X. Long, F. Huang, Z. Yao, P. Li, T. Zhong, H. Zhao, S. Tian, D. Shu, C. He, Advancements in Electrocatalytic Nitrogen Reduction: A Comprehensive Review of Single-Atom Catalysts for Sustainable Ammonia Synthesis, Small 20 (2024) 2400551.

[67] S. Agarwal, R. Kumar, R. Arya, A.K. Singh, Rational design of single-atom catalysts for enhanced electrocatalytic nitrogen reduction reaction, The Journal of Physical Chemistry C 125 (2021) 12585–12593.

[68] H. Tao, C. Choi, L.-X. Ding, Z. Jiang, Z. Han, M. Jia, Q. Fan, Y. Gao, H. Wang, A.W. Robertson, Nitrogen fixation by Ru single-atom electrocatalytic reduction, Chem 5 (2019) 204–214.

[69] A.Y. Bhat, P. Jain, M.A. Bhat, P.P. Ingole, Mechanistic insights into the electrolyte effects on the electrochemical nitrogen reduction reaction using copper hexacyanoferrate/f-MWCNT nano-composites, Physical Chemistry Chemical Physics 26 (2024) 1777–1791.

[70] H. Xiong, Y. Meng, B. Xie, Z. Ni, S. Xia, Screening and mechanistic study of transition metal and non-metal mono-/co-doped WS2 with anti-site defects as nitrogen reduction electrocatalysts, Fuel 404 (2026) 136349.

[71] L. Lin, R. Ma, R. Jiang, S. Lin, Design of high performance nitrogen reduction electrocatalysts by doping defective polyoxometalate with a single atom promoter, Physical Chemistry Chemical Physics 26 (2024) 8494–8503.

[72] M. Nazemi, P. Ou, A. Alabbady, L. Soule, A. Liu, J. Song, T.A. Sulchek, M. Liu, M.A. El-Sayed, Electrosynthesis of ammonia using porous bimetallic Pd–Ag nanocatalysts in liquid- and gas-phase systems, ACS Catal. 10 (2020) 10197–10206.

[73] S. Zhang, M. Han, T. Shi, H. Zhang, Y. Lin, X. Zheng, L.R. Zheng, H. Zhou, C. Chen, Y. Zhang, Atomically dispersed bimetallic Fe–Co electrocatalysts for green production of ammonia, Nat. Sustain. 6 (2023) 169–179.

[74] H. Wang, Q. Mao, H. Yu, S. Wang, Y. Xu, X. Li, Z. Wang, L. Wang, Enhanced electrocatalytic performance of mesoporous Au-Rh bimetallic films for ammonia synthesis, Chemical Engineering Journal 418 (2021) 129493.

[75] Y. Gao, M.-J. Zhu, X.-H. Liu, G.-L. Dai, Y.-W. Zhou, Z.-D. Meng, L. Luo, T. Gan, F. Chen, Y.-Y. Zhou, Electrocatalytic nitrogen reduction to ammonia at low overpotentials based on

tungsten carbide doped by non-precious metal single cobalt atoms, Chemical Engineering Journal 493 (2024) 152659.

[76] K.P. Ramaiyan, S. Ozden, S. Maurya, D. Kelly, S.K. Babu, A. Benavidez, F.G. Garzon, Y.S. Kim, C.R. Kreller, R. Mukundan, Molybdenum carbide electrocatalysts for electrochemical synthesis of ammonia from nitrogen: activity and stability, J. Electrochem. Soc. 167 (2020) 044506.

[77] S.Y. Park, Y.J. Jang, D.H. Youn, A review of transition metal nitride-based catalysts for electrochemical nitrogen reduction to ammonia, Catalysts 13 (2023) 639.

[78] S. Chen, X. Liu, J. Xiong, L. Mi, X.-Z. Song, Y. Li, Defect and interface engineering in metal sulfide catalysts for the electrocatalytic nitrogen reduction reaction: a review, J. Mater. Chem. A Mater. 10 (2022) 6927–6949.

[79] S. Zhang, M. Han, T. Shi, H. Zhang, Y. Lin, X. Zheng, L.R. Zheng, H. Zhou, C. Chen, Y. Zhang, Atomically dispersed bimetallic Fe–Co electrocatalysts for green production of ammonia, Nat. Sustain. 6 (2023) 169–179.

[80] L. Shi, Y. Yin, S. Wang, H. Sun, Rational catalyst design for N2 reduction under ambient conditions: strategies toward enhanced conversion efficiency, ACS Catal. 10 (2020) 6870–6899.

[81] L. Li, C. Tang, H. Jin, K. Davey, S.-Z. Qiao, Main-group elements boost electrochemical nitrogen fixation, Chem 7 (2021) 3232–3255.

[82] G. Wu, W. Zhang, R. Yu, Y. Yang, J. Jiang, M. Sun, A. Du, W. He, L. Dai, X. Mao, p–d Orbital Hybridization in Ag-based Electrocatalysts for Enhanced Nitrate-to-Ammonia Conversion, Angewandte Chemie 136 (2024) e202410251.

[83] B. Chen, C. Zheng, D. Shi, Y. Huang, R. Deng, Y. Wei, Z. Liu, Y. Yu, S. Zhong, pd orbital hybridization induced by CuGa2 promotes selective N2 electroreduction, Chinese Journal of Structural Chemistry 44 (2025) 100468. https://doi.org/http://dx.doi.org/10.1021/acs.inorgchem.8b02436.

[84] L. Ji, X. Shi, A.M. Asiri, B. Zheng, X. Sun, Nanostructured Bromide-Derived Ag Film: An Efficient Electrocatalyst for N2 Reduction to NH3 under Ambient Conditions, Inorg. Chem. 57 (2018) 14692–14697. https://doi.org/10.1021/acs.inorgchem.8b02436.

[85] Z. Xue, C. Sun, M. Zhao, Y. Cui, Y. Qu, H. Ma, Z. Wang, Q. Jiang, Efficient Electrocatalytic Nitrogen Reduction to Ammonia on Ultrafine Sn Nanoparticles, ACS Appl. Mater. Interfaces 13 (2021) 59834–59842. https://doi.org/10.1021/acsami.1c15324.

[86] X. Lv, F. Wang, J. Du, Q. Liu, Y. Luo, S. Lu, G. Chen, S. Gao, B. Zheng, X. Sun, Sn dendrites for electrocatalytic N2 reduction to NH3 under ambient conditions, Sustain. Energy Fuels 4 (2020) 4469–4472. https://doi.org/10.1039/D0SE00828A.

[87] K.S. Suslick, S.J. Doktycz, E.B. Flint, On the origin of sonoluminescence and sonochemistry, Ultrasonics 28 (1990) 280–290.

[88] L.A. Yusuf, P.J. McHugh, G. Cioncoloni, J. Song, C.A. Morrison, E. Palmer, F.F. Franco, F.A. Boroujeni, C. Gauchotte-Lindsay, P. Prentice, Toward decentralized nitrogen fixation using pulsed ultrasound, Cell Rep. Phys. Sci. (2025).

[89] T. Hou, T. Shan, H. Rong, J. Zhang, Nitrate Electroreduction to Ammonia Over Copper-based Catalysts, ChemSusChem 18 (2025) e202402331.

[90] W.-S. Hu, Oxygen transfer in cell culture bioreactors, in: Cell Culture Bioprocess Engineering, Second Edition, CRC Press, 2020: pp. 351–373.

[91] J. Zhou, M. Wen, R. Huang, Q. Wu, Y. Luo, Y. Tian, G. Wei, Y. Fu, Regulating active hydrogen adsorbed on grain boundary defects of nano-nickel for boosting ammonia electrosynthesis from nitrate, Energy Environ. Sci. 16 (2023) 2611–2620.

[92] J. Li, G. Zhan, J. Yang, F. Quan, C. Mao, Y. Liu, B. Wang, F. Lei, L. Li, A.W.M. Chan, Efficient ammonia electrosynthesis from nitrate on strained ruthenium nanoclusters, J. Am. Chem. Soc. 142 (2020) 7036–7046.

[93] L. Tao, Y. Zhao, H. Sun, Metallenes for electrocatalytic nitrate reduction, Mater. Today Chem. 42 (2024) 102418.

[94] H. Li, D.H. Robertson, J.Q. Chambers, D.T. Hobbs, Electrochemical reduction of nitrate and nitrite in concentrated sodium hydroxide at platinum and nickel electrodes, J. Electrochem. Soc. 135 (1988) 1154.

[95] J.-Y. Zhu, Q. Xue, Y.-Y. Xue, Y. Ding, F.-M. Li, P. Jin, P. Chen, Y. Chen, Iridium nanotubes as bifunctional electrocatalysts for oxygen evolution and nitrate reduction reactions, ACS Appl. Mater. Interfaces 12 (2020) 14064–14070.

[96] J. Lim, C.-Y. Liu, J. Park, Y.-H. Liu, T.P. Senftle, S.W. Lee, M.C. Hatzell, Structure sensitivity of Pd facets for enhanced electrochemical nitrate reduction to ammonia, ACS Catal. 11 (2021) 7568–7577.

[97] Y.-J. Shih, Z.-L. Wu, Y.-H. Huang, C.-P. Huang, Electrochemical nitrate reduction as affected by the crystal morphology and facet of copper nanoparticles supported on nickel foam electrodes (Cu/Ni), Chemical Engineering Journal 383 (2020) 123157.

[98] X. Deng, Y. Yang, L. Wang, X. Fu, J. Luo, Metallic Co nanoarray catalyzes selective NH3 production from electrochemical nitrate reduction at current densities exceeding 2 A cm−2, Advanced Science 8 (2021) 2004523.

[99] W. Fu, X. Du, P. Su, Q. Zhang, M. Zhou, Synergistic effect of Co (III) and Co (II) in a 3D structured Co3O4/carbon felt electrode for enhanced electrochemical nitrate reduction reaction, ACS Appl. Mater. Interfaces 13 (2021) 28348–28358.

[100] Y. Guo, R. Zhang, S. Zhang, Y. Zhao, Q. Yang, Z. Huang, B. Dong, C. Zhi, Pd doping-weakened intermediate adsorption to promote electrocatalytic nitrate reduction on TiO 2 nanoarrays for ammonia production and energy supply with zinc–nitrate batteries, Energy Environ. Sci. 14 (2021) 3938–3944.

[101] J. Wei, Y. Li, H. Lin, X. Lu, C. Zhou, Y. Li, Copper-based electro-catalytic nitrate reduction to ammonia from water: Mechanism, preparation, and research directions, Environmental Science and Ecotechnology 20 (2024) 100383.

[102] Y. Zhao, Y. Liu, Z. Zhang, Z. Mo, C. Wang, S. Gao, Flower-like open-structured polycrystalline copper with synergistic multi-crystal plane for efficient electrocatalytic reduction of nitrate to ammonia, Nano Energy 97 (2022) 107124.

[103] Z. Shen, Y. Yu, Z. Zhao, S. Zhang, S. Xu, S. Yang, Y. Hu, Highly distributed amorphous copper catalyst for efficient ammonia electrosynthesis from nitrate, J. Hazard. Mater. 445 (2023) 130651.

[104] M. Karamad, T.J. Goncalves, S. Jimenez-Villegas, I.D. Gates, S. Siahrostami, Why copper catalyzes electrochemical reduction of nitrate to ammonia, Faraday Discuss. 243 (2023) 502–519.

[105] P. Kruus, Sonochemical formation of nitrate and nitrite in water, Ultrason. Sonochem. 7 (2000) 109–113.

[106] H. Schultes, H. Gohr, Über chemische wirkungen der ultraschallwellen, Angewandte Chemie 49 (1936) 420–423.

[107] J. Yao, L. Chen, X. Chen, L. Zhou, W. Liu, Z. Zhang, Formation of inorganic nitrogenous byproducts in aqueous solution under ultrasound irradiation, Ultrason. Sonochem. 42 (2018) 42–47.

[108] K. Okitsu, R. Kunichika, S. Asada, Quantitation and evaluation of NO2−, NO3−, and H2O2 in the sonolysis of aqueous NaOH solution under air and air-Ar mixture: Effects of solution temperature, ultrasonic power, and ratio of gas mixture, Ultrason. Sonochem. 100 (2023) 106612.

[109] C.A. Wakeford, R. Blackburn, P.D. Lickiss, Effect of ionic strength on the acoustic generation of nitrite, nitrate and hydrogen peroxide, Ultrason. Sonochem. 6 (1999) 141–148.

[110] P. Kruus, Sonochemical formation of nitrate and nitrite in water, Ultrason. Sonochem. 7 (2000) 109–113.

[111] Y. Son, J. Choi, Effects of gas saturation and sparging on sonochemical oxidation activity in open and closed systems, part II: NO2−/NO3− generation and a brief critical review, Ultrason. Sonochem. 92 (2023) 106250.

[112] Z. Wang, A. Berbille, Y. Feng, S. Li, L. Zhu, W. Tang, Z.L. Wang, Contact-electro-catalysis for the degradation of organic pollutants using pristine dielectric powders, Nat. Commun. 13 (2022) 130.

[113] J. Zhao, X. Zhang, J. Xu, W. Tang, Z. Lin Wang, F. Ru Fan, Contact-electro-catalysis for Direct Synthesis of H2O2 under Ambient Conditions, Angewandte Chemie International Edition 62 (2023) e202300604.

[114] X. Dong, Z. Wang, Y. Hou, T. Wang, F.-J. Lv, W. Tang, Quantified analysis on the conversion from contact electrification to contact-electro-catalysis and the performance of contact-electro-catalysts, J. Catal. (2025) 116153.

[115] Z. Wang, A. Berbille, Y. Feng, S. Li, L. Zhu, W. Tang, Z.L. Wang, Contact-electro-catalysis for the degradation of organic pollutants using pristine dielectric powders, Nat. Commun. 13 (2022) 130.

[116] H. Li, A. Berbille, X. Zhao, Z. Wang, W. Tang, Z.L. Wang, A contact-electro-catalytic cathode recycling method for spent lithium-ion batteries, Nat. Energy 8 (2023) 1137–1144.

[117] W. Li, J. Sun, M. Wang, J. Xu, Y. Wang, L. Yang, R. Yan, H. He, S. Wang, W. Deng, Contact-electro-catalysis for direct oxidation of methane under ambient conditions, Angewandte Chemie 136 (2024) e202403114.

[118] J. Li, Y. Xia, X. Song, B. Chen, R.N. Zare, Continuous ammonia synthesis from water and nitrogen via contact electrification, Proceedings of the National Academy of Sciences 121 (2024) e2318408121.

[119] S. Huang, Y. Liu, L. Ren, L. Huang, J. Tang, Z. Yu, M. Chen, S. Zhou, Direct Conversion of N2 to Nitric Acid via Contact Electrocatalysis, ACS Sustain. Chem. Eng. (2025).

[120] S. Kweon, N. Qureshi, J.H. Shim, Engineering MoFe Nanostructures on Carbon Cloth for Sustainable Ammonia Production via Nitrogen Reduction, ChemCatChem 17 (2025) e202401936.

[121] W. Wang, W. Liu, Y. Zeng, Y. Han, M. Yu, X. Lu, Y. Tong, A Novel Exfoliation Strategy to Significantly Boost the Energy Storage Capability of Commercial Carbon Cloth., Adv. Mater. 27 (2015) 3572–3578.

[122] Z. Yan, H. Liu, Z. Hao, M. Yu, X. Chen, J. Chen, Electrodeposition of (hydro) oxides for an oxygen evolution electrode, Chem. Sci. 11 (2020) 10614–10625.

[123] Q. Wang, F. Chen, Y. Liu, T.T. Gebremariam, J. Wang, L. An, R.L. Johnston, AgSn intermetallics as highly selective and active oxygen reduction electrocatalysts in membraneless alkaline fuel cells, J. Power Sources 404 (2018) 106–117. https://doi.org/https://doi.org/10.1016/j.jpowsour.2018.10.013.

[124] S. Esmailzadeh, T. Shahrabi, Y. Yaghoubinezhad, G.B. Darband, An analytical study on nucleation and growth mechanism of nanostructured Ni-Se coating by the chronoamperometry and pulse potential techniques, Journal of Electroanalytical Chemistry 881 (2021) 114949.

[125] M. Wang, S. Liu, T. Qian, J. Liu, J. Zhou, H. Ji, J. Xiong, J. Zhong, C. Yan, Over 56.55% Faradaic efficiency of ambient ammonia synthesis enabled by positively shifting the reaction potential, Nat. Commun. 10 (2019) 341.

[126] W.-Y. Gao, Y.-C. Hao, X. Su, L.-W. Chen, T.-A. Bu, N. Zhang, Z.-L. Yu, Z. Zhu, A.-X. Yin, Morphology-dependent electrocatalytic nitrogen reduction on Ag triangular nanoplates, Chemical Communications 55 (2019) 10705–10708.

[127] J.W. Erisman, M.A. Sutton, J. Galloway, Z. Klimont, W. Winiwarter, How a century of ammonia synthesis changed the world, Nat. Geosci. 1 (2008) 636–639. https://doi.org/10.1038/ngeo325.

[128] M. Capdevila-Cortada, Electrifying the Haber–Bosch, Nat. Catal. 2 (2019) 1055. https://doi.org/10.1038/s41929-019-0414-4.

[129] C. Smith, A.K. Hill, L. Torrente-Murciano, Current and future role of Haber–Bosch ammonia in a carbon-free energy landscape, Energy Environ. Sci. 13 (2020) 331–344. https://doi.org/10.1039/C9EE02873K.

[130] X. Cui, C. Tang, Q. Zhang, A Review of Electrocatalytic Reduction of Dinitrogen to Ammonia under Ambient Conditions, Adv. Energy Mater. 8 (2018). https://doi.org/10.1002/aenm.201800369.

[131] L. An, Z. Zhang, G. Liu, W. Liu, Y. Fu, D. Qu, Y. Liu, P. Hu, Z. Sun, Recent advances in transition metal electrocatalysts for effective nitrogen reduction reaction under ambient conditions, EcoEnergy 2 (2024) 229–257.

[132] M. Yan, R. Wei, R. Zhang, X. Zhang, S. Sun, X. Wei, X. Wang, S. Yin, Y. Wang, Distinctive p-d Orbital Hybridization in CuSb Porous Nanonetworks for Enhanced Nitrite Electroreduction to Ammonia, Small 20 (2024) 2310409.

[133] J. Zhang, J. Sun, T.A. Shifa, D. Wang, X. Wu, Y. Cui, Hierarchical MnO2/activated carbon cloth electrode prepared by synchronized electrochemical activation and oxidation for flexible asymmetric supercapacitors, Chemical Engineering Journal 372 (2019) 1047–1055.

[134] A. Goyal, M.T.M. Koper, The interrelated effect of cations and electrolyte pH on the hydrogen evolution reaction on gold electrodes in alkaline media, Angewandte Chemie International Edition 60 (2021) 13452–13462.

[135] G.K. Gebremariam, A.Z. Jovanović, I.A. Pašti, The effect of electrolytes on the kinetics of the hydrogen evolution reaction, Hydrogen 4 (2023) 776–806.

[136] Y. Ma, T. Yang, H. Zou, W. Zang, Z. Kou, L. Mao, Y. Feng, L. Shen, S.J. Pennycook, L. Duan, Synergizing Mo single atoms and Mo2C nanoparticles on CNTs synchronizes selectivity and activity of electrocatalytic N2 reduction to ammonia, Advanced Materials 32 (2020) 2002177.

[137] W. Peng, M. Luo, X. Xu, K. Jiang, M. Peng, D. Chen, T. Chan, Y. Tan, Spontaneous atomic ruthenium doping in Mo2CTX MXene defects enhances electrocatalytic activity for the nitrogen reduction reaction, Adv. Energy Mater. 10 (2020) 2001364.

[138] Y. Sun, Y. Wang, H. Li, W. Zhang, X.-M. Song, D.-M. Feng, X. Sun, B. Jia, H. Mao, T. Ma, Main group metal elements for ambient-condition electrochemical nitrogen reduction, Journal of Energy Chemistry 62 (2021) 51–70. https://doi.org/https://doi.org/10.1016/j.jechem.2021.03.001.

[139] M. Wang, S. Liu, T. Qian, J. Liu, J. Zhou, H. Ji, J. Xiong, J. Zhong, C. Yan, Over 56.55% Faradaic efficiency of ambient ammonia synthesis enabled by positively shifting the reaction potential, Nat. Commun. 10 (2019). https://doi.org/10.1038/s41467-018-08120-x.

[140] J. Enkovaara, N.A. Romero, S. Shende, J.J. Mortensen, GPAW-massively parallel electronic structure calculations with Python-based software, Procedia Comput. Sci. 4 (2011) 17–25.

[141] J. Wellendorff, K.T. Lundgaard, A. Møgelhøj, V. Petzold, D.D. Landis, J.K. Nørskov, T. Bligaard, K.W. Jacobsen, Density functionals for surface science: Exchange-correlation model development with Bayesian error estimation, Physical Review B—Condensed Matter and Materials Physics 85 (2012) 235149.

[142] P.E. Blöchl, Projector augmented-wave method, Phys. Rev. B 50 (1994) 17953.

[143] C.W. Fairhurst, J.B. Cohen, The crystal structures of two compounds found in dental amalgam: Ag2Hg3 and Ag3Sn, Acta Crystallogr. B 28 (1972) 371–378.

[144] A.H. Larsen, J.J. Mortensen, J. Blomqvist, I.E. Castelli, R. Christensen, M. Dułak, J. Friis, M.N. Groves, B. Hammer, C. Hargus, The atomic simulation environment—a Python library for working with atoms, Journal of Physics: Condensed Matter 29 (2017) 273002.

[145] S. Dahl, A. Logadottir, R.C. Egeberg, J.H. Larsen, I. Chorkendorff, E. Törnqvist, J.K. Nørskov, Role of steps in N 2 activation on Ru (0001), Phys. Rev. Lett. 83 (1999) 1814.

[146] A.L. Garden, E. Skulason, The mechanism of industrial ammonia synthesis revisited: calculations of the role of the associative mechanism, The Journal of Physical Chemistry C 119 (2015) 26554–26559.

[147] E. Skulason, T. Bligaard, S. Gudmundsdóttir, F. Studt, J. Rossmeisl, F. Abild-Pedersen, T. Vegge, H. Jónsson, J.K. Nørskov, A theoretical evaluation of possible transition metal electro-catalysts for N 2 reduction, Physical Chemistry Chemical Physics 14 (2012) 1235–1245.

[148] J.H. Montoya, C. Tsai, A. Vojvodic, J.K. Nørskov, The challenge of electrochemical ammonia synthesis: a new perspective on the role of nitrogen scaling relations, ChemSusChem 8 (2015) 2180–2186.

[149] H.M. Irfan, K. Iqbal, M.I. Taipabu, C.-Y. You, D. Mazumdar, W. Wu, Decarbonization frameworks to industrial-scale ammonia production: Techno-economic and environmental implications, Int. J. Hydrogen Energy 78 (2024) 580–593. https://doi.org/10.1016/j.ijhydene.2024.06.312 (accessed September 4, 2025).

[150] A. Mangini, J.B.V. Mygind, S.G. Ballesteros, A. Pedico, M. Armandi, I. Chorkendorff, F. Bella, Multivariate Approaches Boosting Lithium-Mediated Ammonia Electrosynthesis in Different Electrolytes, Angewandte Chemie International Edition 64 (2025) e202416027. https://doi.org/https://doi.org/10.1002/anie.202416027.

[151] K.H.R. Rouwenhorst, F. Jardali, A. Bogaerts, L. Lefferts, From the Birkeland–Eyde process towards energy-efficient plasma-based NO X synthesis: a techno-economic analysis, Energy Environ. Sci. 14 (2021) 2520–2534.

[152] L.-M. Kwedi-Nsah, T. Kobayashi, Sonochemical nitrogen fixation for the generation of NO2− and NO3− ions under high-powered ultrasound in aqueous medium, Ultrason. Sonochem. 66 (2020) 105051.

[153] M.-N. Liu, J.-H. Liu, L.-Y. Wang, F. Yin, G. Zheng, R. Li, J. Zhang, Y.-Z. Long, Strategies for Improving Contact-Electro-Catalytic Efficiency: A Review, Nanomaterials 15 (2025) 386.

[154] X. Dong, Z. Wang, Y. Hou, T. Wang, F.-J. Lv, W. Tang, Quantified analysis on the conversion from contact electrification to contact-electro-catalysis and the performance of contact-electro-catalysts, J. Catal. 448 (2025) 116153. https://doi.org/https://doi.org/10.1016/j.jcat.2025.116153.

[155] J. Zhao, X. Zhang, J. Xu, W. Tang, Z. Lin Wang, F. Ru Fan, Contact-electro-catalysis for Direct Synthesis of H2O2 under Ambient Conditions, Angewandte Chemie International Edition 62 (2023) e202300604.

[156] Z. Wang, J. Liu, H. Zhao, W. Xu, J. Liu, Z. Liu, J. Lai, L. Wang, Free radicals promote electrocatalytic nitrogen oxidation, Chem. Sci. 14 (2023) 1878–1884.

[157] M. Teng, J. Ye, C. Wan, G. He, H. Chen, Research progress on Cu-based catalysts for electrochemical nitrate reduction reaction to ammonia, Ind. Eng. Chem. Res. 61 (2022) 14731–14746.

[158] E. Skulason, T. Bligaard, S. Gudmundsdóttir, F. Studt, J. Rossmeisl, F. Abild-Pedersen, T. Vegge, H. Jónsson, J.K. Nørskov, A theoretical evaluation of possible transition metal electro-catalysts for N 2 reduction, Physical Chemistry Chemical Physics 14 (2012) 1235–1245.

[159] A. Wu, J. Yang, B. Xu, X.-Y. Wu, Y. Wang, X. Lv, Y. Ma, A. Xu, J. Zheng, Q. Tan, Direct ammonia synthesis from the air via gliding arc plasma integrated with single atom electrocatalysis, Appl. Catal. B 299 (2021) 120667.

[160] E. Murray, E.P. Nesterenko, M. McCaul, A. Morrin, D. Diamond, B. Moore, A colorimetric method for use within portable test kits for nitrate determination in various water matrices, Analytical Methods 9 (2017) 680–687. https://doi.org/10.1039/C6AY03190K.